REFLECTOR FEEDS FOR

LARGE ADAPTIVE REFLECTOR ANTENNAS

By:

Seyed Pedram Mousavi Bafrooei

A Thesis

Submitted to the Faculty of Graduate Studies

in Partial Fulfillment of the Requirements

for the Degree of

Doctor of Philosophy

Department of Electrical and Computer Engineering

The University of Manitoba

Winnipeg, Manitoba, Canada.

THE UNIVERSITY OF MANITOBA

FACULTY OF GRADUATE STUDIES

*****

COPYRIGHT PERMISSION PAGE

Reflector Feeds for Large Adaptive Reflector Antennas

BY

Seyed Pedram Mousavi Bafrooei

A Thesis/Practicum submitted to the Faculty of Graduate Studies of The University of Manitoba in partial fulfillment of the requirements of the degree of Doctor of Philosophy

To my parents:

for their lifetime efforts to teach

me the value of knowledge and wisdom

ABSTRACT

A novel Feed-Reflector system for large Cassegrain antennas for Radio Astronomy and Deep-Space Communication applications is investigated. This Feed-Reflector is used to illuminate a hyperboloid sub-reflector with 5-10 m diameter located 500 m above the ground. Because the sub-reflector is located in the near field of the Feed-Reflector antenna, a theory based on the near field focusing properties of paraboloid reflectors is established. The focusing at near distance is formed by moving the feed horn away from the focal point of the Feed-Reflector. In this theory the properties of axial defocused paraboloid reflectors at near distance are investigated in some detail.

By using equivalence path law, sub-reflector shape is obtained. It is found that the hyperbola can approximate the sub-reflector well. A detailed ray tracing analysis is performed on the entire system which reveals that some part of the sub-reflector receive three rays per point from the feed. The performance of the system over the operating band (1-22 GHz) is also studied and shown that the lower frequency limit is dependent on sub-reflector and Feed-Reflector sizes.

To obtain higher efficiencies, three sets of shaping techniques, based on the genetic algorithm and Jacobi Fourier surface expansion, are performed. An efficiency of 78.5% for a 5 m sub-reflector is obtained.

In another method of analysis, the Feed-Reflector aperture field distribution is expanded into a set of Gaussian-Laguerre modes. These modes propagate from the Feed-Reflector aperture in a simple and well defined way. The Feed-Reflector near field radia-

tion pattern is calculated at the sub-reflector location. The sub-reflector parameters in this system are found by maximizing the Large Adaptive Reflector (LAR) aperture efficiency which includes phase and taper efficiencies, and minimizing the LAR spillover loss.

An exact equation for the offset LAR surface is obtained in this thesis. To scan the beam up to 60^{o}, which is one of the LAR requirements, the concept of the dual offset LAR with the Feed-Reflector is introduced. In this design the cross-polarization is eliminated by proper orientation of the sub-reflector. The parameters of the configuration are obtained by utilizing generalized Gauss-Laguerre beam modes and matrix representation of beam mode transformation factor. In this design the blockage effect due to the Feed-Reflector is totally removed.

ACKNOWLEDGMENTS

I would like to express my sincere gratitude to my advisor Professor Lotfollah Shafai for his knowledge, insight, enthusiasm, and continuous encouragement and support through out this research. He is always there when I need help.

I would like also to thank Dr. G. Bridges, Dr. C. Shafai, Dr. McGreer, N. Sepehri, and Dr. A. Kishk for serving on my committee and for their constructive criticisms and suggestions in the preparation of the final report.

Thanks are owed to Dr. P. Dewdney and Dr. B. Veidt of National Research Council of Canada, for initiating this research and providing me with the required software and first year financial support. I also benefited from many discussions with them.

I am also thankful to Dr. V. Jamnejad of Jet Propulsion Laboratories of California Institute of Technology, for his useful comments.

I would also like to take this opportunity to thank the Faculty of Graduate Studies for a Graduate Student Fellowship, and Department of Electrical and Computer Engineering for providing me with their facilities.

Financial support during this study was provided by grants from the Natural Science and Engineering Research Council of Canada (NSERC), and Canadian Institute of Telecommunication Research (CITR). Their contribution is greatly appreciated.

Last, but not least, endless thanks to my wife, Mojgan, for her kindness, generous love, support and understanding of my neglects during the period of this thesis.

TABLE OF CONTENTS

LIST OF FIGURES

LIST OF TABLES

Chapter 1

INTRODUCTION

1.1. Motivation and Objective of the Thesis

The concept of Large Adaptive Reflector antenna (LAR) has been previously proposed as a candidate for the next generation Radio Telescopes [1]. It consists of a large and almost flat paraboloid reflector of diameter in excess of 200 m, having an adjustable shape made of identical flat panels supported by actuators on the ground, as shown in Figs. 1.1 and 1.2. Its nearly flat profile allows wide angle beam scanning of around $\pm 60^{\circ}$. Its manageable actuator plays and maintains acceptable beam characteristics. It, however, requires large focal lengths, in excess of unity. This imposes an unusual condition that the feed or sub-reflector be carried by an airborne vehicle, a tethered aerostat. During the beam scan, to compromise between large panel actuator displacements and excessive aerostat motions, the airborne device moves along a constant radius trajectory, where the distance between the centre of the reflector and aerostat is kept constant. For further minimization of the actuator plays, an optimum reflector surface may be found, which in general will be an offset configuration.

Variations of the concept, especially using smaller reflectors may also be used for other applications, such as deep space communication. A possible set of parameters for this application are shown in Table 1.1. The sub-reflector diameter $D_S = 5 \sim 10$ m is selected due to the aerostat size limitation. With a prime focus configuration this dimen-

sion, D_S, may also be used for the feed carriage motion to accommodate small beam scanning without the aerostat motion. The main reflector diameter of 200 m can provide a peak gain in excess of 85 dBi at the Ku-band, with a reasonable aperture efficiency of 70 percent, making it a good candidate for this intended application.

Because of the large reflector focal length, the optical system configuration is an important issue. The prime focus configuration provides the best optical preference [2], but requires the receiver to be located at the aerostat. This requires, a powered aerostat, which complicates its design and increases the cost. Conventional Cassegrain and Gregorian designs are also not suitable, since they further increase the focal length. An inverted sub-reflector to reduce the system focal length is more desirable, but also suffers from the same problems of the prime focus case. With sub-reflector sizes of 5~10 m and a small spillover power, a conventional feed horn must be in its close proximity to allow efficient illumination. This again means that the receiver must be near the aerostat. Naturally, the best place for the receiver is on the ground. This requires the feed to be on the ground, at a distance of 500 m from a small sub-reflector of diameter 5~10 m. The feed aperture therefore must be very large to illuminate the sub-reflector efficiently with small spillover power, which renders a conventional feed horn useless. A better choice is a larger aperture antenna with adequate aperture phase aberration to focus its beam on the small sub-reflector [3]-[6]. Such a larger aperture can be generated conveniently, using a defocused paraboloid [7]-[10]. Thus, a cost effective feed design for a LAR that is located on the ground, is another paraboloid, i.e. a "Feed-Reflector". The advantage of a paraboloid over an ellipsoid reflector [11] is its flexible focii distances. The design of such a Feed-Reflector and performance of a dual-reflector LAR, using this feed, is the object of this investigation.

For radio astronomy applications the frequency band of interest is 1-22 GHz, which also covers active communication bands. In this frequency range the sub-reflector is in the near field of the Feed-Reflector, and must intercept most of its radiated power. The near field focusing properties of aperture antennas in general and reflector antennas in particular are investigated in [3]-[10], [12]. Beamwidth and sidelobes of the field distribution in the image region of a focusing device is nearly independent of the image point location, provided it is not too close to the antenna to cause serious aberrations[5]. For large antennas a convenient distance limit is the size of its aperture, where the first order term for the observation distance is dominant. That is, the beamwidth and sidelobes of the focused beams remain nearly constant as the image point moves from infinity towards the aperture, until it reaches a distance of about the size of the antenna aperture.

1.2. Structure of the Thesis

The structure, parameters and the importance of the Large Adaptive Reflector antenna (LAR) were stressed in this chapter. As mentioned in the previous section a Feed-Reflector for Cassegrainian LAR is one of the candidates to feed this system. This suggests development of various analytical tools and physical model to design the Feed-Reflector and analyse the whole configuration. The existing theoretical frameworks in the design and analysis of the Feed-Reflector and the LAR Cassegrainian system will be discussed in chapter 2. This chapter is not meant to be an exhaustive review on reflector antenna and radio telescope feed systems. The area is too wide to be covered in a single chapter. Nevertheless it is hoped to provide sufficient background on the most important

issues used in this thesis. The radio telescope feed systems, numerical techniques, synthesis techniques for reflector antennas and aperture near field and defocused paraboloid reflector are addressed in chapter 2. Also, mentioned are the Gaussian beam techniques and offset reflector antennas.

Chapter 3 deals with theories to design the Feed-Reflector system for the LAR. This theory is established based on the near field focusing properties of aperture antennas. Because the sub-reflector is located in the Fresnel region of the Feed-Reflector antenna, the fields at this region for paraboloid reflector antenna are calculated. The quadratic phase at the Fresnel region is cancelled by defocusing the feed horn away from the Feed-Reflector focal point which brings the far field radiation patterns to the near field. The formula for the Feed-Reflector diameter to illuminate the sub-reflector properly is derived. The sub-reflector profile is obtained to maximize the LAR efficiency by utilizing Geometrical Optics (GO).

Chapter 4 includes the investigation of the performance of the symmetric Cassegrainian LAR with the Feed-Reflector. The formulation for the hyperboloid sub-reflector in this symmetric configuration is derived. Detailed ray tracing is performed on the entire system which reveals that the feed system uses some part of sub-reflector three times. The gain, side lobe level, cross-polarization, and aperture distribution are calculated for different feed horn locations and taper at the edge of Feed-Reflector, and also for different sizes and eccentricity of the sub-reflector. The performance of the system over the operating band (1-22 GHz) is also studied in this chapter. To obtain higher efficiencies, three sets of shapings, based on genetic algorithm and Jacobi Fourier surface expansion, are per-

formed. Physical Optics (PO) using Jacobi-Bessel series [13]-[15] and body of revolution formulation [16], [17] are applied on the Feed-Reflector, sub-reflector and LAR. TICRA reflector antenna software, GRASP8W [19], has been used to confirm this study. For the sub-reflector, Physical Theory of Diffraction (PTD) [18] implemented in GRASP8W, is used in addition to Physical Optics.

A novel approach for analysing the quasi-optical LAR Cassegrain system is described in chapter 5. In the proposed method of analysis, the Feed-Reflector aperture field distribution is expanded into a set of Gaussian-Laguerre modes. These modes propagate from the Feed-Reflector aperture in a simple and well defined way. The Feed-Reflector near field radiation pattern is calculated at the sub-reflector location. The sub-reflector parameters in this system is found by maximizing the LAR aperture efficiency, which includes phase and taper efficiencies, and minimizing the LAR spillover loss. This process is computationally more efficient than the physical optics current distribution method, and more accurate than the ray tracing approach. It also provides a new insight into the operation of the Feed-Reflector system.

Chapter 6 introduces the concept of the offset Cassegrainian LAR. In this chapter the formulation for the LAR surface to scan different scan angles is derived. Two Cassegrainian configurations are presented. The first one is an open Cassegrainian configuration, where the Feed-Reflector sits in the middle of the LAR. The second one is a dual offset Cassegrainian system. In the latter design, the introduction of generalized Gaussian beam modes, which includes modes representing the cross-polarization, facilitates the derivation of the system parameters. Also in this chapter, the performance of a dual offset LAR over

its frequency band are investigated.

Table 1.1: Typical parameter for LAR Cassegrain system

Parameter	Symbol	Dimension /Unit
LAR Diameter	D_L	200 m
LAR Focal Length	f_L	500 m
LAR Cylindrical Coordinates	ρ_L, ϕ_L, z_L	(m) & (Degree)
Feed-Reflector Diameter	D_F	Design Parameter (m)
Feed-Reflector Focal Length	f_F	Design Parameter (m)
Feed-Reflector Defocus Distance	d_f	Design Parameter (cm)
Field Taper at the Feed-Reflector Edge	T_a	Design Parameter (dB)
Feed-Reflector Cylindrical Coordinates	ρ_F, ϕ_F, z_F	(m) & (Degree)
Sub-reflector Diameter	D_S	5 ~ 10 (m)
Hyperboloid Sub-Reflector Focal Distance	$2c$	Design Parameter (m)
Hyperboloid Sub-reflector eccentricity	e	Design Parameter
Sub-reflector Cylindrical Coordinates	ρ_S, ϕ_S, z_S	(m) & (Degree)
Beam Cartesian Coordinates	x, y, z	(m)
Operating Frequency	f	1 ~ 22 (GHz)

Figure 1.1: Large Adaptive Reflector Antenna

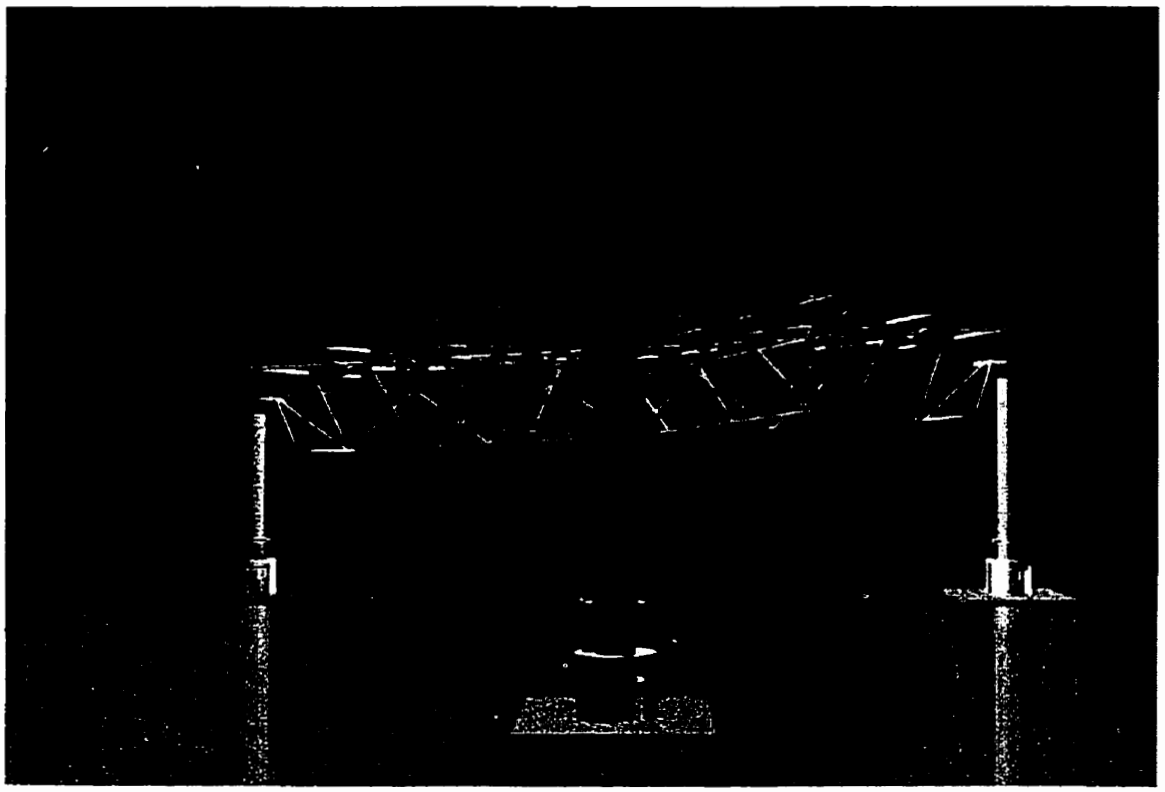

Figure 1.2: LAR flat panels supported by actuators on the ground

Chapter 2

BACKGROUND INFORMATION

The Feed-Reflector design for the LAR has taken advantage of many aspects of antenna design, such as radio telescope feed system, numerical techniques for reflector antennas, synthesis techniques, defocused paraboloid reflector, aperture antenna near field calculation, Gaussian beam analysis and offset reflector properties. In the following sections a short review of literature is provided.

2.1. Radio Telescope Feed Systems

Reber (1940) built the first radio telescope, using a paraboloidal reflector, almost 60 years ago. The world's largest fully steerable reflector was built in a valley of Eifle mountain near Bonn. This telescope has a 100 m diameter paraboloid reflector. It can operate at the wavelength as short as 1 cm, and can use either prime focus or Cassegrainian feed system.

The most famous of large radio telescopes is the 305 m diameter dish suspended in a mountain valley at Arecibo, Puerto Rico. Many feed options have been considered since its design. Love [20] designed slotted-waveguide line sources which can be swung through an angle of 20° from vertical, allowing beam scanning over a solid angle around the zenith of 6 percent of the sky above the horizon. Aperture efficiency of 53 percent with 16 dB sidelobes was obtained at 430 MHz. However, this feed system suffers from a

number of deficiencies [21] such as, ohmic losses which increase the noise temperature, and limited bandwidth which requires new line feeds, when new frequency bands are needed. To overcome these difficulties Kildal et al. [22] proposed a Gregorian dual reflector feed which is shown in Fig. 2.1. The idea of using a Gregorian-type sub-reflector, is to correct the spherical aberration.

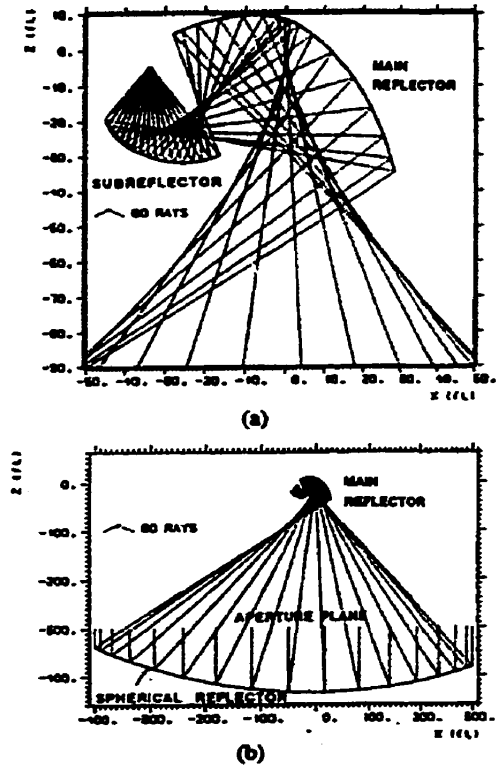

Figure 2.1: Cross section of Arecibo trireflector system a) Dual-reflector feed b) Total trireflector [22]

Kraus [23] designed the Ohio State University radio telescope which is shown in Fig. 2.2. It consists of a fixed standing-curved reflector and a tiltable-flat reflector. The

fixed-standing-curved reflector is a rectangular section of a sphere or paraboloid of revolution with the dimensions of 110 m by 21 m. The tiltable flat reflector dimensions are 104 m by 31 m. Two reflectors are joined by a flat conducting ground plane. Incoming rays are reflected by the flat reflector into the parabola which brings the rays to a focus at the ground level near the base of the flat reflector. The antenna feed system can work in two modes. In one mode (Fig. 2.3a) the feed horn axis is aligned with the centre of parabola and the ground plane is incidental. In the second mode (Fig. 2.3c) the horn axis is coincident with conducting ground plane. The ground plane serves as a guiding boundary surface. In this mode polarization should be vertical, and the feed horn required is 1/4 the height and 1/2 the length of the horn required in first mode.

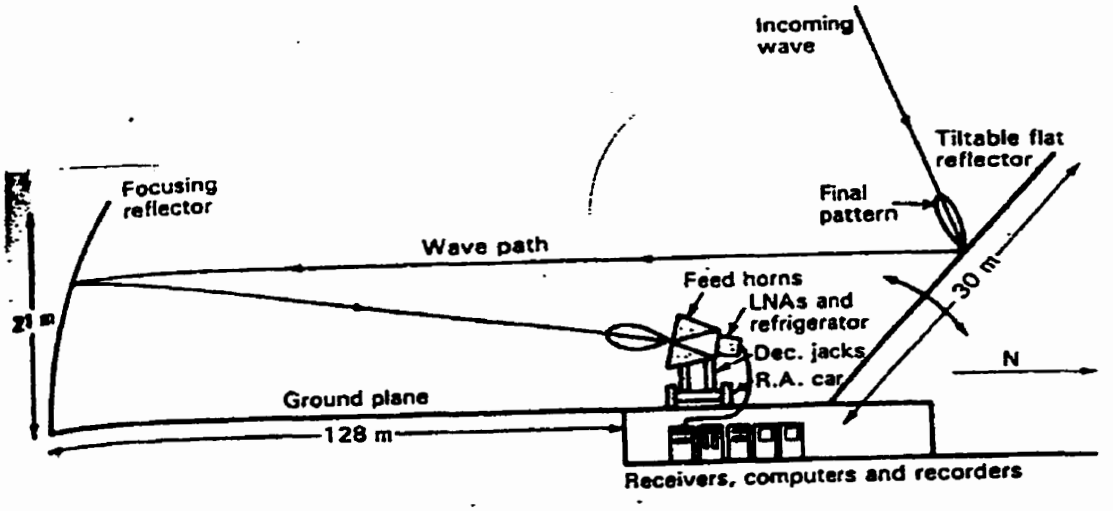

Figure 2.2: Elevation of cross section of Kraus radio telescope[23]

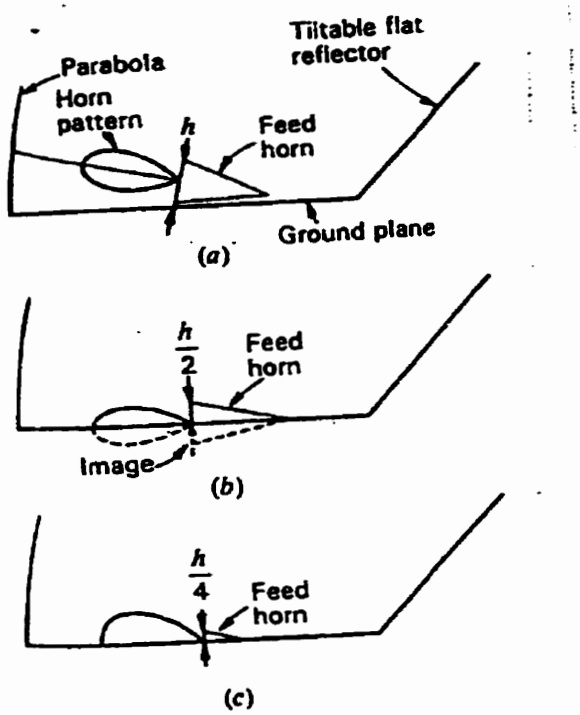

Figure 2.3: Arrangement for feeding antenna without ground plane, (a) requires 4 times horn height of arrangement at (c) using ground plane. Diagram (b) shows that half the horn in (a) produces too sharp a pattern when used with ground plane and must be reduced in size, as at (c).[23]

The other version of Ohio State radio telescope is Nancy (France) radio telescope which consists of a fixed spherical reflector 300 m long and 34.56 m high. The tiltable-flat reflector is 200 m long and 40 m high. The feed system is at the quasi- focus position of spherical reflector as shown in Fig. 2.4a. A new feed system was suggested by James et al. [24] for this telescope. This new feed system is based on using corrugated horn in dual-reflector Gregorian configuration which is shown in Fig. 2.4b. The proposed feed system uses the high performance wide band properties that can be obtained from a corrugated horn, while the designed Gregorian configuration transfers the horn's circularly symmetric radiation pattern to the highly elliptical pattern required to illuminate the fixed spherical reflector antenna.

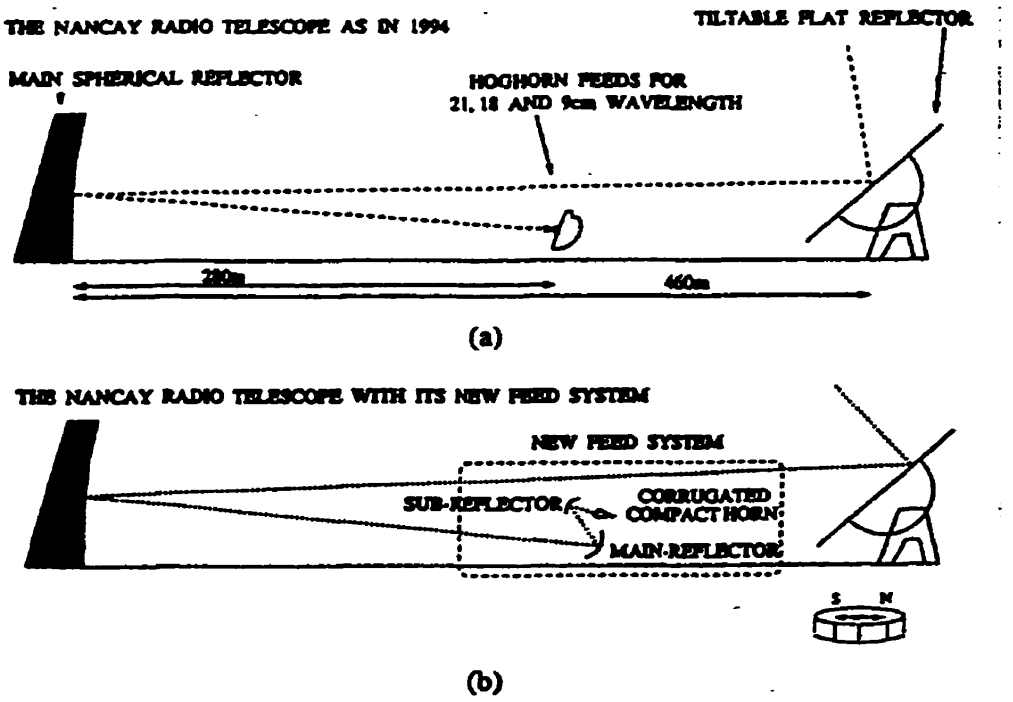

Figure 2.4: The Nancy radio telescope a) as in 1994 and b) with the proposed new feed system [24]

2.2. Numerical Techniques For Reflector Antennas

Efficient and accurate high frequency diffraction analysis techniques for reflector antennas have been investigated for many years. PO (Physical optics) is one of the techniques that has been used regularly in the analytical calculation of the radiation pattern of reflector antennas. Its simplicity, ability to accurately predict the far field pattern near the main beam, and the availability of efficient numerical techniques to perform the necessary surface integration make it popular[25]. Nevertheless, for accurate calculation of the fields

far from the main beam other techniques must be employed.

One of the methods which is able to estimate the fields at the far angles is Keller's Geometrical theory of diffraction (GTD)[26,27]. Aside from simplicity and accuracy, GTD can be made even more powerful by employing the uniform asymptotic theory (UAT) [28],[29] and the uniform geometrical theory of diffraction (UTD) [30], to remove its deficiency at the shadow boundary and reflection boundary. However, the singularities of GTD at caustics still remain in the uniform version. It is usually difficult to find the observation angle at which a switch between GTD and PO should be taken when the two methods are used together.

Another technique developed at the same time as GTD is the physical theory of diffraction (PTD) pioneered by Ufimtsev [31]. Two significant modifications to the original PTD have been obtained. The first is the application of the concept of equivalent edge current which removes the caustic singularities in the original ray tracing PTD. The second is an extension for observation angles. Ando's modified PTD [32] is one modification which uses the concept of equivalent edge current.

Mitzner, on the other hand, did not use equivalent edge current explicitly but rather expressed the PTD correction fields in term of incremental length diffraction coefficients (ILDC) [33]. When these coefficients are multiplied by the incident fields of arbitrary incident angles and integrated over the edge of the scatterer, one may determine the fringe field.

The third modification in PTD is Michaeli work[34]. He derived the GTD equiva-

lent edge current by asymptotically reducing the surface to edge integral. These currents were then written in terms of diffraction coefficients. It has been mentioned [35] that if the PO components are deducted from Michaeli's total scattered field, the fringe field constructed by Mitzner's ILDC are recovered. Later, Michaeli calculated the fringe current radiation integral over the ray coordinates instead of over normal coordinates, which corrected many of the singularities in Mitzner's ILDC [36].

2.3. Synthesis Techniques for Reflector Antennas

Many techniques have been proposed to solve the problem of synthesizing reflector antenna systems. Most of these methods are established based on principal of geometrical optics (GO). GO shaping of circularly symmetric dual-reflector antennas was formulated in terms of simultaneous nonlinear ordinary differential equations [37]-[39]. For offset dual-reflector antennas, the shaping problem can be described by a partial differential equation [40]. While, there has been a long controversy about the existence of the exact solution to the problem; but it has finally been accepted that several exact solutions are possible [41]-[43]. Another formulation of GO-shaping is based on the apparatus of complex coordinates [44], [45]. Other versions of the GO-shaping procedures can also be found in the literature [46]-[50].

A major drawback of the GO-shaping techniques is that diffraction effects are not incorporated in the process of reflector shaping. The diffraction effects that are ignored, include the near field effect between the feed and the reflector, that between the main and sub-reflector, and the diffraction from the surface and edges of the reflectors. The radiation

patterns of a GO shaped reflector antenna, when evaluated by the diffraction analysis techniques, may at times deviate from the desired pattern to the extent that stringent specifications such as very low sidelobe levels are violated. Due to this limitation, GO-shaping methods are essentially applicable to large antenna system where ray-tracing is an acceptable approximation. Another difficulty involving these techniques is that, array and aperture-type feeds (such as Feed-Reflector) may not be easily incorporated in the synthesis procedure. Although modifications of GO-shaping techniques have been suggested to overcome this difficulty [51],[52], they are mainly used as the initial designs for subsequent accurate diffraction synthesis.

It is noticed that in GO algorithms, one typically synthesizes the aperture field, from which the far field patterns are inferred. This is sometimes referred to as the "indirect" approach in contrast to techniques in which far field radiations are synthesized directly. The aperture field and radiated far field can be related by methods such as closed form formulas in pencil beam designs [53], [54], and optimization algorithms in contour beam designs [55]. A shaped reflector result from GO techniques is typically characterized by a set of discrete points, which may produce a surface that has discontinuities and irregular boundary. The interpolation procedure which is needed before fabrication may further add errors that degrade the radiation pattern.

To overcome the limitation associate with the GO shaping techniques, several methods have been investigated. Wood [56] carried out the first reflector shaping by diffraction synthesis using "Spherical Wave Expansion". Clarricoats et al. [57] employed reflector surface expansion and coefficient optimization that incorporated both GO algo-

rithm and physical optics analysis. This concept was further extended to methods that carry out full PO synthesis of reflector antenna with circular aperture and single feed. In the PO+PTD shaping introduced in [58,59] a set of orthogonal expansion functions was applied to represent reflectors with circular, rectangular or any intermediate rounded-corner shapes described by the superquadric functions[60]. This method can be applied to synthesize single, dual reflector with a single feed and array feed. Later Ramat-Samii introduced PO/GO analysis to this synthesis procedure [61], where the analysis of subreflector was carried out by GO Technique.

2.4. Aperture Near-Field and Defocused Paraboloid Reflector

The synthesis of axial field pattern has important applications to imaging apertures designed to achieve diffraction limited lateral and axial resolution by focusing in the Fresnel region. However, just few papers can be found in literature. In early 1960's Kay [3], Hansen [62], and Sherman [4] investigated the properties of focused aperture in Fresnel region. The issue remained intact until 1983 when Graham [5] showed the axial field pattern of an aperture focused in the Fresnel region can be synthesis in the same manner as the angular pattern of an aperture in Fraunhofer region. Later Shafai et al. [6], [10] considered the applications of near-field focusing aperture for array and reflector.

Before advanced antenna measurement facilities were introduced, people measured antennas in a test site. The trend toward higher operating frequencies and larger aperture dimensions for microwave reflector-type antennas has brought about the need for taking far-zone radiation patterns at distances too great for the average test site. This led to

a defocusing practice which the feed is displaced along axis of symmetrical reflector away from the surface in the attempt to simulate far-zone patterns in the Fresnel region [7]. Cheng[8] derived the first analytical solution for amount of defocusing in three ways, namely: i) The geometrical approach, ii) The aperture-phase approach, and finally iii) The ellipsoidal-reflector approach. However, he found inconsistencies among these approaches. Later Chu, in a communication [9], resolved this ambiguity.

The defocused far-field radiation pattern was the interest of Rusch when he published a paper [12] in 1973.

2.5. Gaussian Beam Methods

Quasi-optical propagation is hardly new. In fact, many of Hertz's and Bose's experiments at the end of nineteen century on the propagation, refraction, polarization and reflection of electromagnetic waves were carried out using apparatus only a few times larger than the wavelength employed [63, 64].

The modern era of quasi optics had its start in two quite distinct areas of research in the late 1950's and bore fruit in the early part of the following decade. The first was the study of modes in resonators operating at optical wavelengths, which were of great interest due to of their applications to lasers [65, 66]. The transverse field distributions of the low loss modes of the resonators consisting of a pair of reflecting mirrors were found to be Gaussian functions. Analysis of the variation of the electric field distribution as a function of position within the resonator yielded an understanding of Gaussian beam propagation.

Much of the early work in this field is summarized in the article by Kogelnik and Li [67].

The second line of investigation leading to the development of Gaussian beam theory was the study of beam waveguides, which are repeated sequences of lenses or mirrors designed to achieve low loss propagation of a beam of radiation over large distances. Analyses using diffraction theory revealed that the low loss electric field distribution in the beam waveguide is again essentially a Gaussian[68].

The significance of Gaussian beams, and the fundamental Gaussian mode in particular, is greatly increased by the high degree to which this relatively simple form represents the radiation pattern of different types of feed horns. These are critical elements for coupling to guided wave devices such as mixers and detectors. The analysis of radiation patterns in terms of Gaussian modes is carried out by expanding the electric field in the horn aperture in terms of a set of Gauss-Hermite or Gauss-Laguerre functions. If many modes are required to reproduce the aperture distribution, the Gaussian mode approach may be useful computational tool, albeit not an extremely simple one. Only if the fraction of the power in the fundamental mode is large, the radiation pattern in terms of a single Gaussian mode can be represented satisfactorily.

Corrugated or scalar feed horns are widely used at the millimetre wavelengths, and have an aperture field distribution which ideally is of the form $J_o\ (\alpha\rho/a)$, where $\alpha = 2.405$ and a is the aperture radius [69]. Since this Bessel function is quite similar to $exp[-(\rho/W)^2]$ (W is the beam radius), it is expected that the fundamental Gaussian mode alone to be a good representation of the aperture field. Indeed, for W/a = 0.64, 98% of the radiated power is in the fundamental mode [70-72].

2.6. Offset Reflectors

The offset parabolic reflector has found application as an antenna for many years and was certainly receiving some attention during 1940s. However, it is only in recent times that analytical and numerical models have been developed for this antenna[73]. Much of the initial difficulty in dealing with offset parabolic reflector can be attributed to its asymmetric geometry. This geometry is the key to the analysis of the offset antenna and to ultimately understanding its electrical properties. One of the best analyses of the offset reflector geometry can be found in a monograph issued by the Bell Telephone System [74]. The depolarization properties of asymmetric antennas have deservedly received considerable attention in the literature. The polarization characteristics of the offset reflector were subject to the independent study of a number of authors like the work by Chu and Turrin [75]. Some important features of offset reflectors were demonstrated in [76].

For applications involving complex primary-feed structures, the use of a Cassegrainian feed system has some obvious advantages. In particular, the Cassegrainian configuration allows the feed elements and the associated circuitry to be located close to the main reflector surface possibly avoiding long RF transmission paths and the need for extended feed support structure while the forward pointing feed format can be a desirable attribute for applications requiring low noise performance.

Of the variety of offset Cassegrainian systems proposed in the literature, perhaps the best known is the open Cassegrainian antenna introduced in 1965 by the Bell Telephone Laboratories[74]. The antenna, which is illustrated in Fig.2.5c comprises an offset

section of a paraboloid an offset hyperboloid sub-reflector, fed by a primary feed which protrudes from an aperture in the main reflector surface.

An alternative dual-offset reflector configuration, which offers a number of attractive features, is the so-called double-offset antenna shown in Fig. 2.5a. This antenna, which was first implemented by Graham [77] provides a convenient location for the primary feed hardware by use of an offset section of a hyperboloidal sub-reflector in a Cassegrainian configuration. Two arrangements of the double offset are shown in Fig. 2.5.

Analyses performed by several researchers [78-83] have shown that the double offset antenna can be designed such that, when fed by a conventional linearly polarised primary feed, the depolarisation arising from the two offset reflectors can be made to cancel. Thus providing an overall low cross-polar characteristic. This performance is achieved by matching the scattered radiation fields from the sub-reflector to the main reflector.

Approximate techniques based upon the use of geometric optics indicate that a perfect mach can be achieved when the axis of the parent sub-reflector is depressed by an angle β from the axis of the parent paraboloid. This condition is illustrated in Fig. 2.5b. A mathematical expression relating the depression angle β to the parameter of the sub-reflector was derived by Mizugutch [79]. In its simplified form this can be expressed as

$$\tan\left(\frac{\beta}{2}\right) = \frac{1-e}{1+e}\tan\left(\frac{\alpha}{2}\right) \qquad (2\text{-}1)$$

where e is the eccentricity of the sub-reflector, α is the feed offset angle.

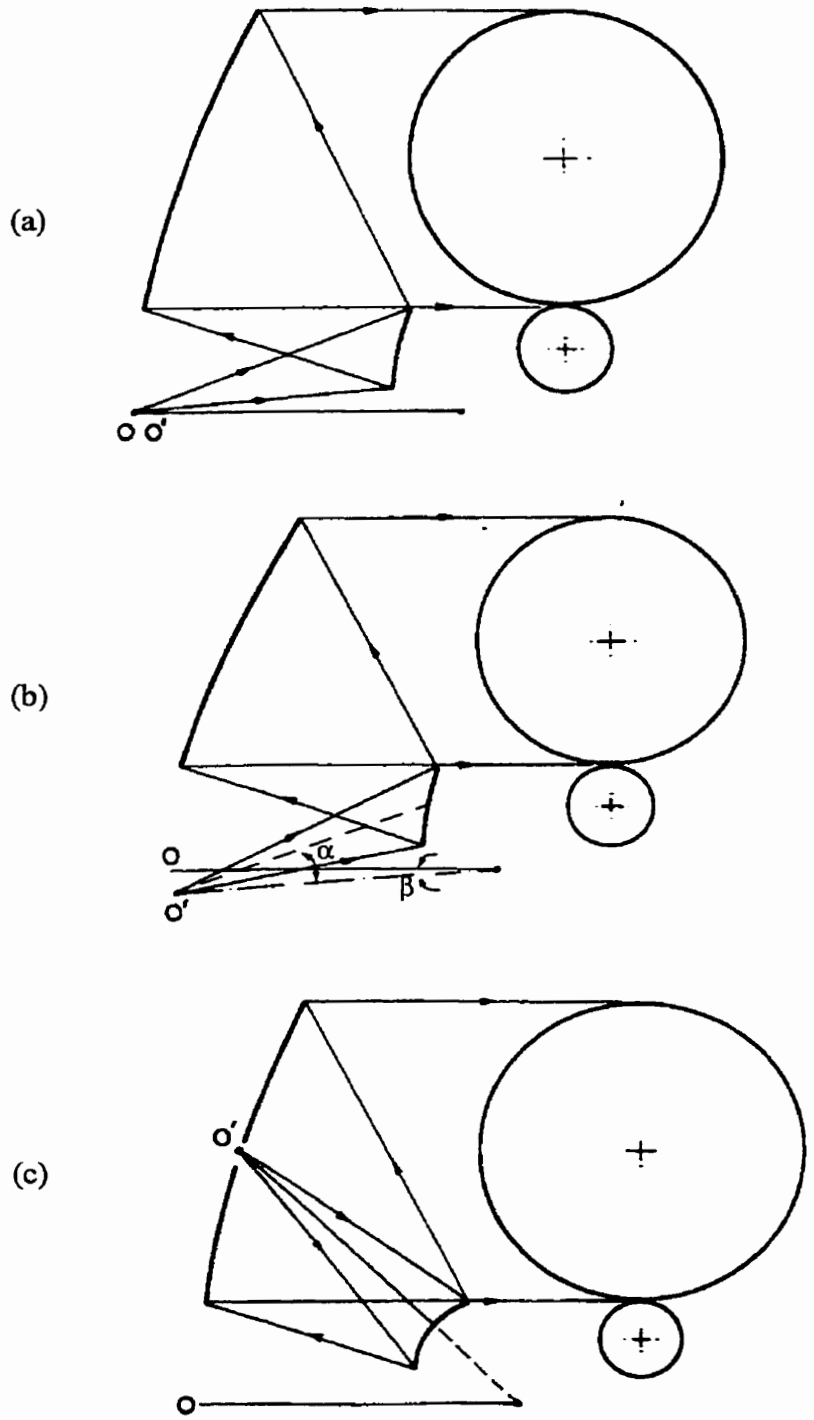

Figure 2.5: Dual-offset reflector configurations: a) Double offset system; b) Optimised double offset; c) Open Cassegrainian system [73] (paraboloid vertex at O and feed phase centre located at O')

Chapter 3

THEORY OF THE FEED-REFLECTOR

3.1. Introduction

The main element in the design of the LAR fed from the ground is the Feed-Reflector antenna. Due to the large aperture size D_F, of the Feed-Reflector, the sub-reflector is located in its Fresnel region (i.e the distance R, between the feed and sub-reflector is less than $2D_F^2/\lambda$ [73]), for almost all of the operating frequencies. Thus, the paraboloid Feed-Reflector needs to focus in the Fresnel region instead of Fraunhofer region. This issue was the concern of researchers in late 1950's. At that time the trend toward higher operating frequencies and larger aperture dimensions for microwave reflector antennas brought about the need for taking Fraunhofer region radiation patterns at distances far too great for the average available test site. This led to a defocusing practice whereby the antenna feed was displaced along the principal axis away from the reflector in the attempt to simulate far-zone patterns in the optical Fresnel region. The amount of defocus required for given test site was by approximated a geometrical optics method.

This chapter will establish a theory for the design of a paraboloid Feed-Reflector to generate radiation pattern similar to a feed horn. In this theory, the properties of axial defocused paraboloid reflectors at near distances are investigated in more detail. By using equivalence path law, the sub-reflector shape is obtained. It is found that a hyperbola can approximate the sub-reflector well.

3.2. Defocused Paraboloid Reflector Relations

The above mentioned theory is established based on the near field focusing properties of aperture antennas. The field in the Fresnel region of a circular aperture can be calculated by the following diffraction integrals [84].

$$U_p = \frac{j}{\lambda}\frac{e^{-jkR}}{R}\int_0^{2\pi}\int_0^{a} F(\rho', \phi') e^{jk\rho'\sin\theta\cos(\phi-\phi')} e^{-jk\frac{\rho'^2(1-\sin^2\theta\cos^2(\phi-\phi'))}{2R}} \rho' d\rho' d\phi' \quad (3\text{-}1)$$

where ρ', ϕ' are the radial, and angular dimensions of aperture plane. $a = D/2$ (Fig. 3.1a), θ and ϕ are zenith and azimuth angle of observation point respectively, and $F(\rho', \phi')$ is the amplitude illumination function over the aperture. The term $e^{-jk\frac{\rho'^2}{2R}(1-\sin^2\theta\cos^2(\phi-\phi'))}$, introduces quadratic phase error and is necessary for calculating the near-field of apertures (i.e. when R is in the near distance). In this equation terms of order greater than $1/R$ are discarded. In the neighbourhood of z-axis or focal region, $\sin^2\theta \approx 0$, and the term inside the bracket of this second exponential reduces to unity which facilitates the calculation of the radiation pattern.

The simulation of Fraunhofer radiation patterns in the Fresnel region of paraboloid reflector antennas was previously discussed in [8]. The general practice is to defocus the primary source of the reflector by a small distance, along the principal axis in a direction away from the paraboloid reflector surface.

A symmetric paraboloid reflector can be represented by an aperture Fig. 3.1b. When the primary source is displaced from the focus of the paraboloidal reflector along the reflector axis away from the reflector, a quadratic phase error (aberration) on its

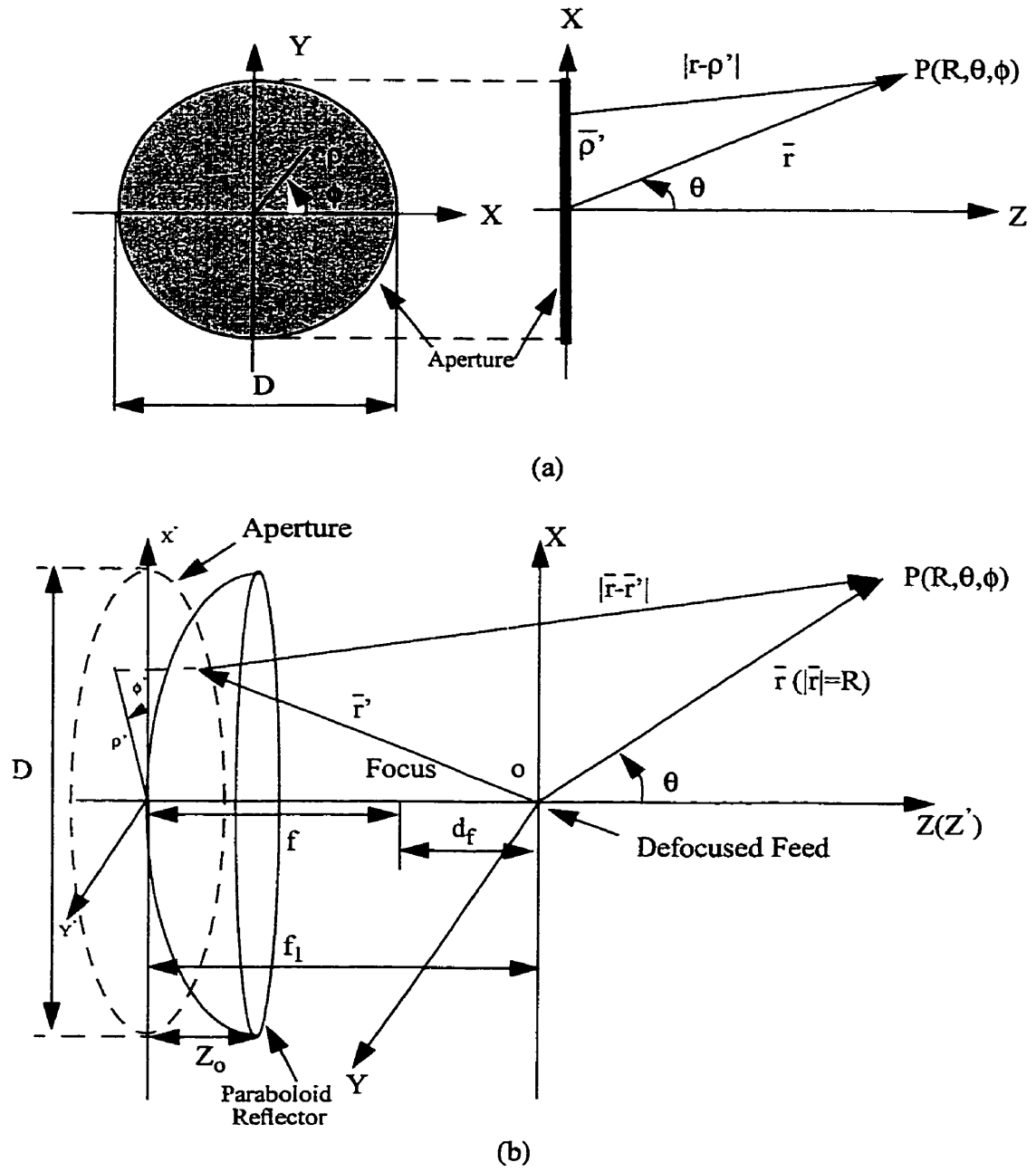

Figure 3.1: a) Aperture near-field scheme b) Reflector near-field scheme

aperture surface is uced. The quadratic phase error due to the defocused feed is [7],

$$\delta = -2d_f/(1+\rho'^2/4f^2) \tag{3-2}$$

where f is focal length, d_f is defocus distance, and (ρ',ϕ',z') are cylindrical coordinate system of paraboloid reflector aperture.

In this case for the reflector antenna in Fig. 3.1b, the phase term $|\bar{r}'-\bar{r}|$ in Fresnel region becomes

$$|\bar{r}-\bar{r}'| \cong R-\rho'\sin\theta\cos(\phi-\phi')-z'\cos\theta + \frac{\rho'^2[1-sin^2\theta cos^2(\phi-\phi')]+z'^2[1-cos^2\theta]-\rho'z'\sin 2\theta\cos(\phi-\phi')}{2R} \tag{3-3}$$

Again the region of interest is the focal region of the reflector, i.e. near the z-axis where the following small angle approximation is valid: $1-cos^2\theta \approx 0$, $1-sin^2\theta cos^2(\phi-\phi') \approx 1$, and $\rho'^2 \gg \rho'z'\sin 2\theta\cos(\phi-\phi')$ resulting in:

$$|\bar{r}-\bar{r}'| \cong R-\rho'\sin\theta\cos(\phi-\phi')-z'\cos\theta+\frac{\rho'^2}{2R} \tag{3-4}$$

The last term in right hand side of the above equation shows the quadratic phase error of the paraboloid reflector which is similar to Eq.(3-1) for the aperture antenna. At the focal plane this quadratic phase error cancels that in Eq.(3-2), and leaving the well known diffraction integral with a linear phase function. In other words, using the aperture field integrals, introduction of a quadratic phase error on its aperture field brings the far field radiation pattern to the focal field. Eq.(3-5) shows the total diffraction integral of the defocused reflector at a distance R [15].

$$\bar{E} = -jk\eta \frac{e^{-jkR}}{4\pi R} \int_0^{2\pi} \int_0^a \bar{J}(\rho', \phi') e^{jk\rho' \sin\theta \cos(\phi - \phi')} e^{jkz' \cos\theta} e^{jk\delta} e^{-jk\frac{\rho'^2}{2R}} \rho' d\rho' d\phi' \qquad (3\text{-}5)$$

where $\bar{J}(\rho', \phi')$ is the current distribution on the aperture of the reflector antenna shown in Fig. 3.1b.

Fig. 3.2 shows the results of ray tracing over a defocused paraboloid reflector. By moving the feed away from the focal point, the rays reflecting from the reflector surface cross the symmetrical axis somewhere on a line (paraxial focus) ended at P'. The ray hitting the surface of reflector at $Q(\rho', z')$ intersects the symmetric axis of the reflector at the point $P(0,R)$ where R can be calculated as

$$R = f + \frac{f^2}{d_f} + \frac{\rho'^2}{2d_f} + \frac{\rho'^4}{16 f^2 d_f} \qquad (3\text{-}6)$$

In Fig. 3.2, $OF = f$ is the focal length of the Feed-Reflector, and $FF' = d_f$ is the feed defocus distance. The starting point of the paraxial focus is $O'(0,R_o)$

$$\lim_{\rho' \to 0} R = f + \frac{f^2}{d_f} = R_o \qquad (3\text{-}7)$$

$M(0,R_m)$, the point on the paraxial focus where the maximum energy density occurs, is located along the paraxial focus. For focusing at this point the amount of defocusing is calculated by [8]

$$d_f = \frac{f^2}{R_m}\left[\left(\frac{R_m}{R_m - f}\right) + \left(\frac{D}{4f}\right)^2\right] \qquad (3\text{-}8)$$

As an example, a 25 meter reflector with f/D=0.36, and defocusing distance d_f is

considered. Sample power distribution on the symmetric axis is shown in Fig. 3.3, for different values of defocusing distances. This figure shows for each value of defocusing distance there is a point on the paraxial focus, where the energy density is maximum.

3.3. Feed-Reflector Size

It was shown in the last section that the field pattern obtained by Eq.(3-5) is equivalent to the far-field [5]. This field equivalence can remain almost linear for distances between the aperture and its image, as small as the aperture size. In this range the focusing property is governed by the aperture phase distribution and the field intensity variation is less important. In the other words, the terms with the order higher than $1/R$ can be neglected (Fig. 3.1b). However, at distances less than the aperture size, the field intensity variation dominates and the image plane field distribution losses its primary dependence on the aperture phase, i.e. higher order terms are significant. In the present study the distance of the sub-reflector is much larger than the Feed-Reflector diameter and so the field intensity dependence does not occur. Thus, the focal plane field distribution remains identical to the far field shape at infinity.

The above relationship allows a quick study of the focal plane field. The geometry for a cross section of circular aperture is shown in Fig. 3.4, where D_F is the aperture size, R is its distance from the focal plane. The important parameters of the focal plane field are its 3 dB beamwidth and beamwidths of the main beam nulls, and the sidelobe levels. Their angular dependence remains the same as those of the far field distribution. To study

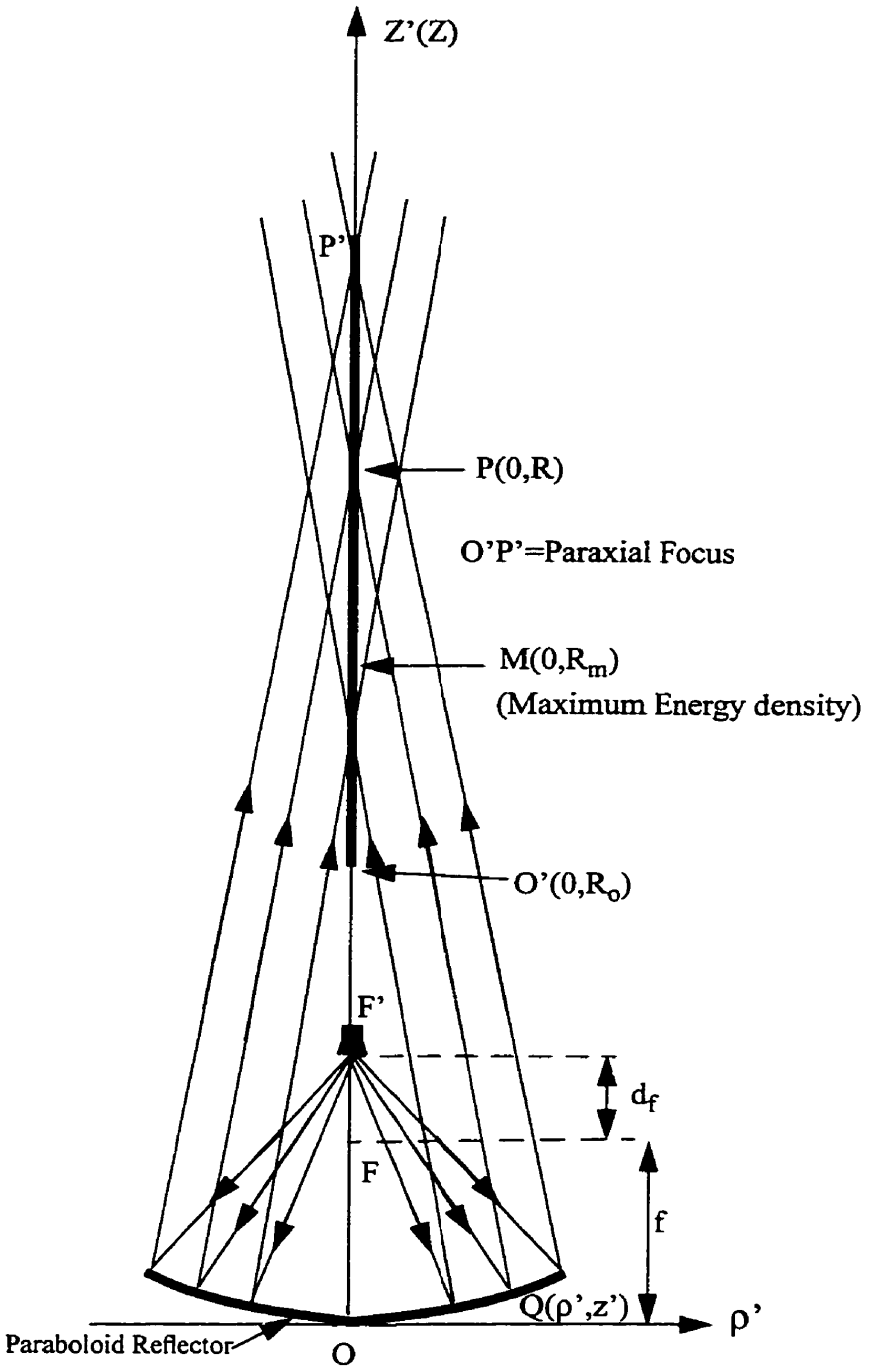

Figure 3.2: Ray tracing for a defocused paraboloid reflector antenna

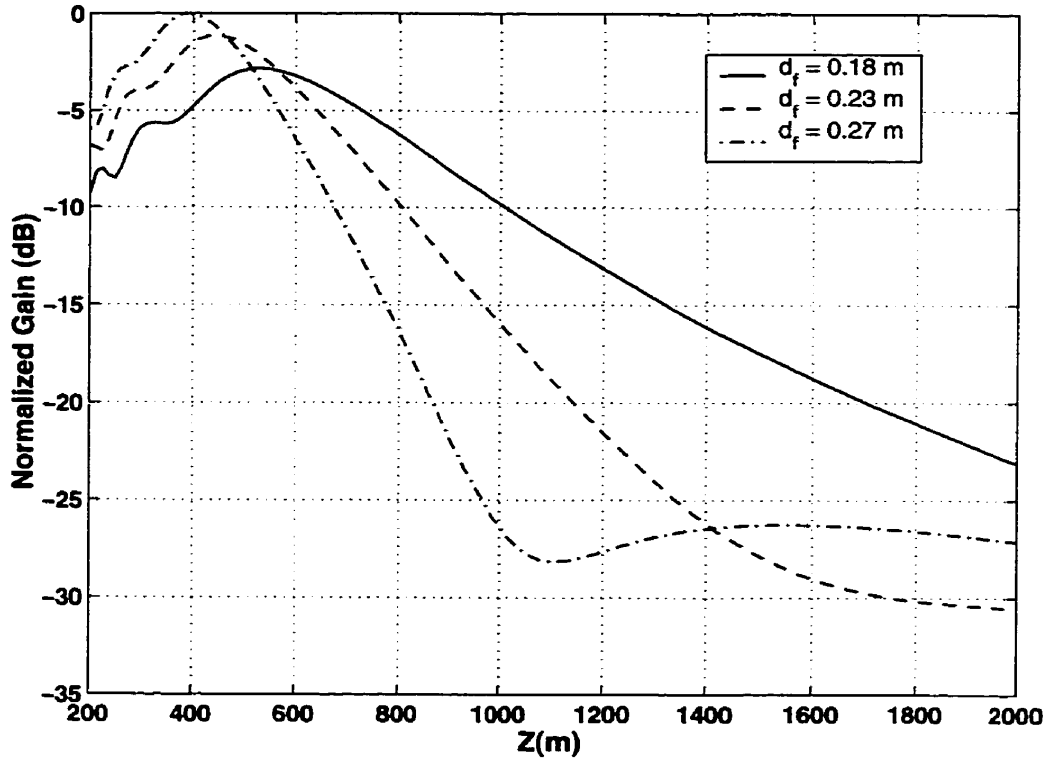

Figure 3.3: Axial power distribution of a reflector focused in its near field

the sub-reflector illumination, the beamwidth can be translated into a spot size on the focal plane, representing the equivalence of Airy disks in optics. The aperture theory can then be used to calculate the beamwidths, spot sizes, sidelobes and gain.

The objective here is to generate simple relationships to determine the focused spot sizes which they are simply proportional to the ratio of R/D_F, a linear relationship [10]. For a circular aperture, the far field and that in the image plane resemble $J_1(x)/x$. The main beam generally contains most of the power and nearly 90% [85] for the focal region of the paraboloid. Thus, if the size of the sub-reflector is selected equal to the null-to-null spot

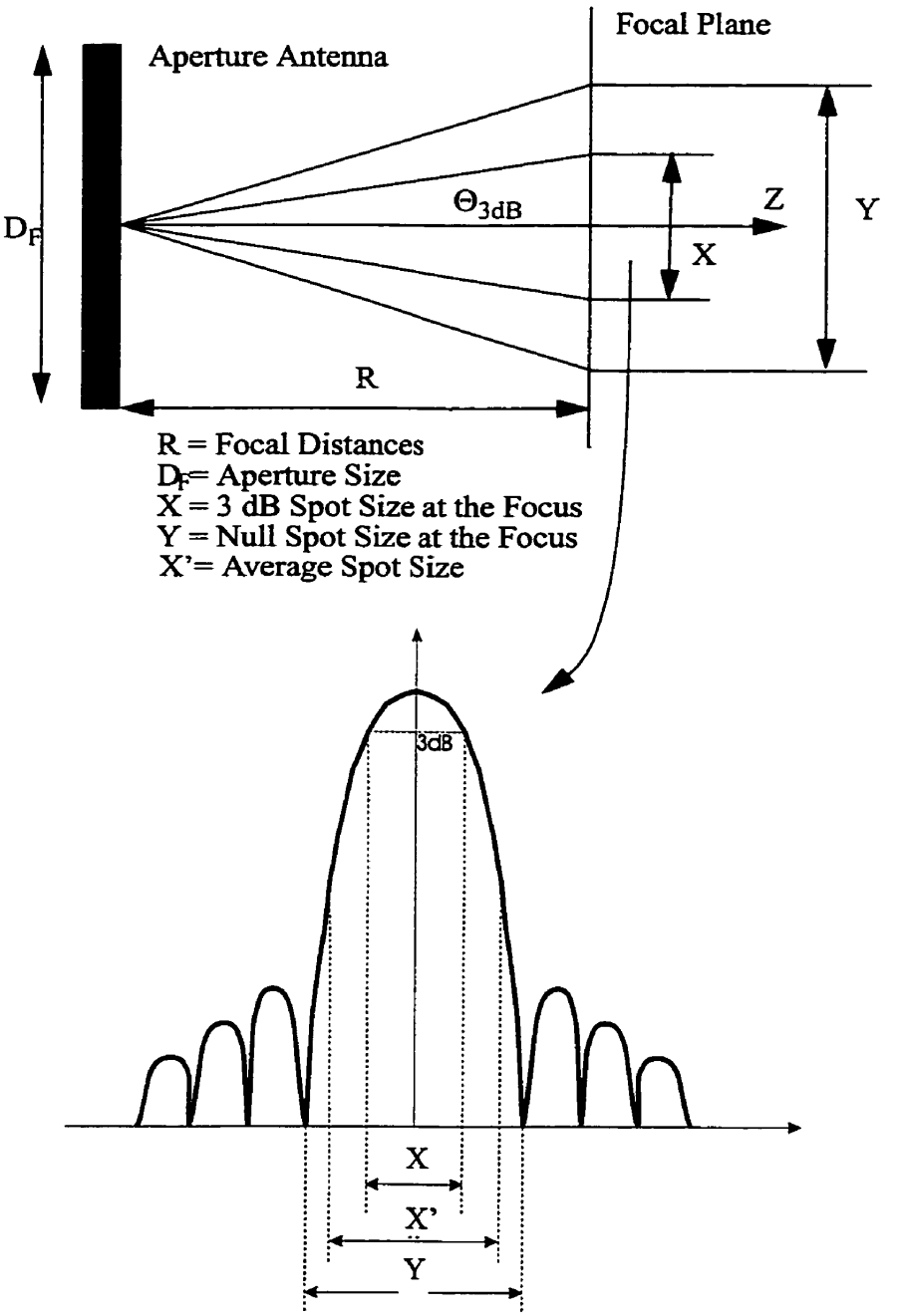

Figure 3.4: An aperture antenna focus to a distance R, and field distribution on the focal plane of a circular aperture antenna

size of the Feed-Reflector, it intercepts the same percentage of the power, i.e. 90% (Fig.3.4). However, in practice, this may result in an oversized sub-reflector, which has zero (i.e. $-\infty$ dB) edge illumination. More realistic edge illuminations of between -10 dB to -20 dB are normally selected in practice, without significantly reducing the power interception efficiency of sub-reflector.

To calculate the Feed- Reflector diameter, D_F, to feed a sub-reflector with diameter D_S, the following circularly symmetric aperture distribution is selected[73].

$$F(\rho_F) = B + (1-B)(1-\rho_F^2/a^2)^n \tag{3-9}$$

where n=2, and B=-18 dB (a close approximation for Feed-Reflector aperture distribution of next chapter). ρ_F is the radial dimension of aperture plane of Feed-Reflector. The 3 dB, and null-to-null spot size are (from Fig. 3.4)[73]

$$\frac{X}{R} = \tan(\theta_{3dB}) \cong \theta_{3dB} = 1.31\frac{\lambda}{D_F} \tag{3-10}$$

$$\frac{Y}{R} = \tan(\theta_{Null}) \cong \theta_{Null} = 3.665\frac{\lambda}{D_F} \tag{3-11}$$

A reasonable selection may be their average, such as

$$Average\ spot\ size = X' = 1/2[1.31+3.665](R/D_F)\lambda = 2.49(R/D_F)\lambda \tag{3-12}$$

Now, assuming the sub-reflector size D_S is equal to the average spot size, it gives a simple relationship of D_S=X'. Thus, for a LAR with D_S=5 ~10 m, and R = 500 m, one can find the required aperture size of the Feed-Reflector as [88, 89]

$$D_F = 2.49(R/D_S)\lambda \tag{3-13}$$

3.4. Sub-Reflector Profile

As can be seen from Fig. 3.2, replacing a horn antenna by the Feed-Reflector antenna imposes new conditions on the Cassegrain system. In this new system the rays converge, while for a horn antenna they diverge. The sub-reflector should be placed somewhere on the paraxial line as shown by Eq.(3-8), to intercept maximum energy. However, by locating the sub-reflector at this place, two or more reflected rays from the Feed-Reflector may pass through each point of sub-reflector surface. This means the sub-reflector surface should be approximated after being corrected [86] for uniform phase distribution over the LAR aperture.

Fig. 3.5 shows a family of incoming rays ($\overline{F'O}$, $\overline{F'P}$, and $\overline{F'G}$) emanating from a horn antenna. The equations for correcting the sub-reflector surface are obtained by requiring all rays to have equal path lengths as measured from a reference wavefront passing through F', that is

$$\overline{F'P} + \overline{PP'} + \overline{P'Q'} = \overline{F'O} + \overline{OB} + \overline{BQ} \tag{3-14}$$

where Q, and Q' are points in a circle with the centre at F_1, and radius a. F_1 is the focus of the sub-reflector which coincides with LAR focus. The various coordinates and the surfaces or points are defined as follows [90]:

$(\rho_F z_F)$ Feed-Reflector surface

$(\rho_S z_S)$ Sub-reflector or Corrector surface as referred in [86]

$B(0,b)$ vertex of sub-reflector

$F_1(0,2c)$ upper focus of the sub-reflector

$F'(0, f_F+d_f)$ feed horn location

$I(0,R)$ cross section of a ray and symmetric axis Eq.(3-6)

Eq.(3-14) can now be expressed as:

$$\sqrt{\rho_F^{\,2}+(z_F-f_F-d_f)^2}+\sqrt{(\rho_F-\rho_S)^2+(z_F-z_S)^2} -\sqrt{\rho_S^2+(z_S-2c)^2}+a \;=\; 2b-2c+a+f_F+d_f \tag{3-15}$$

In Fig. 3.5, calculation of relation between $(\rho_F z_F)$ and (ρ_S, z_S) yields

$$\frac{\rho_F}{R-z_F} \;=\; \tan\theta \;=\; \frac{\rho_S}{z_S-R} \tag{3-16}$$

Simultaneous solution of Eqs.(3-15), and (3-16) for the coordinates (ρ_S, z_S) of the sub-reflector surface yields

$$z_S \;=\; \frac{A^2(z_F)-2A(z_F)\dfrac{R}{\cos\theta}-4c^2+R^2}{2R-4c-2\dfrac{A(z_F)}{\cos\theta}} \tag{3-17}$$

$$\rho_S \;=\; \tan\theta(z_S-R) \tag{3-18}$$

where

$$A(z_F) \;=\; \frac{R-z_F}{\cos\theta}-2b+2c-f_F-d_f+\sqrt{\rho_F^{\,2}+(z_F-f_F-d_f)^2} \tag{3-19}$$

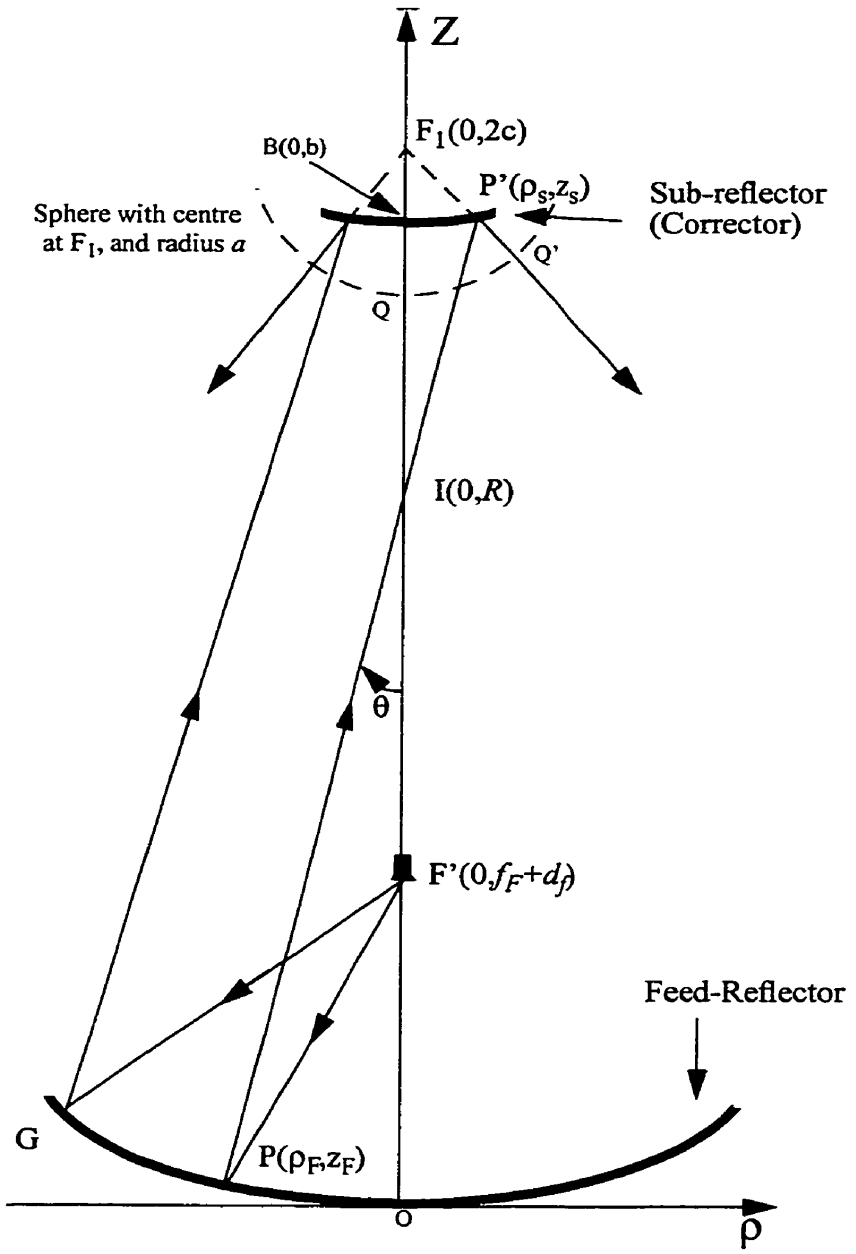

Figure 3.5: Paraboloid Feed-Reflector and sub-reflector (corrector)

The plot of Eqs.(3-17), and (3-18) is shown in Fig. 3.6. The solid curve in this figure shows the only solution for the sub-reflector corresponding to a Feed-Reflector with a 25 m diameter, 9 m focal length, and the defocusing distance of 0.23 m. It can be seen that for ρ_S less than $|\rho_{SA}|$, three values exist for z_S, where each is related to a ray coming from different location of the Feed-Reflector. Parameter b, which fixes the vertex of sub-reflector, is an important parameter in designing the LAR Cassegrain, because it determines the curvature of the sub-reflector and consequently the portion of LAR which must be illuminated. In Fig. 3.6, b is considered to be 489.824.

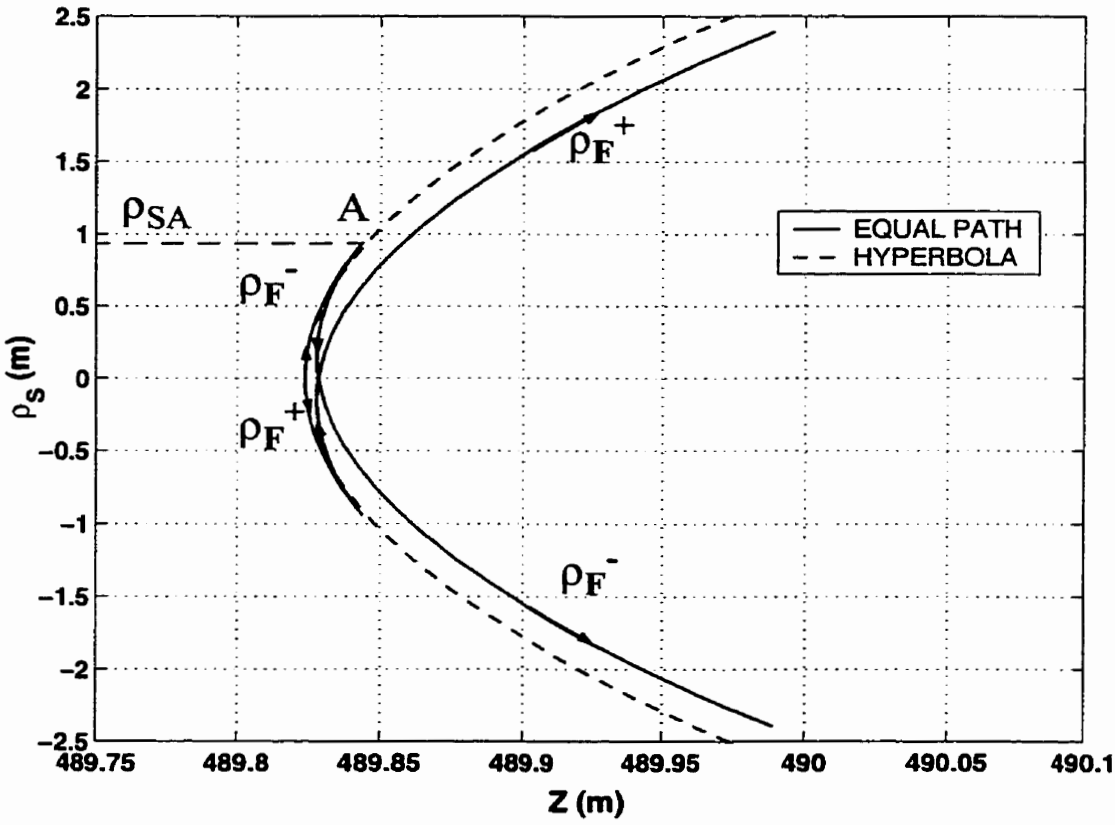

Figure 3.6: Sub-reflector surface and its hyperboloid approximation.

The surface plotted in Fig. 3.6 is not physically realizable and must be approximated by another surface. In the next chapter it is demonstrated that hyperbola is the best fitted surface for this system.

3.5. Conclusion

The Feed-Reflector concept was introduced in this chapter. The feed was based on the near field focusing properties of reflector antennas. The theory of this feed system was established by using the defocused paraboloid reflector characteristics and the aperture theory. It was found that feed defocusing distance can be approximated well by the formula developed by [8]. An approximated formula was developed to estimate the illuminated portion of the Feed-Reflector antenna (-15 dB taper at the edge). By employing the concept of equal ray path theory, the sub-reflector profile was obtained.

Chapter 4

CHARACTERISTICS OF THE SYMMETRICAL CASSEGRAIN LAR SYSTEM WITH FEED-REFLECTOR

4.1. Introduction

To verify the theory derived in chapter 3, a paraboloid reflector with D_F=25 m and a focal length of f_F=9 m is considered. Performance of the LAR and Feed-Reflector are investigated by changing the feed system parameters. These parameters are the feed horn defocusing distance d_f, and field taper T_a at the Feed-Reflector edge. A detail ray tracing is performed on the entire system. The performance of the system over the operating band (1-22 GHz) is also studied in this chapter. To obtain higher efficiencies, three sets of shapings, based on genetic algorithm and Jacobi Fourier surface expansion, are performed. However, before proceeding to this stage, it is instructive to consider the sub-reflector shape and investigate its relevant system performance.

4.2. Sub-Reflector Formulation

The geometrical parameters of a Cassegrain LAR system with a paraboloid Feed-Reflector are shown in Fig. 4.1. The field taper at the Feed-Reflector edge is considered to be -15 dB, and d_f=0.23 m. The sub-reflector diameter is chosen to be 5 m. The influence of these parameters on the LAR performance are discussed later. The effect of blockage is taken into account by removing the central portion of the LAR, the radius of which is

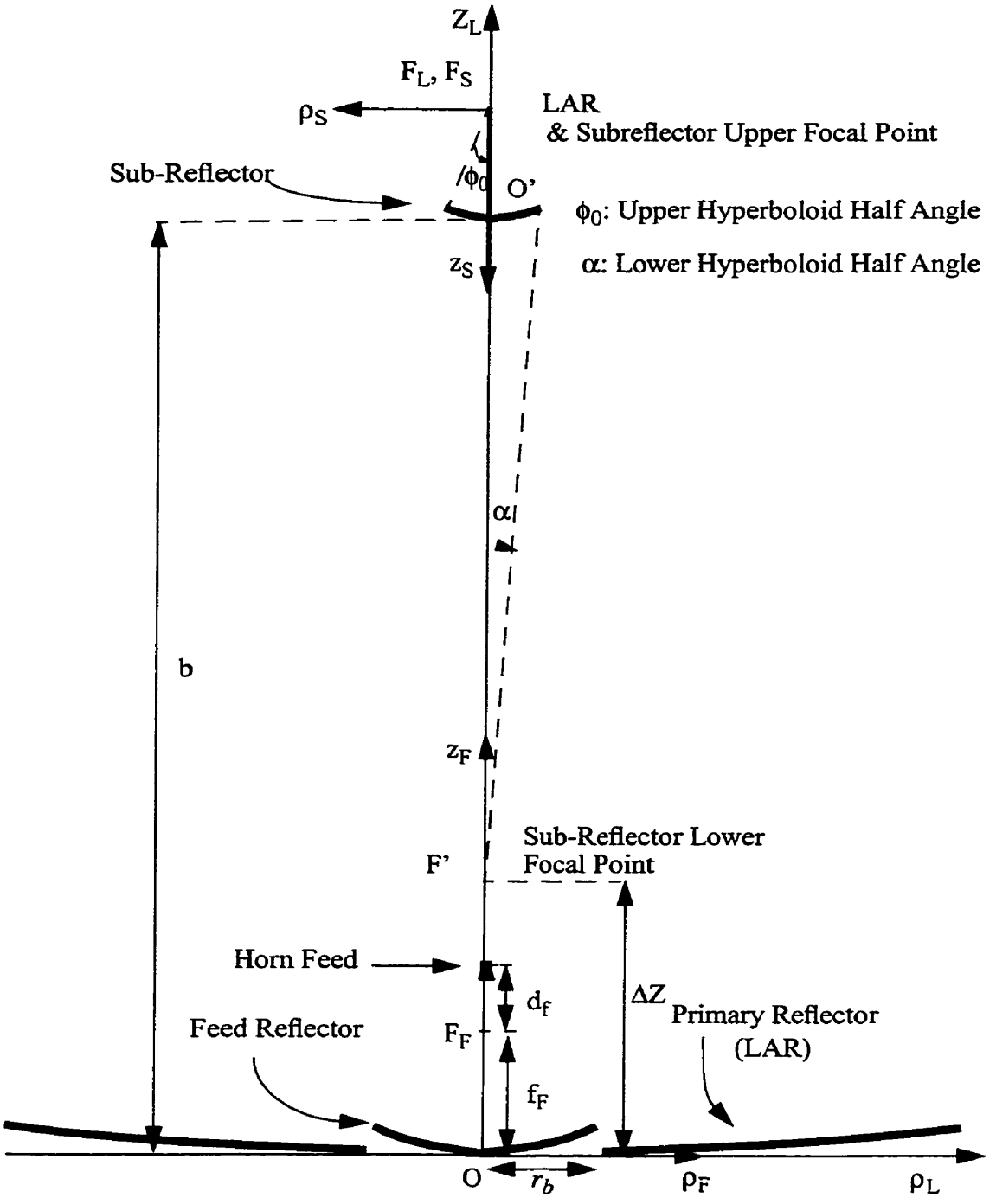

Figure 4.1: Cross section of Large Adaptive Reflector Cassegrain system (Not scaled)

r_b = 15m, or 15% of the LAR radius (Fig.4.1). The operating frequency is assumed to be 3 GHz.

To make it feasible for fabrication, it is preferable to estimate Eqs.(3-17) and (3-18) with the simplest configurations. One of these configurations is a conventional sub-reflector with conical section. To accomplish this goal, a hyperboloid is considered. One of its focal points is located on the LAR focus F_L, and the other focal point on the Feed-Reflector vertex, O. For ($\Delta Z = 0$), the Feed-Reflector vertex coincides with that of the LAR is considered. Thus, the hyperboloid reflector inter-focal distance $2c$ is 500 m. The equation of the hyperboloid can be determined by selecting parameter b, which is the distance between hyperbola vertex O' and LAR vertex O,

$$\frac{z_S^{\,2}}{(b-c)^2} - \frac{\rho_S^{\,2}}{2bc-b^2} = 1 \tag{4-1}$$

which is drawn in Fig. 3.6 for b = 489.824. Other parameters of the hyperboloid sub-reflector are

$$2c = \frac{d}{2}(\cot\alpha + \cot\phi_0) \tag{4-2}$$

$$M = \tan\frac{\phi_0}{2}\cot\frac{\alpha}{2} \tag{4-3}$$

$$e = \frac{M+1}{M-1} \tag{4-4}$$

where α, ϕ_0 are the lower and upper hyperboloid half angles respectively, M is the Cassegrain magnification, and e is the hyperboloid eccentricity.

4.3. Performance of Hyperboloid Sub-Reflector in the LAR System

To investigate the properties of the LAR Cassegrainian system with a hyperboloid sub-reflector, the radiation pattern of the system shown in Fig. 4.1 for D_F=25 m, f_F=9 m, d_f=0.23 m, T_a = -15 dB (Taper at the edge of Feed-Reflector) D_S=5 m, $2c$ = 500 (inter - focal distances) and e =1.0424 (b =489.824, dash curve in Fig. 3.6), is calculated and displayed in Fig. 4.2. The efficiency of the system is 72.0% which is related to a directivity of 74.52 dBi at 3 GHz. The half power beamwidth, HPBW, is 0.03°. The diffraction cross-polarization (feed horn is assumed to be ideal and have no cross-polarization) and first side lobe level are -71 dB and -19.04 dB below maximum directivity respectively, which are in acceptable range [87]. The cross polarization is calculated in the 45° plane. The sub-reflector field induces a taper of -9.5 dB at the edge of the LAR, while the taper at its edge due to the Feed-Reflector is -13 dB.

The calculated result for the co-polarized pattern, using PO on each reflector surface, is compared to that of the GRASP8W, good agreement is evident. Implementation of body of revolution techniques remarkably facilitate the computation of radiation pattern. In this calculation the effect of the Feed-Reflector parasitic fields on the LAR radiation patterns is taken into account. This parasitic fields are due to the current induced by the sub-reflector on the Feed-Reflector. It is observed that the Feed-Reflector radiation pattern has impact only on the LAR sidelobes which are located at least 10 beamwidth away from the main lobe. In the analysis of sub-reflector adding the PTD to PO has a considerable impact on the LAR cross-polarization similar to ordinary Cassegrain system [18]. A 10 dB increase in the diffraction cross-polarization of the LAR radiation pattern is observed by

using the PTD compared to pure PO analysis. However, the impact of adding PTD on the Feed-Reflector and LAR, on the system cross-polarization is not considerable.

In ordinary Cassegrain systems, the lower focal point is normally located on the phase centre of the feed horn. The rays diverge from the phase centre and cover the surface of the sub-reflector. However, in the case of the Feed-Reflector, there is no specific point to locate the lower focal point. To investigate the effect of the lower focal point on the results, its position was changed with respect to the LAR or the Feed-Reflector vertex (ΔZ), while the upper focal point was located on the LAR focus. It is observed that as long as $|\Delta Z| < D_F$ the variation in directivity is not significant for above parameters. The effect of inter-focal distance will be explained in chapter 5 in more details.

A full ray tracing study was performed on this configuration. Figs. 4.3, and 4.4 show the ray tracing result for the LAR. Since the reflectors are rotationally symmetric only a cross section of the structure can be utilized for analysis. To illustrate the ray tracing sequence, five rays are selected and numerically assigned in Figs. 4.4a and 4.4b. Rays number 1, 2, and 3 which are emitted from the horn antenna and being reflected from left side of the Feed-Reflector symmetric axis, intercept the sub-reflector on the right side of the symmetric axis. But ray number 3 which incident farther away from the Feed-Reflector axis compared to ray number 2, i.e. $|\rho_{F3}|>|\rho_{F2}|$, intercepts the sub-reflector closer to the sub-reflector axis, i.e. $|\rho_{S3}|<|\rho_{S2}|$. Rays 4, and 5 which are reflected far away from the symmetry axis (relate to rays 1, 2,and 3), do not cross the symmetric axis. However, ray 5 passes the sub-reflector without interception. This ray is considered as spillover. This analysis reveals, that by considering the rays reflecting from the other half of the

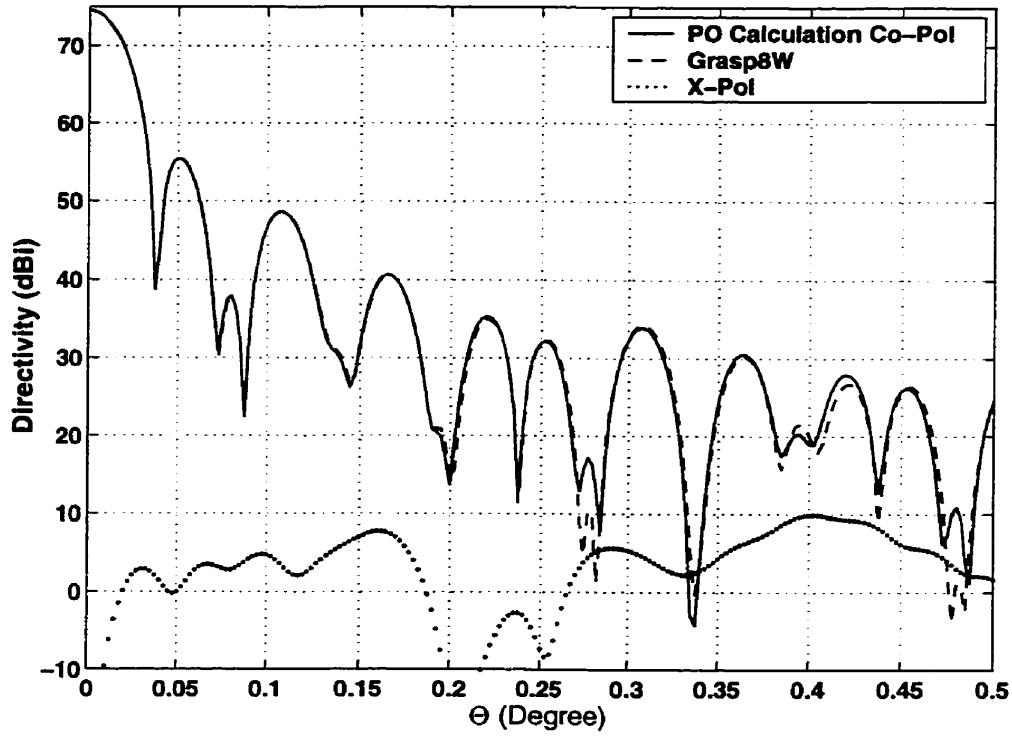

Figure 4.2: Radiation pattern of the LAR, D_F=25 m d_f=0.23 m, T_a= -15 dB, 2c=500 m, f=3GHz, D_S=5 m, e=1.0424

Feed-Reflector some part of the sub-reflector, which corresponds to $|\rho_S| < |\rho_{SA}|$ of Fig. 3.6, receives three rays at each point.

Rays reflected from the sub-reflector intercept the LAR, and the Feed-Reflector on the same side of reflection (Fig. 4.3). From aforementioned observation, and the system ray tracing of Fig. 4.3, it is perceived that the inner part of the LAR and the whole Feed-Reflector receive three rays at each point. However, the other part of the LAR collects only

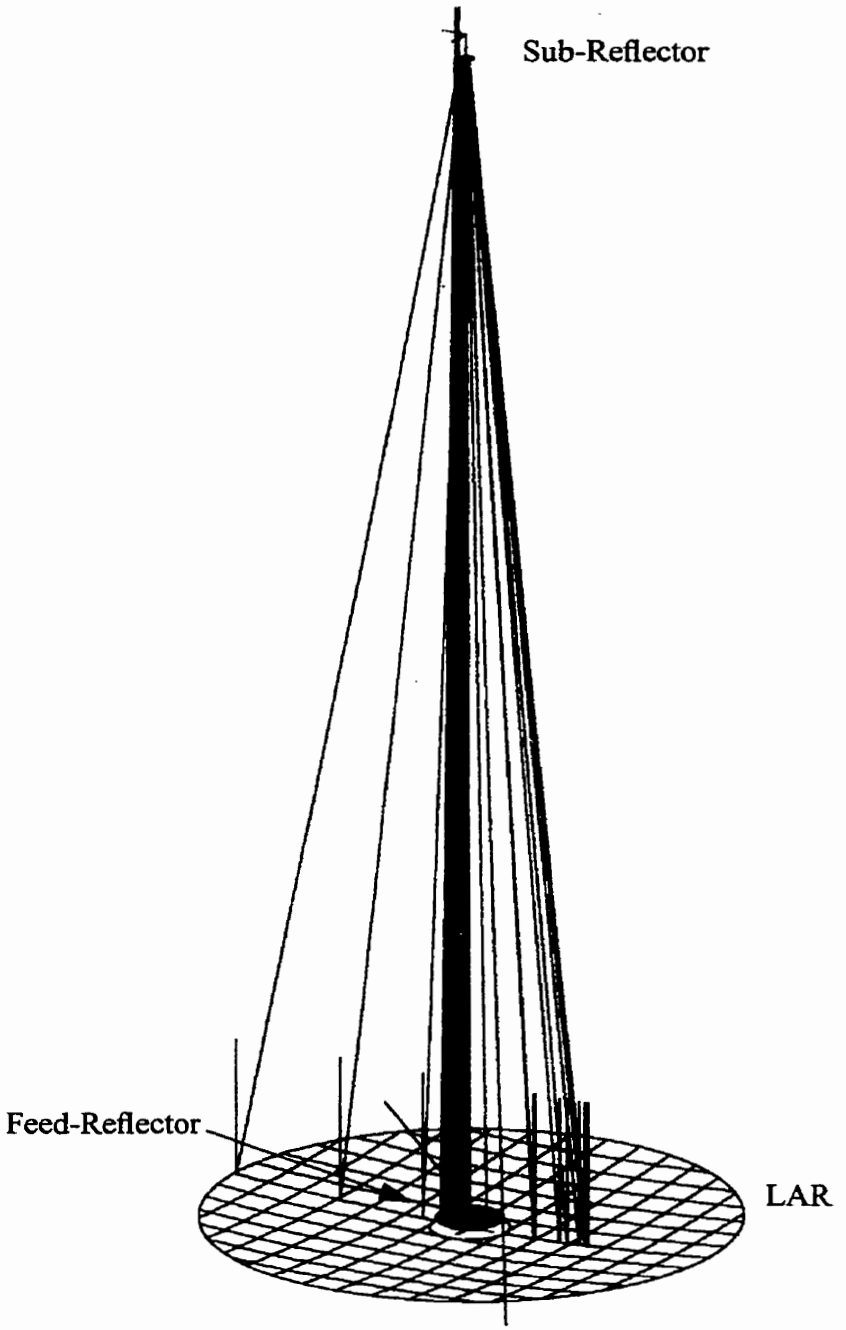

Figure 4.3: Ray tracing for the LAR system, D_F = 25 m, f_F=9 m d_f=0.23 m, 2c=500 m, D_S=5 m, e =1.0424, f=3 GHz

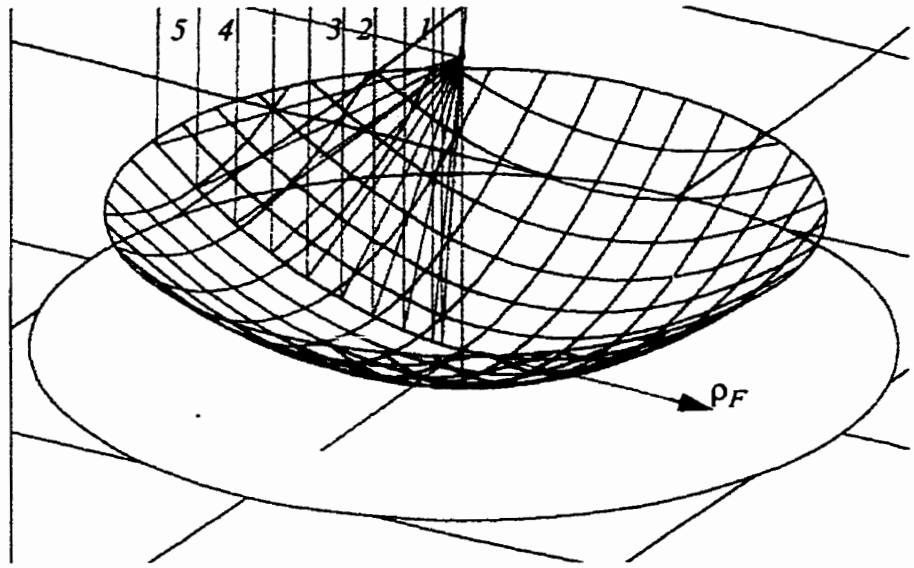

(a)

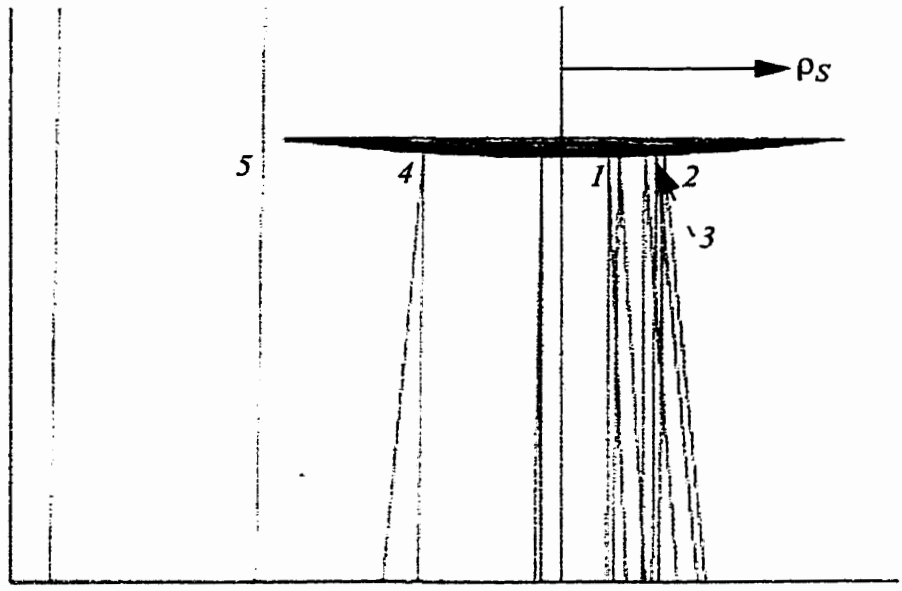

(b)

Figure 4.4: Ray tracing for a) Feed-Reflector b) Sub-reflector, D_F= 25 m, f_F=9 m d_f=0.23 m, 2c=500 m, D_S=5 m, e=1.0424, f=3GHz

one ray per point. Rays reflected from the LAR are almost parallel to the z-axis, which means the system focus to infinity. Unlike the LAR, those rays scattered from the Feed-Reflector go other directions than the zenith angle. These rays, which produce parasitic fields, contribute to the sidelobes locating several beamwidth away from the LAR main beam.

4.4. LAR System Aperture Distributions

Aperture amplitude and phase distributions for the Feed-Reflector with D_F=25 m, f_F=9 m, d_f=0.23, f=3 GHz, T_a=-15 dB at the Feed-Reflector edge are shown in Figs. 4.5a, and 4.5b. Aperture plane for the Feed-Reflector is located on the focal plane. PO techniques is employed to compute the aperture distribution. In Fig. 4.5a the Feed-Reflector computed aperture amplitude distribution shows -18 dB field taper at the aperture edge. In this figure, approximation of Eq.(3-9) is compared to the calculation which indicates a reasonable agreement. Fig. 4.5b shows the computed Feed-Reflector aperture phase distribution and is compared to that of Eq.(3-2) derived by using geometrical optics [7]. A good agreement is evident between them. Also the Fresnel quadratic phase error ($e^{-jk\frac{\rho'^2}{2R}}$) of Eq.(3-5) for R=489.824 (location of sub-reflector vertex) is plotted in the same figure.

The radiation pattern for the sub-reflector with D_S = 5 m, $2c$ = 500 m, e =1.0424, and f = 3 GHz, at the place of the LAR is depicted in Figs. 4.6a, and 4.6b. These figures show a field taper of -9.5 dB at the LAR edge, and a phase distribution with maximum 12° variation on the LAR. The dip in the middle of the sub-reflector radiation pattern reduces the effect of the sub-reflector on the Feed-Reflector and reduces its parasitic fields.

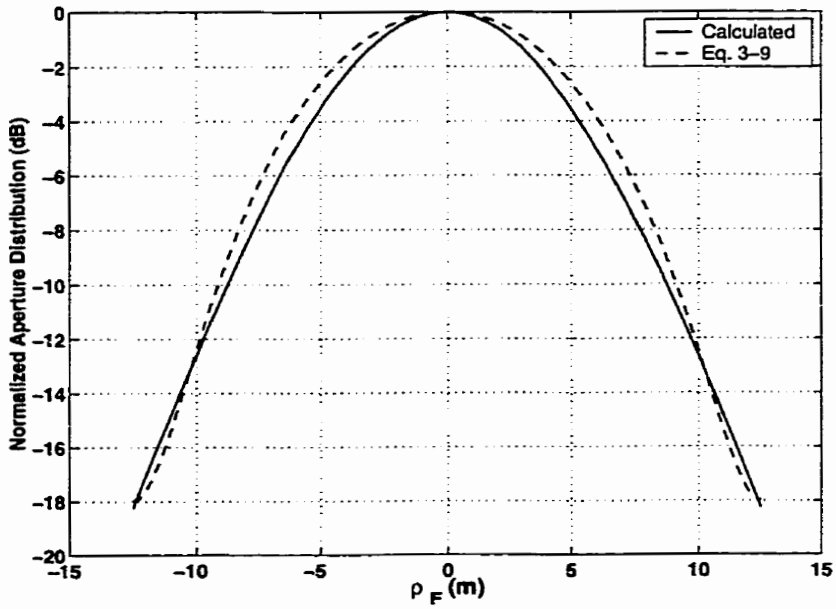

(a)

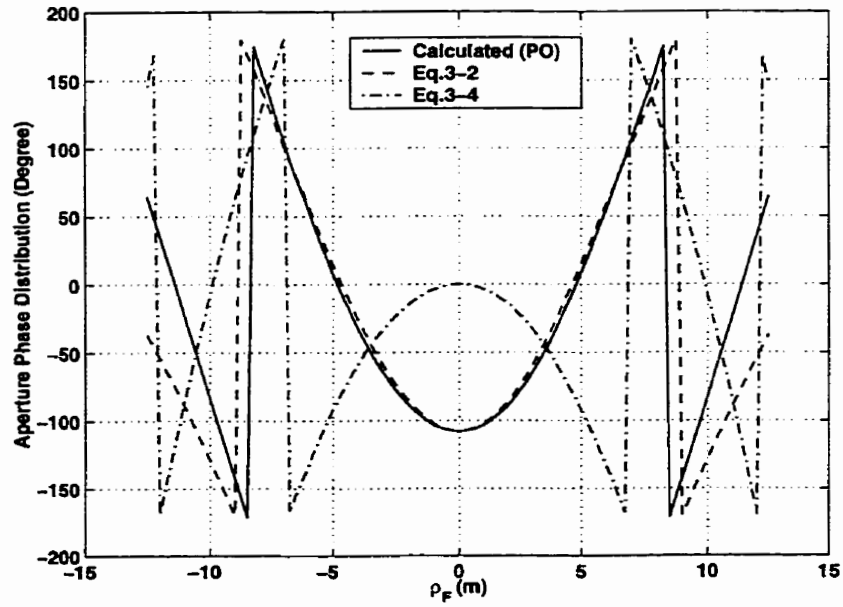

(b)

Figure 4.5: a) Feed-Reflector normalized aperture amplitude distribution, b) Feed-Reflector aperture phase distribution, D_F =25m, f=3 GHz, d_f =0.23 m, f_F = 9 m, T_a=15dB

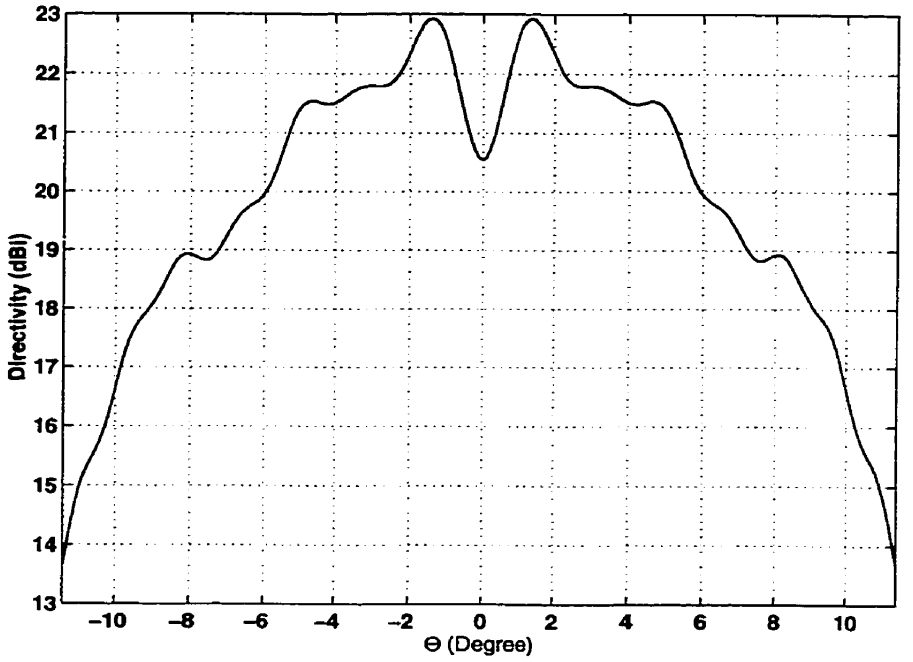

(a)

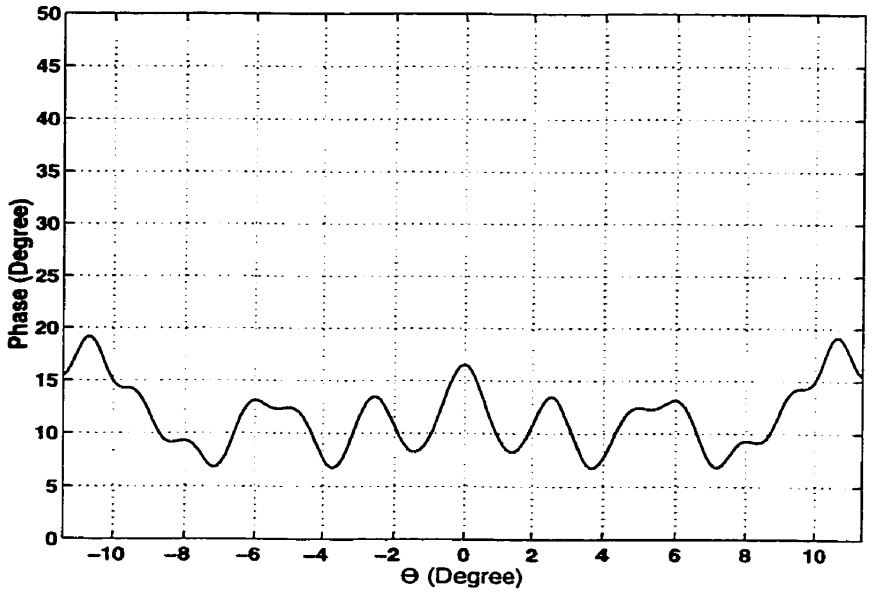

(b)

Figure 4.6: Radiation pattern of the sub-reflector at the LAR location a) Amplitude, b) Phase, D_S =5 m, e =1.0424, 2c=500, f =3 GHz

In Fig. 4.7a the gap in the middle of LAR aperture distribution is due to the Feed-Reflector blockage. The field taper at the LAR aperture edge is -15 dB which is equal to feed horn taper at the Feed-Reflector edge. The LAR Phase distribution (Fig. 4.7b) shows about 0.07λ phase error across the LAR aperture. This phase error is mostly due to estimation of sub-reflector surface.

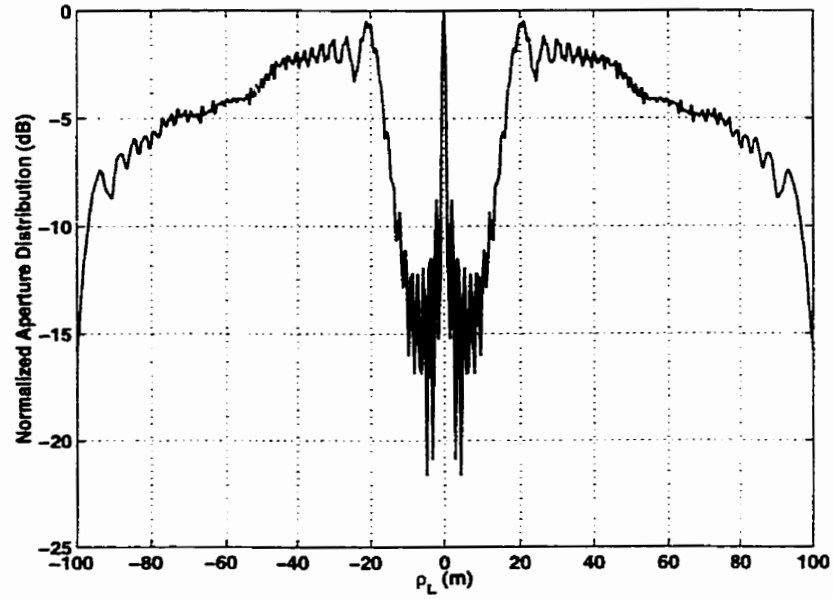

(a)

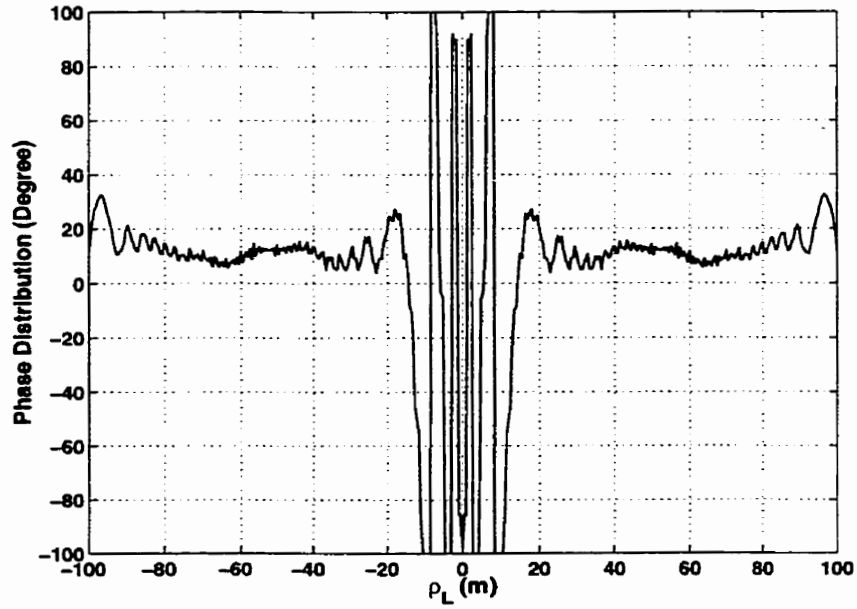

(b)

Figure 4.7: a) LAR normalized aperture distribution, b) LAR Phase distribution, D_S =5 m, e =1.0424, 2c=500, f =3 GHz

4.5. Effect of Defocusing Distance, d_f

Fig. 4.8 shows the radiation patterns of the Feed-Reflector with D_F = 25 m, f_F = 9 m, and T_a = -15 dB, at the sub-reflector (D_S = 5 m, $2c$ = 500 m, e =1.0424) location which is located in the Fresnel region of the Feed-Reflector. The results were for different values of feed defocusing d_f at 3 GHz. The maximum field intensity occurs when d_f=0.23 m. This value also provides the maximum efficiency for the LAR as shown in Fig. 4.9. Fig.4.10 shows the effect of feed defocusing on the LAR sidelobe level (SLL) and cross-polarization, which indicates that d_f=0.23 m provides minimum SLL and cross-polarization for LAR.

The field taper at the edge of the sub-reflector and LAR are presented in Fig. 4.11, as a function of defocusing distance d_f. At d_f=0.23 m both curves reach their minimum, indicating that, the minimum spillover is occurred. A ray tracing of the system for this value of defocusing as cited earlier, confirms that most of the rays emanating from the Feed-Reflector are intercepted by the sub-reflector, and most of the LAR surface is illuminated efficiently by the reflecting rays.

It has been shown in [8] that the defocusing value is independent of the operating frequency. This property was examined by the results of simulation at 5 GHz for the aforementioned Feed-Reflector and sub-reflector and T_a = -40 dB. Again maximum efficiency of 70% occurs at d_f=0.23 m.

The feed defocused distance which places the maximum energy density, at the sub-reflector location, i.e. R=489.648 m, was also calculated using Eq.(3-8). It was found to

be 0.25 m, in lieu of 0.23 m calculated above.

4.6. Effect of Field Taper at Feed-Reflector Edge, T_a

The size of the Feed-Reflector is determined by Eq.(3-13), and depends on the wavelength. In this design, the Feed-Reflector physical diameter is 25 m and by increasing the frequency, the effective aperture area in wavelength of the Feed-Reflector is kept constant by increasing the taper at the edge of the reflector, resulting in a nearly constant spot size on the sub-reflector. To investigate the effect of field taper at the edge of the Feed-Reflector, a system with parameters similar to those of the last section and d_f=0.23 m is considered.

Fig. 4.12 shows the normalized radiation pattern of the Feed-Reflector at the sub-reflector at 3 GHz. The field taper should be selected in a manner that the sub-reflector is placed in the main beam of the Feed-Reflector. Otherwise, a phase change over the sub-reflector will reduce the system efficiency. By investigation, it is found that the best field taper values are between -15 dB to -20 dB, at 3 GHz. By increasing the frequency to 5 GHz, the required field taper (T_a) becomes -40 dB. The reduction of field taper keeps the Feed-Reflector effective aperture area in wavelength constant, and compensates for the effect of beamwidth narrowing due to the frequency increase, and consequently places the sub-reflector in the Feed-Reflector main beam. According to Eq.(3-13), at this frequency the Feed-Reflector diameter is reduced to 14.63 m with T_a = -15 dB which is equivalent to -18 dB field taper at its aperture plane (Eq.(3-9)).

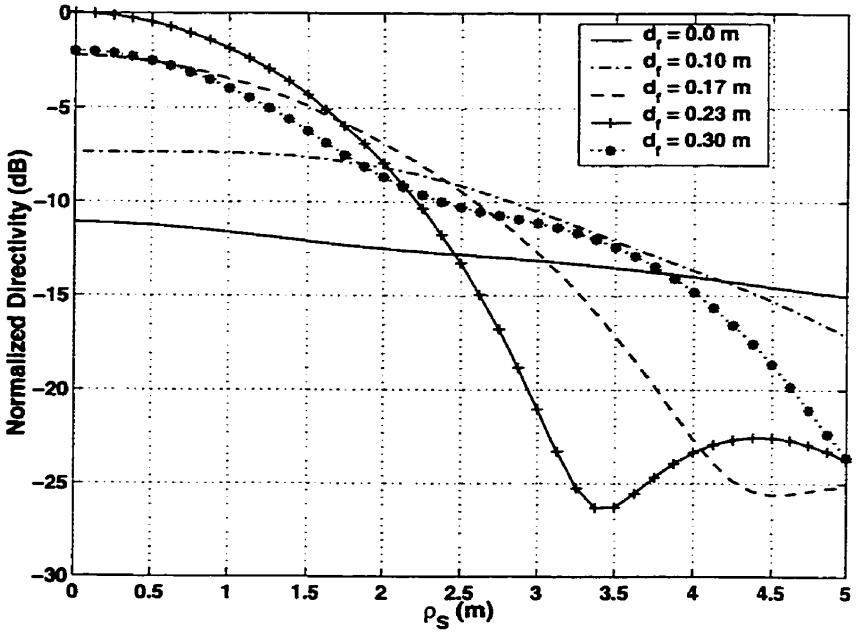

Figure 4.8: Normalized near field radiation pattern of the feed reflector antenna at the sub-reflector for different value of feed defocusing, d_f (D_F =25 m, T_a =-15 dB, f=3 GHz)

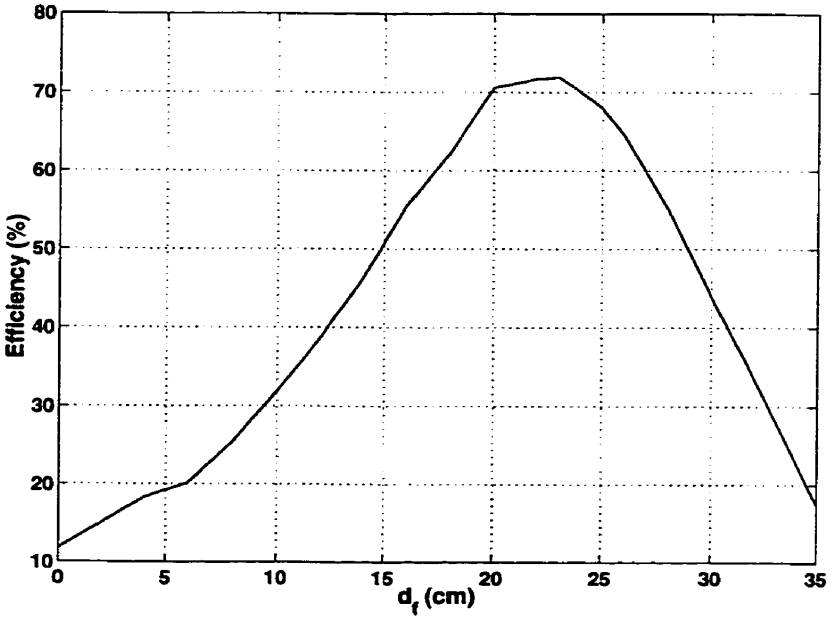

Figure 4.9: LAR efficiency versus feed horn location, T_a =-15 dB, D_F=25 m, D_S=5 m, 2c=500, e=1.0424, f=3GHz

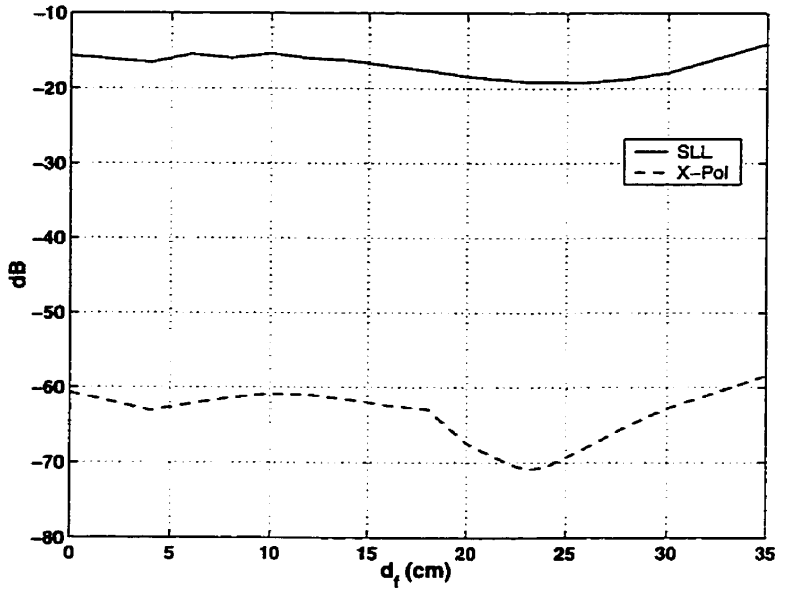

Figure 4.10: LAR sidelobe level and cross-polarization versus feed horn location d_f, T_a = -15 dB, D_F=25 m, D_S=5 m, 2c=500, e=1.0424, f = 3 GHz

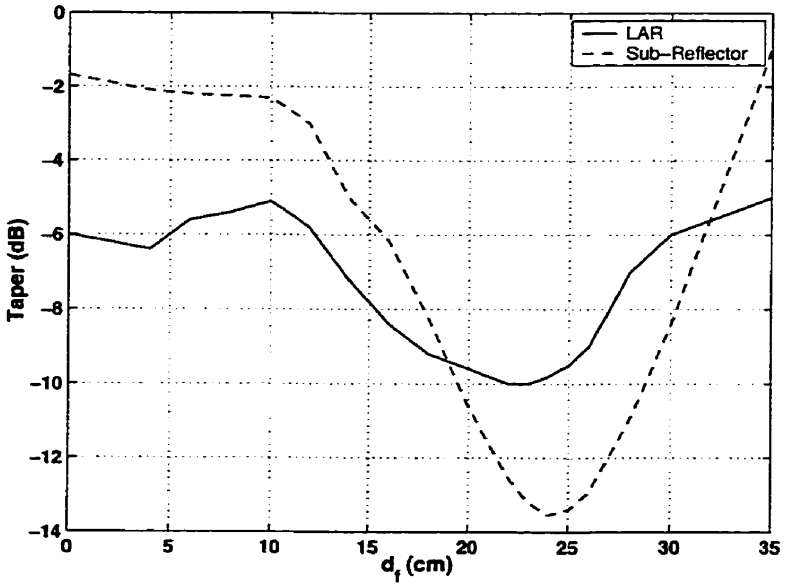

Figure 4.11: Taper at the edge of sub-reflector and LAR, T_a =-15 dB, D_F =25 m, D_S=5 m, 2c=500, e=1.0424, f= 3 GHz

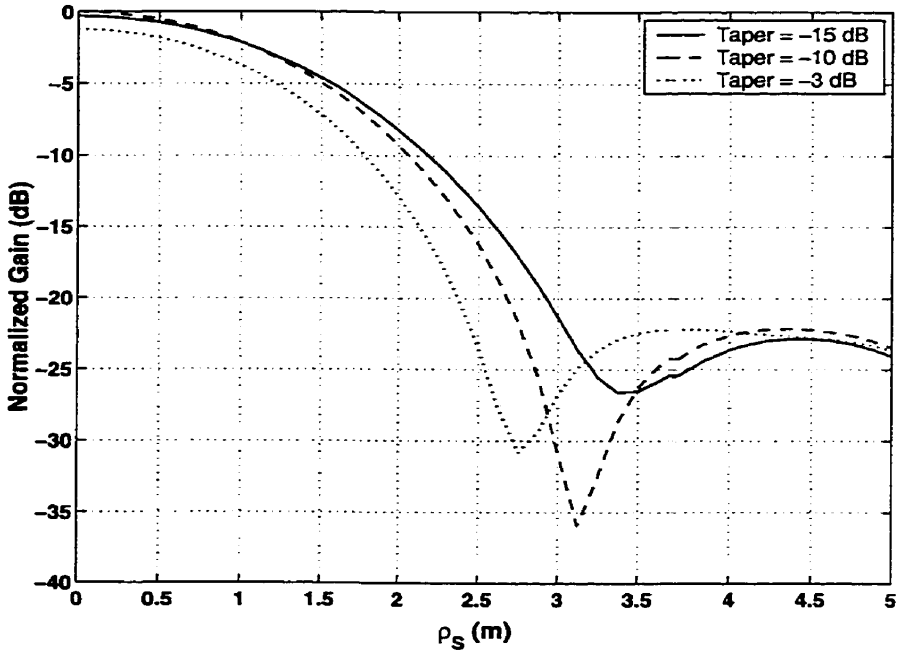

Figure 4.12: Normalized near field radiation pattern of the Feed-Reflector antenna at sub-reflector location for different values of feed horn taper, D_F =25 m, d_f=0.23 m, f =3 GHz

4.7. Sub-Reflector Eccentricity

The sub-reflector eccentricity, Eq.(4-4), determines the curvature of the sub-reflector, and as a result that portion of the LAR which must be illuminated. The results of different eccentricity values on the LAR gain are shown in Table 4.1. To obtain these results a 5 m diameter sub-reflector is considered. Parameters of the Feed-Reflector are D_F =25 m, and d_f=0.23 m, with a field taper of -15 dB at the Feed-Reflector edge, $2c$ = 500 m and the operating frequency was 3 GHz.

Table 4.1: Effect of the eccentricity of the sub-reflector on the LAR performance

e	φ_o(degree)	Efficiency%	SLL(dB)	X-Pol. (dB)	LAR TAPER (dB)
1.052	11.42	64.4	-20.85	-66.95	-19.5
1.050	12.0	67.45	-20.15	-68.5	-17.5
1.046	13.0	70.63	-19.45	-71.2	-12.5
1.044	13.5	71.6	-19.26	-71.81	-10
1.042	14.0	72.0	-19.04	-71.74	-9.5
1.040	14.5	71.78	-18.92	-71.02	-10.5
1.039	15.0	70.63	-18.85	-70.35	-12.5

4.8. Sub-Reflector Size, D_S

The sub-reflector size, according to Eq.(3-13), depends on the Feed-Reflector diameter, field taper at its edge, and the operating frequency. However, ray tracing shows that rays near the Feed-Reflector edge do not intercept the 5 m sub-reflector. This increases the spillover loss of the system and reduces the aperture efficiency. This can also be observed by referring to Figs. 3.4 and 4.8, where the 5 m sub-reflector does not intercept large amounts of energy in the Feed-Reflector main beam. Attempts to increase the field taper at the Feed-Reflector edge, which would make the beam narrower and locate more of its energy on the sub-reflector, will increase the Feed-Reflector spillover.

To minimize the effect of spillover, the sub-reflector diameter was increased to 10 m. The increase in the sub-reflector size places its edge over the Feed-Reflector radiation pattern sidelobes. To increase the radiation pattern average spot size X' in Fig. 3.4, it is

necessary to decrease Feed-Reflector diameter to 12.2 m, at 3 GHz (with 15 dB edge taper) according to Eq.(3-13). However, the Feed-Reflector physical diameter is fixed (25 m). So the only way to decrease the illumination area is to select a higher directivity horn antenna to illuminate a smaller part of the Feed-Reflector. A horn which can illuminate a smaller part of the Feed-Reflector with D_F=12.0 m (the horn produces -15 dB field taper at this part edge) and generate adequate radiation pattern spot size to cover the sub-reflector, was found by trial and error. The difference between this value and that of Eq.(3-13) is due to the fact that the actual diameter of the Feed-Reflector is more than 12.2 m, which contributes to the radiation pattern.

The effect of increasing the sub-reflector size for different eccentricities are also calculated. For e = 1.096, or ϕ_0=13.0°, the LAR efficiency reaches to 74.8%. The corresponding radiation patterns are shown in Fig. 4.13. This increase in efficiency is due to the reduction of spillover from the sub-reflector and the Feed-Reflector.

4.9. LAR Performance Over Its Operating Band

The LAR's primary purpose is to operate over a frequency band from 1 to 22 GHz. The idea of designing the Feed-Reflector to cover this frequency band is to maintain the effective aperture area in wavelength constant which results in a fixed spot size. This can be done by utilization of different horns with various directivities. To investigate the performance of the LAR over its bandwidth, a Feed-Reflector with a fixed diameter of 25 m and 9 m focal length is assumed. Two sub-reflectors with 5 m (e=1.0424) and 10 m (e=1.096) diameters and $2c$ =500 m are considered.

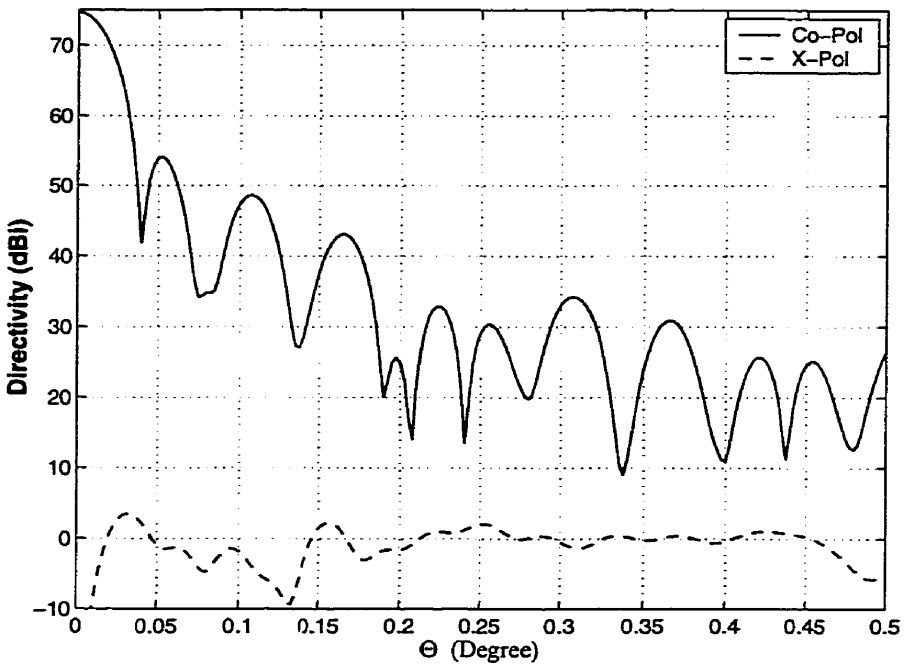

Figure 4.13: Radiation pattern of LAR, d_f=0.23 m, 2c=500 m, D_F = 12 m, f=3GHz, D_S=10 m, e=1.096

The LAR efficiency with the Feed-Reflector antenna is calculated over its operating band, and is shown in Fig. 4.14. For deriving this graph, the feed horn was assumed to be 0.23 m away from focal point with a Gaussian radiation pattern. For each frequency, the central part of the Feed-Reflector with diameter D_F, (shown in Fig. 4.15) is considered to be illuminated by a Gaussian beam, which produces -15 dB taper at its boundary. Also in this figure, the values obtained by Eq.(3-13) are plotted. The difference between these two plots can be interpreted as in latter, it is assumed that the diameter of the Feed-Reflector aperture is limited to the value obtained. However, the former values show that central part of the Feed-Reflector which has -15 dB taper at its selected boundary.

Due to the Feed-Reflector size limitation, which prevents utilization of constant effective aperture area, the efficiency drops for the frequencies below 3 GHz and reaches to about 18% for a 5 m sub-reflector at 1 GHz. However, this reduction in efficiency is less for the 10 m sub-reflector. If the minimum 50% efficiency is set as a criteria, the system with 5 m sub-reflector can operate well above 2 GHz and this value reduces to 1 GHz for the 10 m sub-reflector. For the frequencies between 3-22 GHz, small variations in the efficiency are observed, but the overall efficiencies are almost uniform.

By decreasing the Feed-Reflector size, it is expected that the defocusing distance according to Eq.(3-8) will change. However, results of simulation show, for example at 22 GHz, the directivity remains almost constant for $0.18 < d_f < 0.25$ m. The radiation patterns of LAR at 22 GHz for different value of defocusing distances are shown in Fig. 4.16.

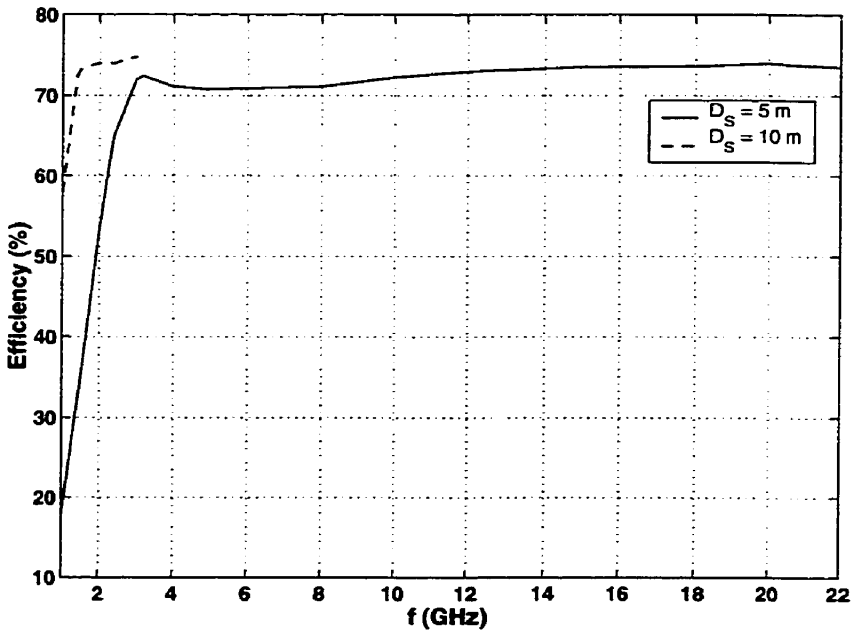

Figure 4.14: Symmetric LAR efficiency versus frequency

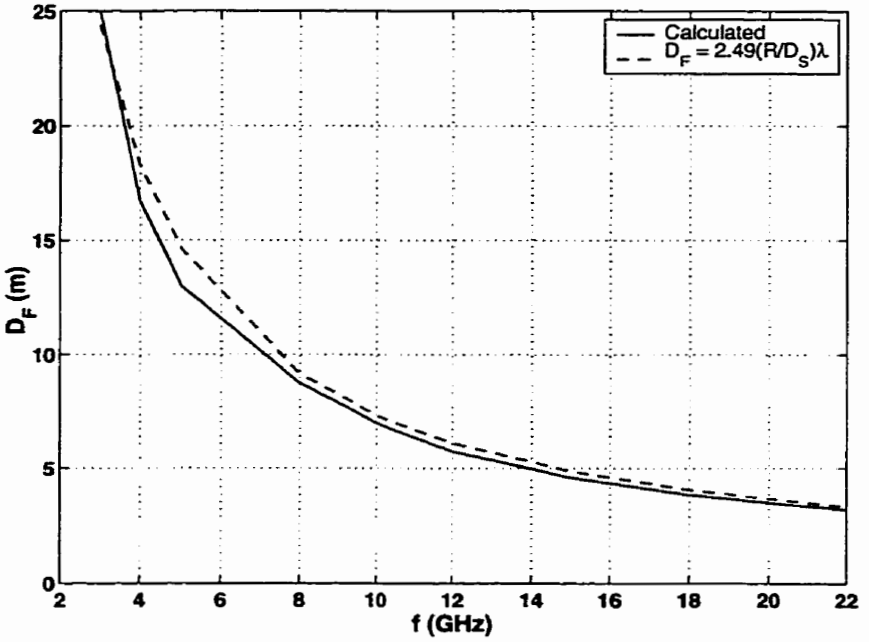

Figure 4.15: Different portion of the Feed-Reflector that must be illuminated with -15 dB field taper at the edge

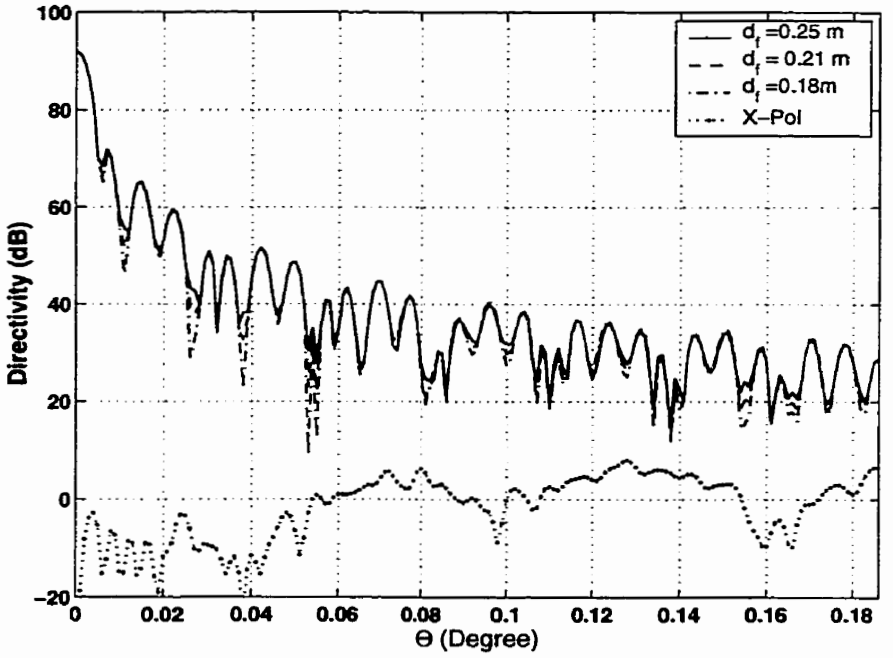

Figure 4.16: Radiation patterns of LAR at 22 GHz for different value of defocusing

4.10. Performance of the Shaped LAR

In order to obtain higher directivities from the LAR, it is necessary to shape its surface and those of its Cassegrain feed system. In this section, first a shaping procedure which is based on a diffraction synthesis is explained and then applied to the LAR system. Three sets of shaping techniques have been carried out i) Shaping the LAR and the subreflector, ii) Shaping the LAR and the Feed-Reflector and iii) Shaping all three surfaces together.

4.10.1. Global Surface Expansion Using Orthogonal Functions

The first step in the diffraction synthesis of the LAR is to parameterize the antenna system. An orthogonal global expansion of the Fourier-Jacobi type that is related to the Zernike functions was used to represent shaped reflector surfaces by Rahmat-Samii [59 ,91]:

$$z'(t,\psi) = \sum_{0}^{N}\sum_{0}^{M}(C_{nm}\cos n\psi + D_{nm}\sin n\psi)F_m^{\,n}(t) \tag{4-5}$$

where C_{nm}, and D_{nm} are the expansion coefficients, t, ψ are planar aperture parameters to show the coordinates of a point $\bar{r}'_{sur}=(x',y',z')$ on the reflector as

$$x' = x'(t,\psi), y' = y'(t,\psi), z' = z'(t,\psi) \tag{4-6}$$

$$0 \le t \le 1, 0 \le \psi \le 2\pi \tag{4-7}$$

$F_m^n(t)$ is the modified Jacobi polynomial defined in Appendix I. In this work the expansion is applied to each reflector of the LAR Cassegrainian system in terms of the

corresponding local coordinate system as shown in Fig. 4.1.

The expansion of Eq.(4-5) is global in the sense that each basis function acts in the entire domain of Eq.(4-7), in contrast to a localized function which has usually nonzero values only with subgridded patch. The Eq.(4-5) guarantees that the reflector surface is continuous, and so are the derivatives of all orders.

For a given reflector surface $z'(t,\psi)$, the expansion coefficient can be determined by

$$\begin{pmatrix} C_{nm} \\ D_{nm} \end{pmatrix} = \frac{\varepsilon_n}{2\pi}\int_0^{2\pi}\int_0^1 z'(t,\psi)\begin{pmatrix} \cos n\psi \\ \sin n\psi \end{pmatrix} F_m^{\,n}(t)\,t\,d\psi\,dt \tag{4-8}$$

$$\varepsilon_n = \begin{cases} 1 & n = 0 \\ 2 & n \neq 0 \end{cases} \tag{4-9}$$

For the LAR system surfaces, due to their symmetric property for the scan angle of 0°, it suffices to use C_{0m} coefficients alone in Eq.(4-5) to represent the shaped reflectors. In this case the number of the expansion coefficients is reduced from a two-dimensional to one-dimensional set. The coefficients for the LAR, the sub-reflector with $2c$ = 500 m, e= 1.0424,and 5 m diameter, and the Feed-reflector with a focal length of 9 m and diameter of 25 m is summarised in Table 4.2.

Table 4.2: Jacobi Fourier Coefficients of the LAR System, D_F = 25 m, f_F= 9m, D_S= 5 m, $2c$=500 m, e =1.0424

Coefficient	LAR	Sub-Reflector	Feed-Reflector
C_{00}	-351.7856	-346.411	-4.8294
C_{01}	-1.0206	0.0307	-0.886

The goal is to maximize the directivity of the system. In this approach, the best solution is determined by an optimization technique, and the criterion is the minimization of an object (penalty, cost) function (Cost = -Directivity). The initial values of the optimization are the original LAR, sub-reflector, and Feed-Reflector surfaces. In this study, genetic algorithm is used as the optimization utility [94].

4.10.2. Shaping LAR and Sub-Reflector

The first shaping process is done on the LAR and its sub-reflector surfaces at 3 GHz. For each surface six coefficients are considered. The Feed-Reflector remains unchanged, with a 0.23 m defocusing of the feed horn. The coefficients after shaping are presented in Table 4.3.

The peak gain of 74.80 dBi, which is equivalent to the efficiency of 76.5% is obtained. Radiation patterns of LAR and sub-reflector are shown in Figs.4.17 and 4.18, and compare with that obtained by Grasp8W.

Table 4.3: Shaped LAR and Sub-Reflector Coefficients, $D_F = 25$ m, $f_F = 9$m

Coefficient	LAR	Sub-reflector
C_{00}	-351.7856	-346.293
C_{01}	-1.0229	0.0307
C_{02}	0	0.0023
C_{03}	0	0
C_{04}	0	0
C_{06}	0	0

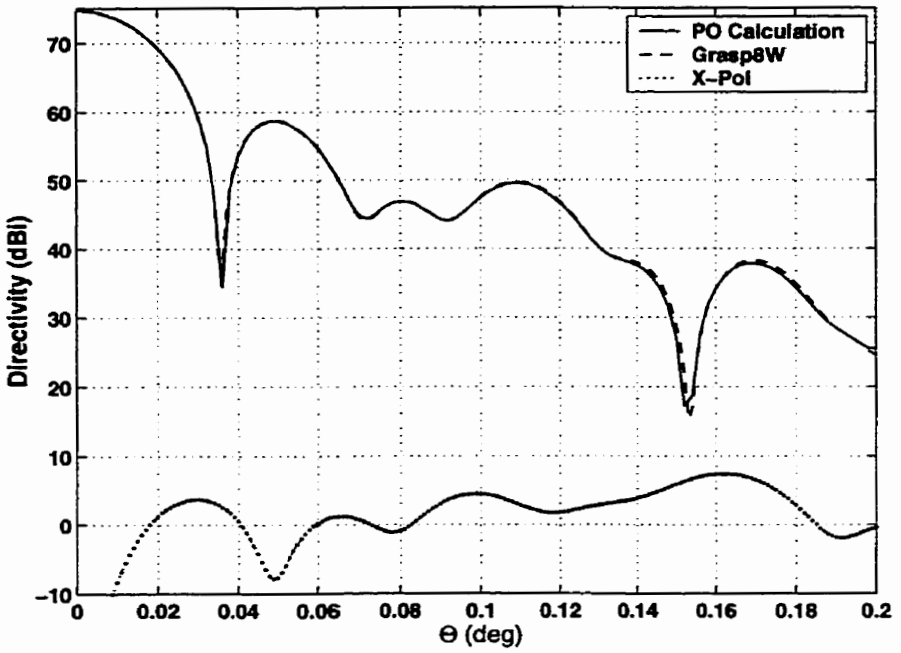

Figure 4.17: LAR radiation patterns for the shaped LAR and sub-reflector at 3 GHz

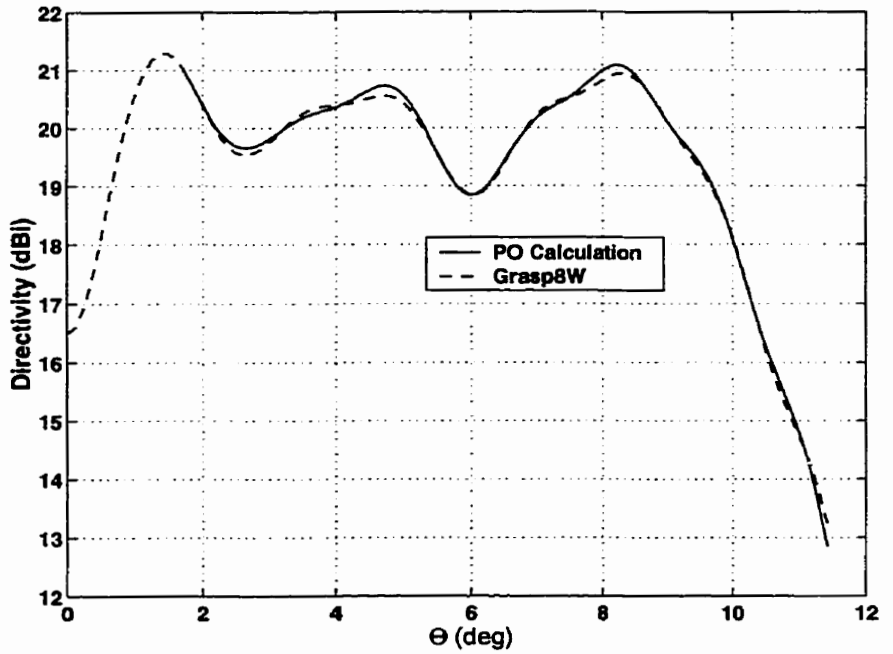

Figure 4.18: Sub-reflector radiation patterns for the shaped LAR and sub-reflector at 3GHz

4.10.3. Shaping LAR and Feed-Reflector

Another shaping process is to shape the LAR and the Feed-Reflector antenna. Again, the operating frequency is 3 GHz. This process is mostly used to reduce the spillover on the sub-reflector and to make the LAR aperture distribution uniform. Six coefficients are utilized for each surface. The sub-reflector parameters are $2c$ = 500 m, e= 1.0424, and 5 m diameter. In this optimization process, defocusing distance d_f and the Feed-reflector edge taper are also considered as parameters to be optimized. The peak gain reaches to 74.71dBi, which is equivalent to an efficiency of 75%. The coefficient of Jacobi-Fourier series after shaping are depicted in Table 4.4, and the radiation patterns of the LAR are shown in Fig. 4.19 and is compared to that of Grasp8W. Defocusing distance d_f, and Feed-Reflector edge taper T_a, after shape are 0.2433 m,and -15 dB respectively.

Table 4.4: Shaped LAR and Feed-Reflector Coefficients, D_S= 5 m, $2c$=500 m, e =1.0424

Coefficients	LAR	Feed-Reflector
C_{00}	-351.7856	-4.8294
C_{01}	-1.0205	0.886
C_{02}	0	0.0012
C_{03}	0	0
C_{04}	0	0.0004
C_{05}	0.0001	0

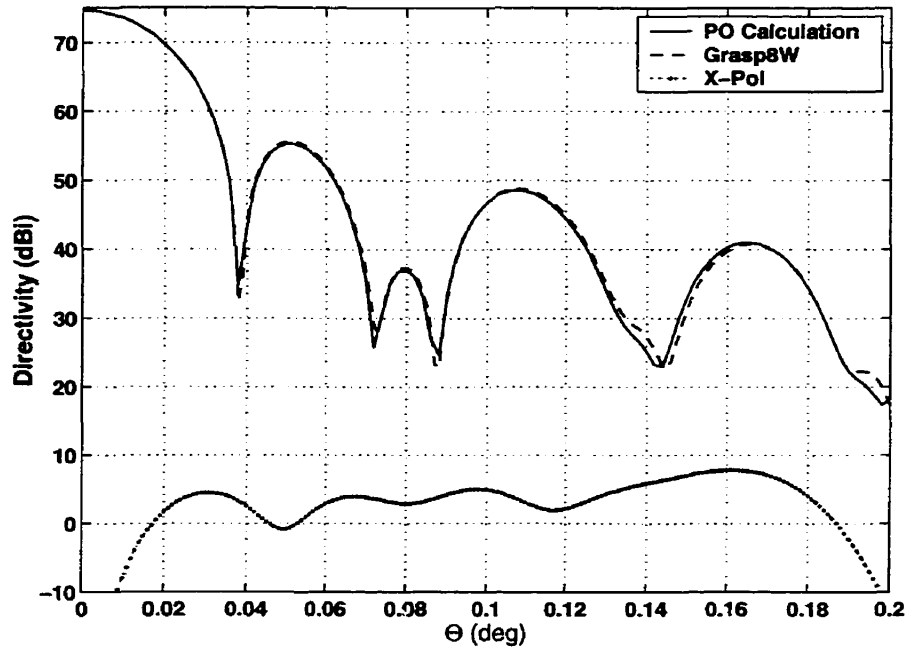

Figure 4.19: LAR radiation pattern for the shaped LAR and Feed-Reflector, D_S= 5 m, 2c=500 m, e =1.0424, f = 3 GHz.

4.10.4. Shaping LAR, Sub-Reflector, and Feed-Reflector

The last shaping process is to shape all three reflectors together. The operating frequency is 3 GHz. Again, six coefficients are utilized for each surface. In this optimization process, defocusing distance d_f, and the Feed-Reflector edge taper are also considered as parameters to be optimized.The peak gain reaches to 74.91 dBi, which is equivalent to the efficiency of 78.5%. The coefficients of Jacobi-Fourier series after shaping are depicted in Table 4.5, and the radiation patterns of the LAR and sub-reflector are shown in Figs 4.20. and 4.21, which are compared to those of Grasp8W. d_f, and the Feed-Reflector edge taper after optimization are 0.2371 m, and -16.81 dB, respectively.

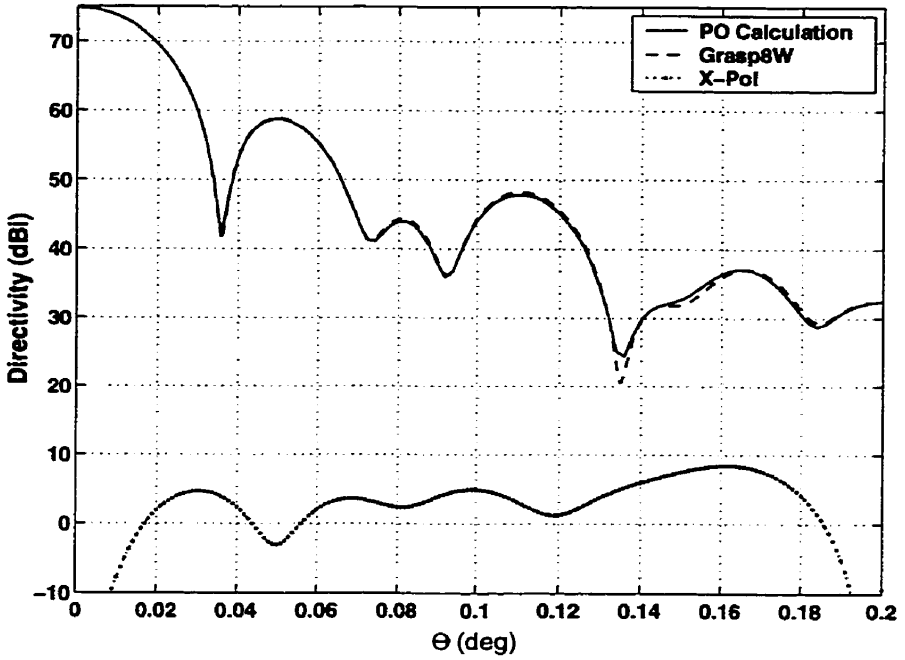

Figure 4.20: LAR radiation patterns for shaped LAR, sub-reflector and Feed-Reflector at 3 GHz

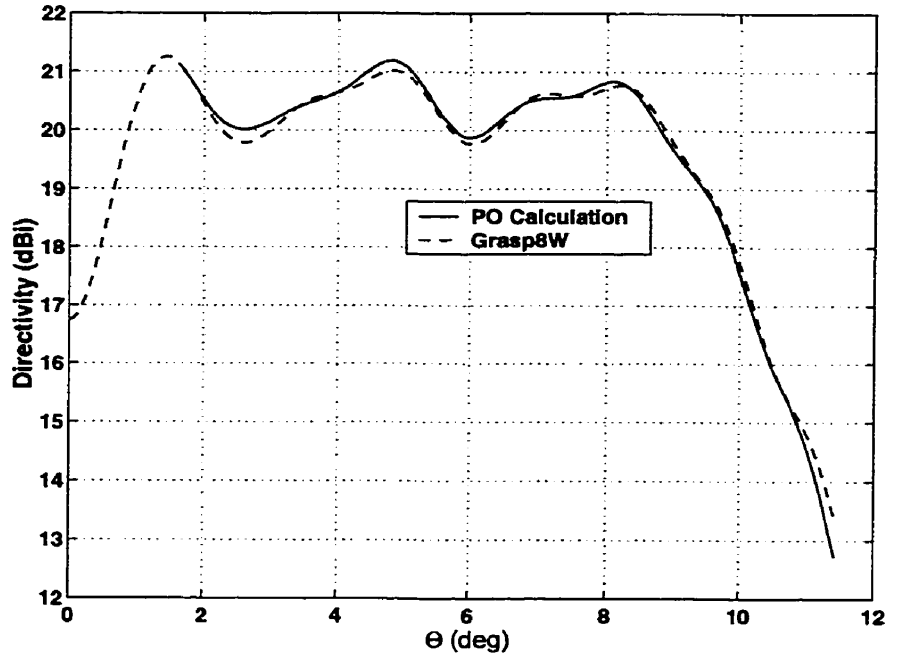

Figure 4.21: Sub-reflector radiation pattern for shaped LAR, sub-reflector and Feed-Reflector at 3 GHz

Table 4.5: Shaped LAR, Sub-Reflector, and Feed-Reflector Coefficients

Coefficients	LAR	Sub-reflector	Feed-Reflector
C_{00}	-351.9135	-346.4515	-4.8294
C_{01}	-1.0211	0.0307	-0.886
C_{02}	0	0.0016	0.0009
C_{03}	0	0.0003	0.0004
C_{04}	0.0005	0.0001	0
C_{05}	0	0	0

Results of these three sets of shaping techniques are summarized in Table 4.6

Table 4.6: Summary of shaping techniques

Shaping Technique	Efficiency(%)	SLL(dB)	X-Pol(dB)
LAR & Sub-Reflector	76.5	-16.17	-71.12
LAR & Feed-Reflector	75	-19.42	-70.17
LAR & Feed-Reflector & Sub-reflector	78.5	-16.10	-70.25

4.11. Conclusion

The performances and characteristics of the LAR using the Feed-Reflector were investigated. To make it feasible for fabrication, a conventional hyperboloid sub-reflector was considered, which approximated the surface obtained by the equal path law. The effect of sub-reflector second focal point position, eccentricity, and size were investigated. ray tracing was used for better understanding of the system performance. For the unshaped surfaces a maximum efficiency of 75% was obtained with less than -65 dB cross polarization. The SLL is in the acceptable range [95].

The performance of the LAR was investigated over its operating band. It was found that for a 5 meter sub-reflector and a 25 m Feed-Reflector, the LAR efficiency is more than 72% for frequencies above 3.0 GHz. However, if the sub-reflector diameter is increased to 10 m this frequency reduces to 1 GHz.

Three shaping processes were conducted on the LAR system based on a diffraction synthesis technique, using Jacobi-Fourier series to represent the reflector surface. An efficiency of 78.5% was obtained by shaping all three reflectors. The final radiation patterns of each case were compared to those of Grasp8w, and showed an excellent agreement [96].

Chapter 5

GAUSSIAN BEAM ANALYSIS OF LARGE ADAPTIVE REFLECTOR ANTENNA USING FEED-REFLECTOR

5.1. Introduction

The recent trend in microwave instruments is the use of multiple millimetre and sub-millimetre wavelength bands. These systems are typically analysed by using physical optics, Gaussian beams or ray tracing techniques. Physical optics offers high accuracy at the expense of computational time. This trade-off becomes particularly apparent in the analysis of multiple reflector antennas, such as beam waveguide antennas, where physical optics is used to compute the current on each reflector from the current on the previous reflector. One example of the beam waveguide antennas is the Cassegrainian LAR fed by the Feed-Reflector. At the other end of the spectrum are ray tracing approaches that ignore diffraction effects entirely. These methods are fast but fail to predict some effects accurately.

An intermediate approach is to use an appropriate set of expansion functions to model the field between the reflectors. If the set is chosen wisely, only a few coefficients need to be determined from each reflector current. The field is then computed at the next reflector through the use of the expansion functions and their coefficients rather than by using the previous reflector current. For a waveguide system with no enclosing tubes an excellent set of expansion functions is Gaussian-Laguerre beam modes set. In many cases

a preliminary design which includes the effects on diffraction may be obtained by considering only the fundamental mode and a thin lens model for the reflectors. Higher order modes are included to model the effects of the curved reflector, which include asymmetric distortion of the beam, cross polarization and beam truncation.

In Section 5.2. after a brief review of orthogonal Gaussian-Laguerre expansion the equivalent Gaussian beam modes for the Feed-Reflector are calculated. Then in section 5.3. the sub-reflector parameters are obtained by utilizing the Gaussian mode analysis of the system.

5.2. Gaussian Beam Analysis of the Feed-Reflector

For the LAR using the Feed-Reflector system as a beam waveguide, an excellent approach for the analysis is the Gaussian beam method. This method not only facilitates the performance investigation of the system, but also provides a powerful tool to calculate the sub-reflector parameters for maximum LAR efficiency. Thus, before proceeding to the analysis of Feed-Reflector, it is advantageous to review the techniques of Gaussian beam-mode optics.

The Gauss-Laguerre beam modes are approximate solutions to the wave equation in cylindrical coordinates, which are valid when the wave propagates in nearly parallel beams [67]. The beam-mode superposition representing the transverse electric field E of an axially-symmetric beam, in cylindrical polar co-ordinates (ρ,z), with the z-axis being coincident with the beam axis, is

$$E(\rho, z) = \sum_{p=0}^{\infty} A_p \sqrt{\frac{2}{\pi W^2}} L_p^0\left[\frac{2\rho^2}{W^2}\right] \exp\left(\frac{-\rho^2}{W^2}\right) \exp\left(-jk_o z - j\frac{k_o \rho^2}{2R} + j\theta_p\right) \qquad (5\text{-}1)$$

where k_o is the wave number, and $p = 0, 1, 2, 3,...$ is the mode number. L_p^o is a zero-order Laguerre polynomial of argument $(2\rho^2/W^2)$ [97].

The first exponential term in Eq.(5-1) indicates the form of the variation of the modulus of p^{th} beam-mode over a cross-sectional plane. This is a Gaussian function of ρ^2 modulated by the L_p^o. The scale of this variation changes with z through the z-dependence of the beamwidth parameter W, beam radius defined when intensity reduces to e^{-1} [67] of the fundamental mode. Gauss-Laguerre functions form an orthogonal set, such that [71]

$$\frac{4}{W^2}\int_0^{\infty} L_m^0\left[\frac{2\rho^2}{W^2}\right] L_n^0\left[\frac{2\rho^2}{W^2}\right] \exp\left(\frac{-2\rho^2}{W^2}\right) \rho d\rho = \delta_{mn} \qquad (5\text{-}2)$$

A_p is the amplitude of the p^{th} mode and is independent of ρ and z. Its values are to be determined by fitting the above superposition to actual field over some transverse plane for which the form of the field is known. For the Feed-Reflector, this will be its aperture plane. The mode coefficients are in general complex and can be determined at z_a as

$$A_p = \frac{4}{W^2}\int_0^{\infty} |E(\rho, z_a)| L_p^0\left[\frac{2\rho^2}{W^2}\right] \exp\left(\frac{-\rho^2}{W^2}\right) \rho d\rho \qquad (5\text{-}3)$$

The phase term in Eq.(5-1) has three components. The first term is a linear propagation phase. The second term in the exponential shows the variation of the phase of the beam mode field over a cross-sectional plane, relative to its value on axis. The form of this term (quadratic) indicates a spherical wave-front with radius of curvature, R. The values of

R varies with the propagation distance, z, as shown in Eq.(5-4) below. The fact that R is not linearly dependent on z means that the location of the centre of the curvature of the beam modes, equi-phase surfaces varies with beam distance. The last component of the phase term is mode dependent. It represents a mode-dependent phase shift, or phase slippage.

The beam parameters, the mode independent beam radius W, the mode independent radius of curvature of the wavefront R, and the phase slippage per beam mode θ_p, vary with z according to[71]

$$\begin{aligned} W^2 &= W_o^2 + \{2(z-z_o)/(k_o W_o)\}^2 \\ R &= (z-z_o) + \left\{(k_o W_o^2/2)^2/(z-z_o)\right\} \\ \theta_p &= (2p+1)tan^{-1}\{2(z-z_o)/k_o W_o^2\} \end{aligned} \tag{5-4}$$

where in general W_o and z_o, beam waist and its position, are constants which can be expressed in terms of the values W_a and R_a assigned to W and R at the aperture plane located at $z = z_a$ thus

$$\begin{aligned} W_o^2 &= W_a^2/\left\{1 + (k_o W_a^2/2R_a)^2\right\} \\ z_o - z_a &= -R_a/\left\{1 + (2R_a/k_o W_a^2)^2\right\} \end{aligned} \tag{5-5}$$

The values of W_a and R_a are not uniquely determined. That is to say, an arbitrary axially symmetric function can be fitted by a superposition of Gauss-Laguerre functions with any choice of values for the parameters W and R. The best choice is that to maximize the power in the fundamental mode[71].

In Gaussian-beam optics the relationship between the beam parameters of the incident and reflected fields are necessary for solving a reflection problem. In reflector antennas the reflecting surface is conical. Fig. 5.1 shows a representative example of conical section with focii at F_1 and F_2. The transformation of a paraxial beam-mode parameters, W and R (emitted from F_1) that occur as the beam is reflected from the conical section can be shown to be related by[98]

$$\begin{aligned} W_r &= W_i \\ 1/R_r &= 1/R_i - 1/f \end{aligned} \tag{5-6}$$

where W_i and R_i, are beam radius and radius of curvature of the incident and W_r and R_r are those for the reflected wavefront at the reflection point N. The sign of R_i or R_r is negative when F_1 or F_2 lies in the direction of wave propagation shown by the arrow in Fig. 5.1. f is the "focal length" of the conical section and from Fig. 5.1 it can be defined as

$$1/R_2 = 1/R_1 - 1/f \tag{5-7}$$

In this equation, R_1 and R_2 are distances between F_1 and N, and F_2 and N, respectively. R_1 or R_2 is positive when they lie on opposite side of the reflection surface, and negative when they are on the same side. In this thesis, the subscript S relates parameters W_i, W_r, R_i, R_r, R_1, R_2, f, F_1, F_2 to the sub-reflector, and L associates them with the LAR.

To apply the Gaussian beam method to the system, the feed horn of the Feed-Reflector is represented by the first term of Gaussian-Laguerre modes [71]. The feed horn is displaced 0.23 m away from the focal point of the paraboloid Feed-Reflector with

Conical Section of a Quadratic Surface of Revolution

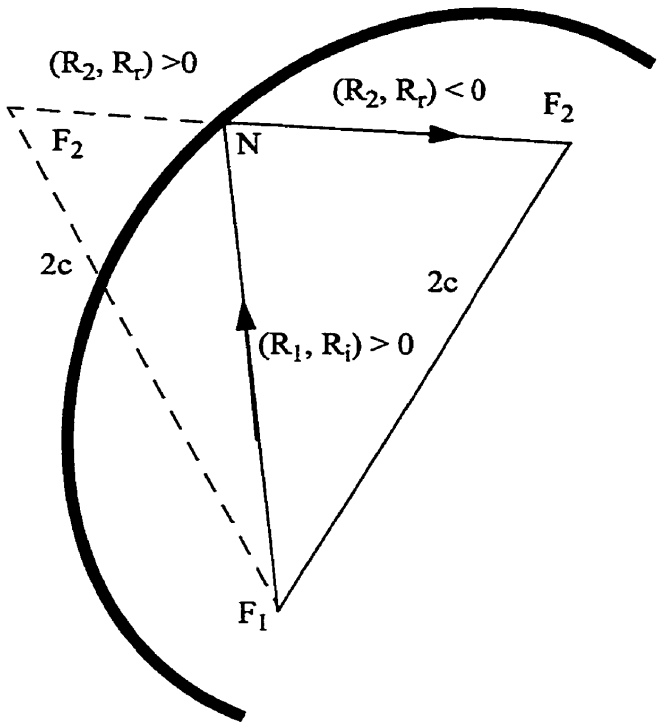

Figure 5.1: Cross-section of a conical reflector with the direction of wave propagation

$D_F = 25$ m ($a = 12.5$ m) and a focal length of $f_F = 9$ m, which provides -15 dB field taper at the edge of the Feed-Reflector at 3 GHz. Due to the Feed-Reflector curvature and also low aperture edge field taper, exercising Eqs.(5-6) and (5-7) to find reflected beam parameters at its aperture i.e the beam radius $W_a = W_f$, and the radius of curvature $R_a = R_f$, may cause an inaccurate result. However, the Feed-Reflector aperture distribution $E_f(\rho, z_f)$, can be calculated accurately by employing the physical optics (PO). Then, the field at the aperture is decomposed into a sum of orthogonal Gaussian-Laguerre beam modes[71]. All these constituent beam modes have identical equi-phase radii of curvature. However, as the beam from the Feed-Reflector aperture propagates, the relative phases of the modes shift as discussed above. The Feed-Reflector aperture is considered to be at its edge, i.e. $z_a = z_f = 4.341$ m, as shown in Fig. 5.2.

The logical choice for W_f/a is that which maximizes the fractional power in the fundamental beam mode i.e. $p = 0$. The fractional power in the first mode is given by[71]

$$\eta\left[\frac{W_f}{a}\right] = \frac{4}{W_f^2}\frac{\left[\int_0^a \left|E_f(\rho, z_f)\right| \exp(-\rho^2/W_f^2)\rho d\rho\right]^2}{\int_0^a \left|E_f(\rho, z_f)\right|^2 \rho d\rho} \tag{5-8}$$

Using Eq.(5-8), the fractional power in the fundamental beam mode is calculated and shown in Fig. 5.3. Its peak value is 99.01% and is given for the beam radius,

$$\frac{W_f}{a} = 0.6348 \tag{5-9}$$

Thus, the Feed-reflector can have a very high fundamental Gaussian beam mode component. Fig. 5.4 shows the coefficients of the first 30 modes calculated by Eq.(5-3),

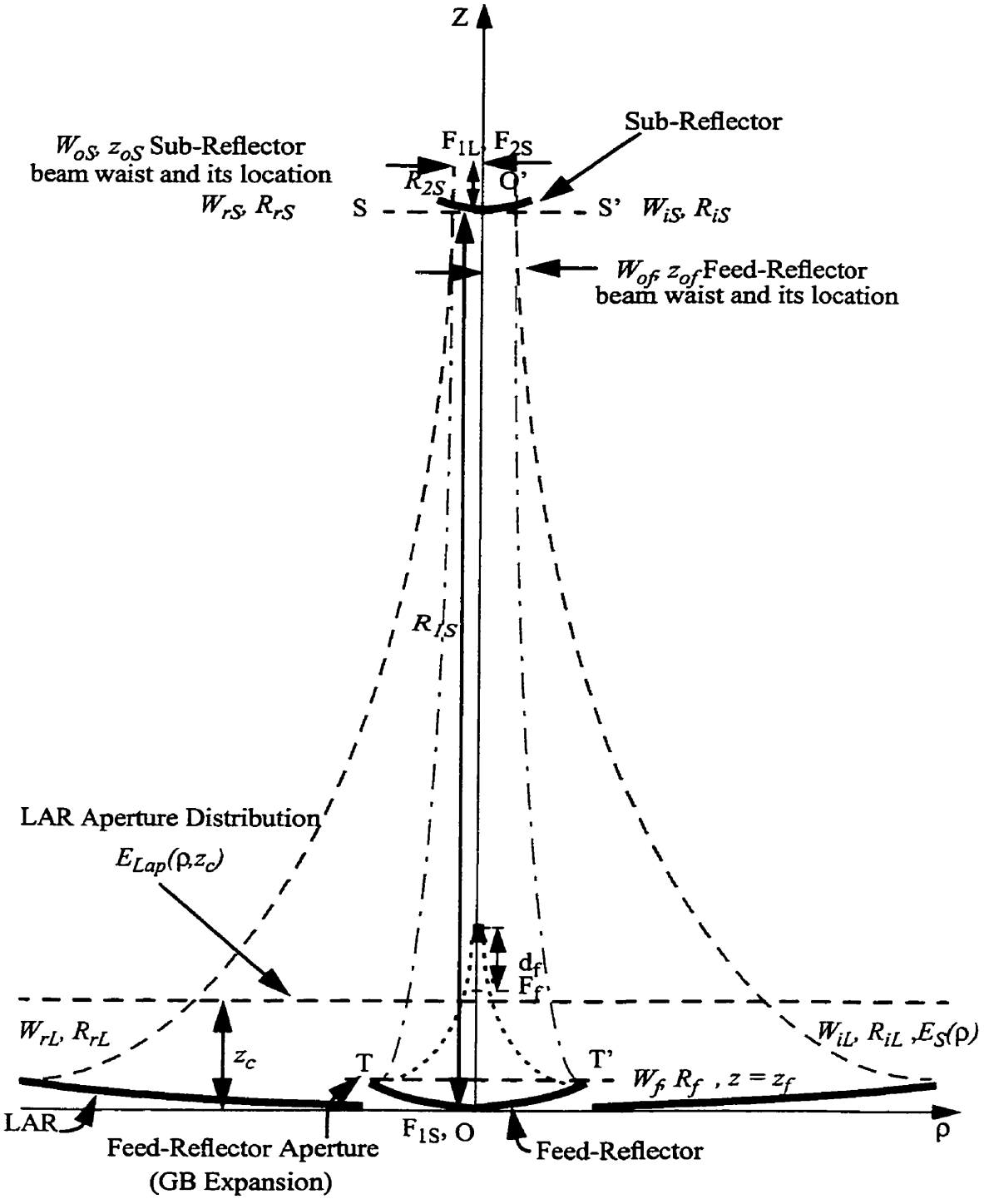

Figure 5.2: A Gaussian beam diagram for the LAR

which indicates that only the first few modes contribute to the aperture field distribution. Fig. 5.5a shows a comparison between the Feed-Reflector aperture distribution obtained by PO and its interpolation by Gaussian-Laguerre modes using both the fundamental mode and the first 30 modes.

The Feed-Reflector radius of curvature R_f at its aperture, can be determined from the Feed-Reflector aperture phase distribution, calculated by PO as shown in Fig. 5.5b. However, for a defocused paraboloid reflector, the aperture phase distribution as a function of radius is not entirely a quadratic function, especially for small ratios of f/D. That means the appropriate value of R_f must be found through a trial and error procedure to minimize the difference between the actual aperture phase distribution and the quadratic term of the phase component of the Gaussian-beam mode representation given by Eq.(5-1). For the above mentioned system, R_f = -467.75 m minimizes this error at 3 GHz. The aperture phase distribution and its equivalent quadratic phase representation, on the Feed-Reflector aperture, are shown in Fig. 5.5b. It shows that, their difference increases towards the edge of the Feed-Reflector, but as it will be shown later the selected representation is adequate.

Fig. 5.6 shows the Feed-Reflector near field radiation pattern at the sub-reflector location (z = 489.824 m), obtained by both the Gaussian beam mode expansion of Eq.(5-1) and the PO technique. The comparison between them reveals an excellent agreement for the main beam down to -25 dB, adequate enough to satisfy the LAR design requirements with a 5 m diameter sub-reflector. Considerable discrepancies are, however, observed for the side-lobes, which are due to imperfect match between the aperture phase distribution and Gaussian-beam radius of curvature. W_{iS} and R_{iS} are the beam radius and the radius of

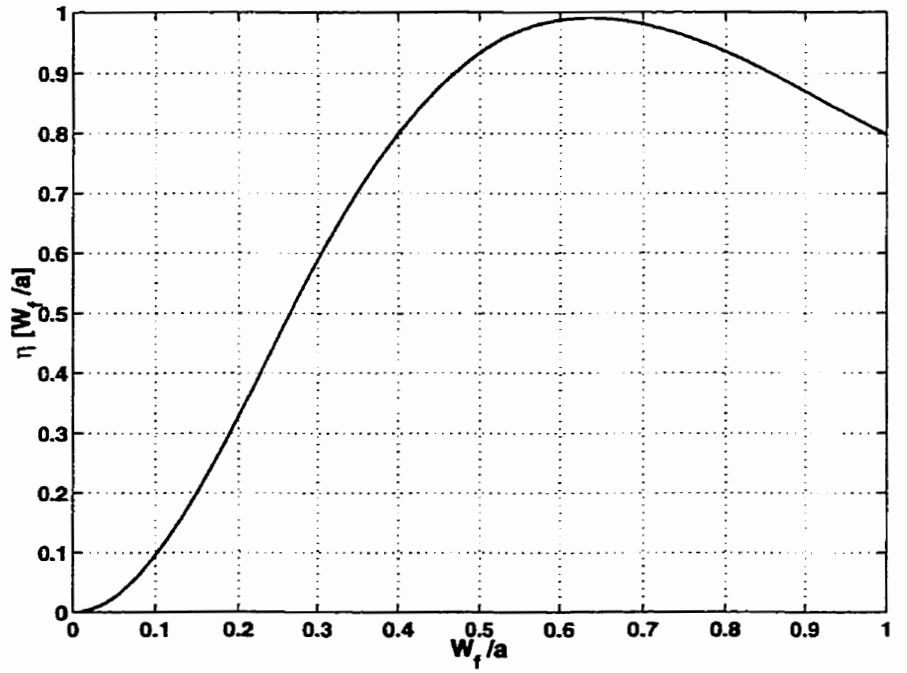

Figure 5.3: First Gaussian-Laguerre mode efficiency versus beam radius, W_f, for the Feed-Reflector at 3 GHz (a =12.5 m)

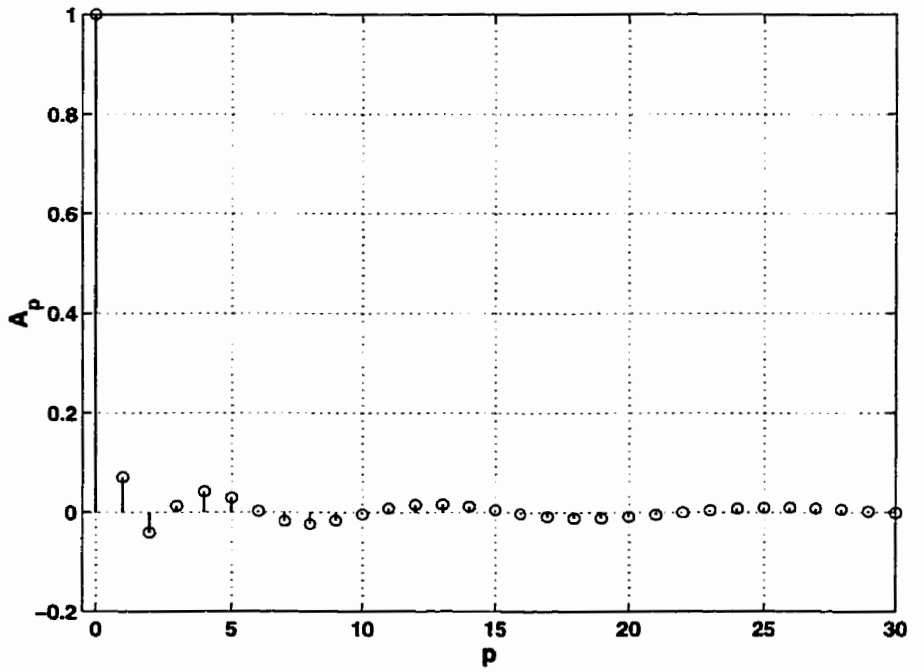

Figure 5.4: Normalized amplitude coefficients for the Gaussian-Laguerre beam-mode expansion of the field at the Feed-Reflector aperture at 3 GHz

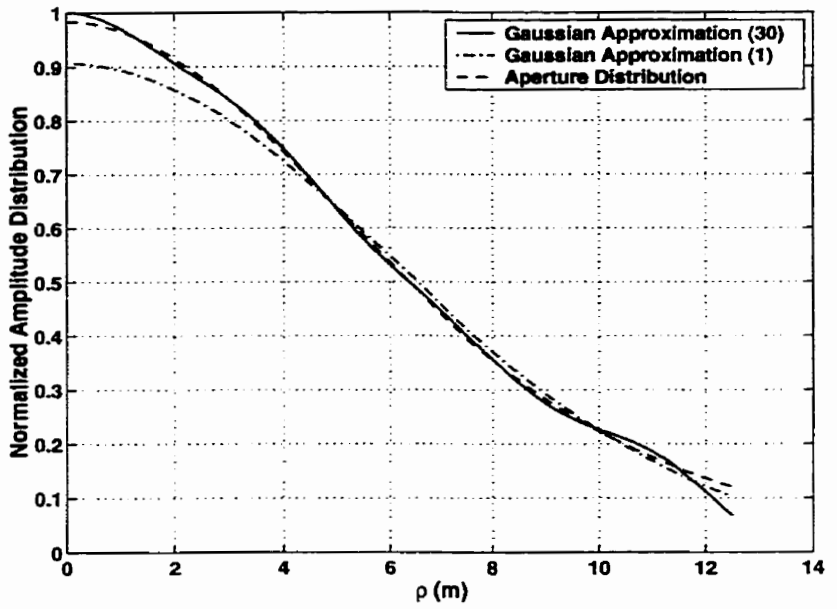

(a)

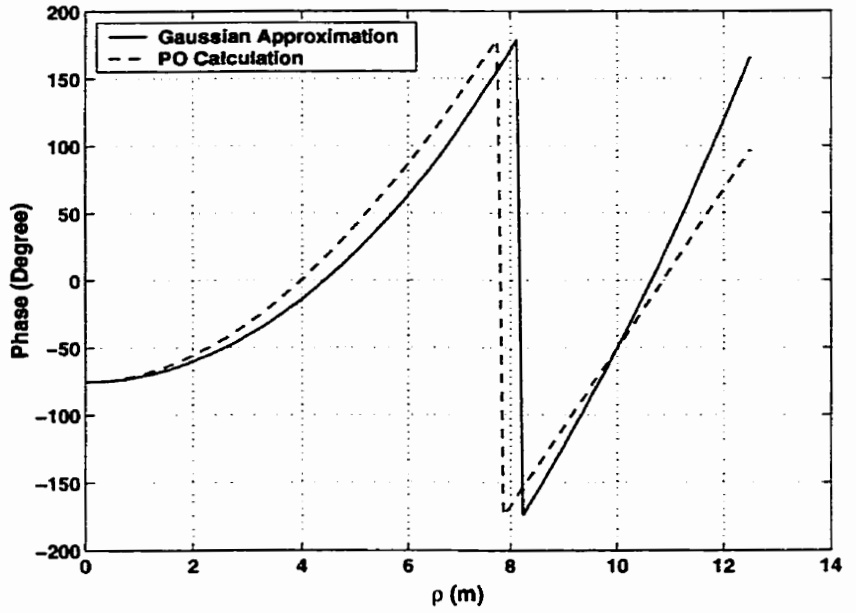

(b)

Figure 5.5: a) Feed-Reflector normalized aperture amplitude distribution and its 1 and 30 modes Gaussian-Laguerre approximations, b) Feed-Reflector aperture phase distribution and Gaussian beam approximation, d_f=0.23 m, D_F =25 m, T_a = -15 dB, f =3 GHz

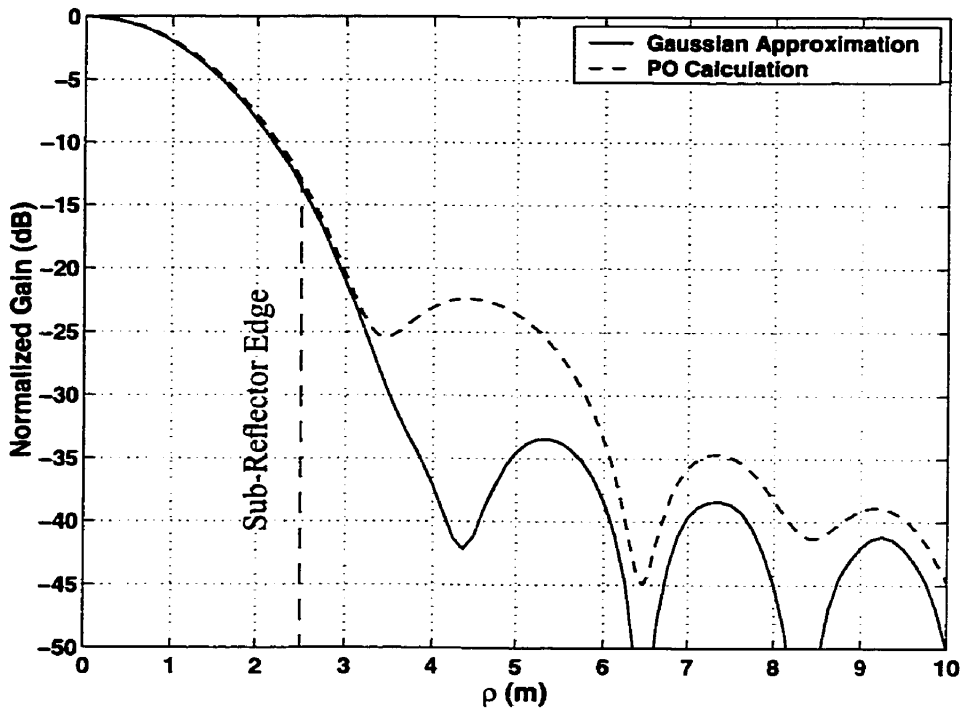

Figure 5.6: Feed-Reflector near field radiation pattern at 3 GHz and z = 489.824

curvature of the incident wave at the sub-reflector location and are equal to 1.9706 m, and 300.66 m, respectively. The beam waist of the Feed-Reflector W_{of} is equal to 1.8260 m, and is located at z_{of}= 447.3211 m, as shown in Fig. 5.2. Unlike feed horns for which the beam waist is located at the horn throat, the Feed-Reflector beam waist is away from its aperture. This implies that the sub-reflector must be redesigned to match this type of feed system.

5.3. Sub-Reflector and LAR Gaussian Beam Analysis

The main idea behind Gaussian beam analysis of the LAR system is to acquire the sub-reflector parameters, and investigate the LAR performance. For the purpose of initial design, one of the sub-reflector focii must be at the LAR focal point and the other one is considered to be located at the LAR vertex, i.e $2c = 500$ m. However, as it will be shown in Fig. 5.10, this is not a necessary requirement and the optimum value of $2c$ will depend on the Feed-Reflector edge taper.

The beam propagating away from the sub-reflector is still made up of the beam-modes with unchanged coefficients, A_p. Consider the plane SS', a plane at the vertex of the sub-reflector as shown in Fig. 5.2. It is considered to be as a new source plane for the sub-reflector, similar to plane TT' the Feed-Reflector aperture. Thus, in this case too, the beam parameters W_a and R_a of Eq.(5-5) can be acquired as before [71] and be designated as W_{rS} and R_{rS} by Eq.(5-6). By utilizing Eqs.(5-1) and (5-4), the field radiating from the sub-reflector can be obtained at any distance. As cited earlier, since almost the entire power is contained in the fundamental mode, the series representation can be reduced to the fundamental mode. This will simplify the analysis and will be used in the rest of this study.

To achieve the maximum efficiency from the LAR, the following conditions must be satisfied:

- Phase distribution must be uniform over the LAR aperture (η_p)
- A compromise between the high aperture-illumination efficiency, η_i, and low spillover efficiency, η_s must be sought such that the product $\eta_s \eta_i$

is maximized.

Because only the symmetric configuration is considered here, asymmetric Gaussian beam modes which are responsible for the cross-polarization are not excited. Thus, the cross-polarization loss is assumed to be zero.

To meet the first requirement, in an ideal case, R_{iL} at the LAR, i.e.the incidental wave radius of curvature, must be equal to LAR focal length f_L which makes the reflected radius of curvature R_{rL} to be infinite according to Eq.(5-6). This results in the quadratic phase component in Eq.(5-1), i.e. $\exp\left(-j\frac{k_o\rho^2}{2R_{rL}}\right)$, to be constant at the aperture. In a conventional Cassegrainian reflector design, the uniform phase distribution at the main reflector aperture can be obtained by setting one of the sub-reflector focii at the feed horn phase centre and the other at paraboloid reflector focal point. This condition provides case $R_{iS} = R_{1S}$, $R_{rS} = R_{2S}$, and $R_{iL} = f_L$. However, by replacing the feed horn by the Feed-Reflector, R_{iS} is not equal to R_{1S} any more, as shown in Fig. 5.2. Thus the sub-reflector parameters (i.e. eccentricity, e, and focii distance, $2c$), must be calculated to match R_{iL} to the LAR focal length f_L. In other words, the LAR phase efficiency η_p must be maximized [99]

$$\eta_p = \frac{\left|\int_0^{2\pi}\int_0^{\rho_L} E_{Lap}(\rho, \phi, z_c)\rho\, d\rho\, d\phi\right|^2}{\left[\int_0^{2\pi}\int_0^{\rho_L} |E_{Lap}(\rho, \phi, z_c)|\rho\, d\rho\, d\phi\right]^2} \tag{5-10}$$

where $E_{Lap}(\rho, \phi, z_c)$ is the LAR aperture distribution at the distance z_c from its vertex, and ρ_L =100 m is the LAR radius.

To achieve the maximum aperture efficiency from LAR, the radius of curvature of the incoming wave W_{iL}, should be adjusted to minimize the spillover loss while maintain-

ing the aperture illumination efficiency as high as possible. The spillover efficiency can be calculated from [99]

$$\eta_s = \frac{\int_0^{2\pi}\int_0^{\rho_L} |E_S(\rho, \phi)|^2 \rho d\rho d\phi}{\int_0^{2\pi}\int_0^{\infty} |E_S(\rho, \phi)|^2 \rho d\rho d\phi} \tag{5-11}$$

where $|E_S(\rho,\phi)|^2$ is the power-radiation pattern of the sub-reflector at the LAR location ($z = 0$), which can be easily evaluated using Eq.(5-1) by substituting the sub-reflector parameters.

The illumination efficiency of the LAR can be expressed as[99]

$$\eta_i = \frac{1}{\pi\rho_L^2} \frac{\left[\int_0^{2\pi}\int_0^{\rho_L} |E_{Lap}(\rho, \phi, z_c)| \rho d\rho d\phi\right]^2}{\int_0^{2\pi}\int_0^{r_L} |E_{Lap}(\rho, \phi, z_c)|^2 \rho d\rho d\phi} \tag{5-12}$$

Due to the symmetry of the reflectors, $E_{Lap}(\rho,\phi,z_c) = E_{Lap}(\rho,z_c)$, and $|E_S(\rho,\phi)|^2 = |E_S(\rho)|^2$. Thus, the integrals in Eqs.(5-10)-(5-12) reduce to one dimensional integrals, which expedite the computations process.

The total LAR efficiency η_A can be computed by the product of the above mentioned efficiencies, i.e. $\eta_A = \eta_p \eta_i \eta_s$. Fig. 5.7 shows the LAR efficiency vs. sub-reflector eccentricity, when the distance between its focii, $2c$, is equal to 500 m. The maximum efficiency occurs for $e = 1.046$, which is slightly more than 80%. However, this efficiency is not attainable because of the spillover losses of the Feed-Reflector and sub-reflector, and also the effect of blockage at of LAR centre, due to the Feed-Reflector. As it will be shown later, inclusion of these parameters can reduce the efficiency of the system by as much as

10%. Thus, the overall efficiency becomes about 71%.

The sub-reflector radiation pattern at LAR location for $e = 1.046$, and $2c = 500$ m is calculated by using Eqs.(5-1), (5-4) and (5-6) and is shown in Fig. 5.8. In this figure, the sub-reflector radiation pattern with the radius of 2.5 m, computed by the PO, is also depicted. The comparison between them reveals an overall agreement. Fig. 5.2 shows the Gaussian beam reflected from the sub-reflector has a beam waist W_{oS} of 0.1617 m which is located at 0.1989 m from the sub-reflector second focal point F_{2S}.

Fig. 5.8 also shows that the LAR edge taper of -9.5 dB, which is very close to the

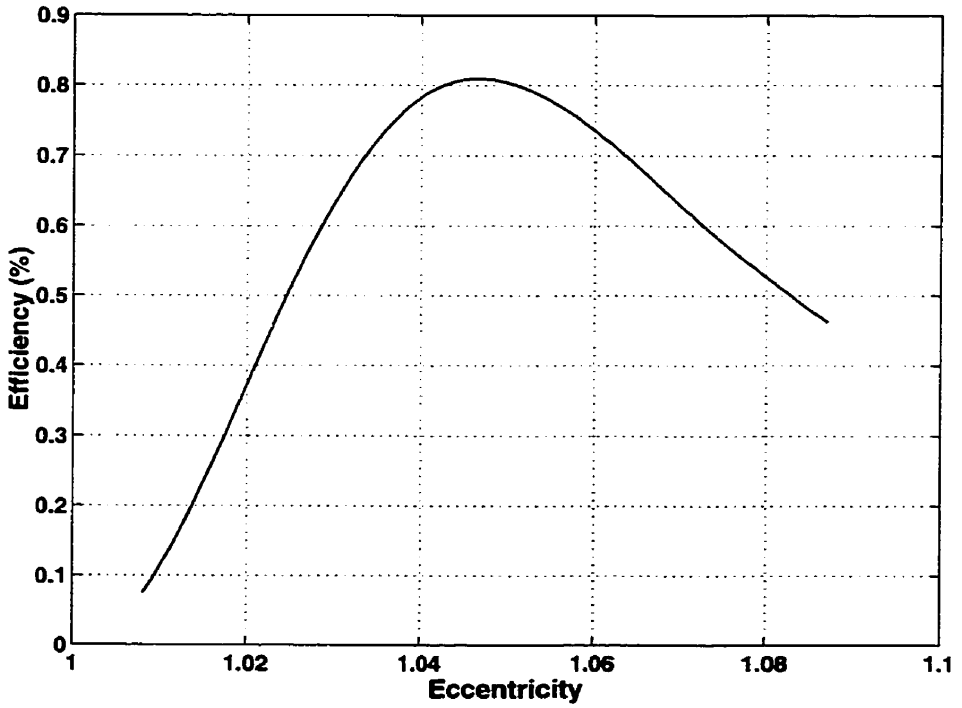

Figure 5.7: LAR efficiency vs. sub-reflector eccentricity using Gaussian beam ($\eta_A = \eta_p \eta_i \eta_s$)

beam taper of -8.7 dB at its waist (-8.7 dB). This implies that the LAR far field radiation pattern be calculated by integrating from the LAR aperture distribution instead of direct computation of the reflected Gaussian beam, as in Eq.(5-1) which requires lower edge tapers to be accurate (by substituting of LAR parameters). Following the usual aperture theory integral, the LAR far field radiation pattern can be calculated from

$$E_{far}(\Theta) = 2\pi\int_0^{\rho_L} E_{Lap}(\rho, z_c)J_o(k_o\rho\sin\Theta)\rho\, d\rho \qquad (5\text{-}13)$$

Fig. 5.9 shows the LAR normalized far field radiation patterns obtained by using Eq.(5-13) for the fundamental Gaussian mode and an accurate PO technique, which indicates a good agreement between them. The blockage effect is ignored in this graph. The CPU time required for the Gaussian beam technique is substantially less than its PO counterpart. Also in this figure, the LAR radiation pattern calculated by Eq.(5-1) is depicted, which shows considerable difference as can be predicted.

The LAR efficiency vs. the sub-reflector focii-distance is depicted in Fig. 5.10 which indicates that the maximum efficiency occurs at $2c = 250$ m. The LAR efficiency at $2c = 500$ m is only half a percent less than the maximum efficiency which indicates low sensitivity for this parameter. Fig. 5.10 also shows that the optimum $2c$ value is dependent on the Feed-Reflector edge taper and may be selected accordingly. One should, however, note that this Gaussian-beam efficiency is the limiting value for large sub-reflector and neglecting blockage and the Feed-Reflector spillover. The true LAR efficiency must be determined by the physical optics method.

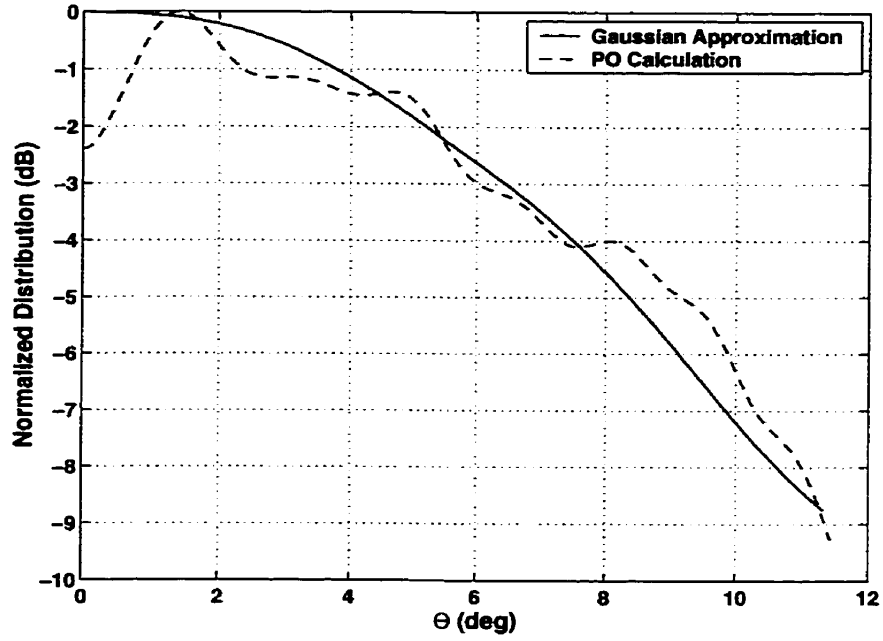

Figure 5.8: Sub-reflector radiation pattern at LAR location D_F=25 m d_f=0.23 m, T_a= -15 dB, 2c=500 m, f=3GHz, D_S=5 m, e=1.046

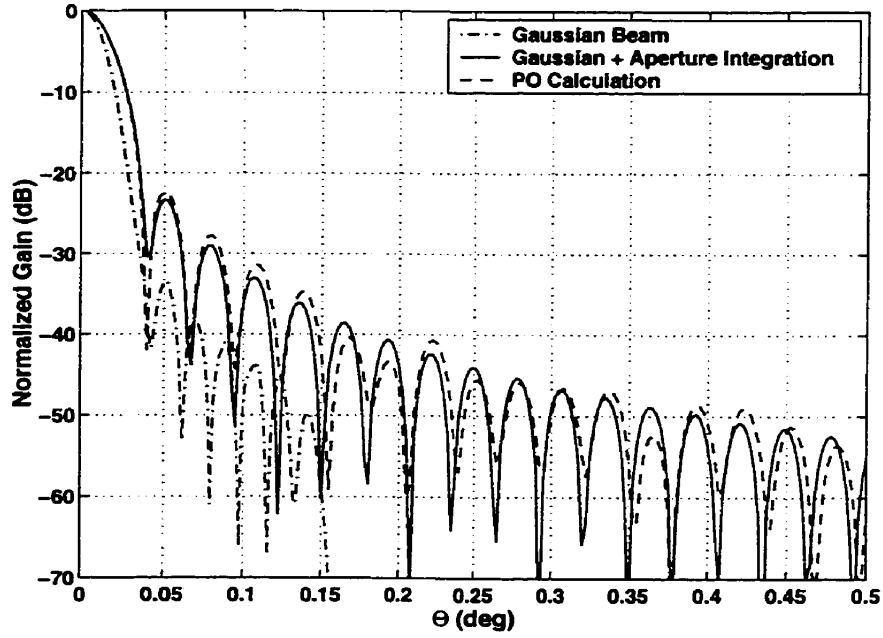

Figure 5.9: Normalized LAR radiation pattern neglecting blockage and spillover losses on the Feed-Reflector and the Sub-reflector, D_F=25 m d_f=0.23 m, T_a= -15 dB, 2c=500 m, f=3GHz, D_S=5 m, e=1.046

The LAR radiation pattern for a sub-reflector size D_S = 5 m and $2c$ = 500 m, e =1.046, and f= 3 GHz, is also calculated by using GRASP8W and displayed in Fig. 5.11. In this computation, the effect of the blockage and Feed-Reflector parasitic field on the LAR far fields are also taken into account. The efficiency of the system is about 71%, which is related to the directivity of 74.40 dBi. The half power beamwidth is 0.03 degree. The diffraction cross-polarization and the FSLL are -71.2, and -19.45 dB, respectively.

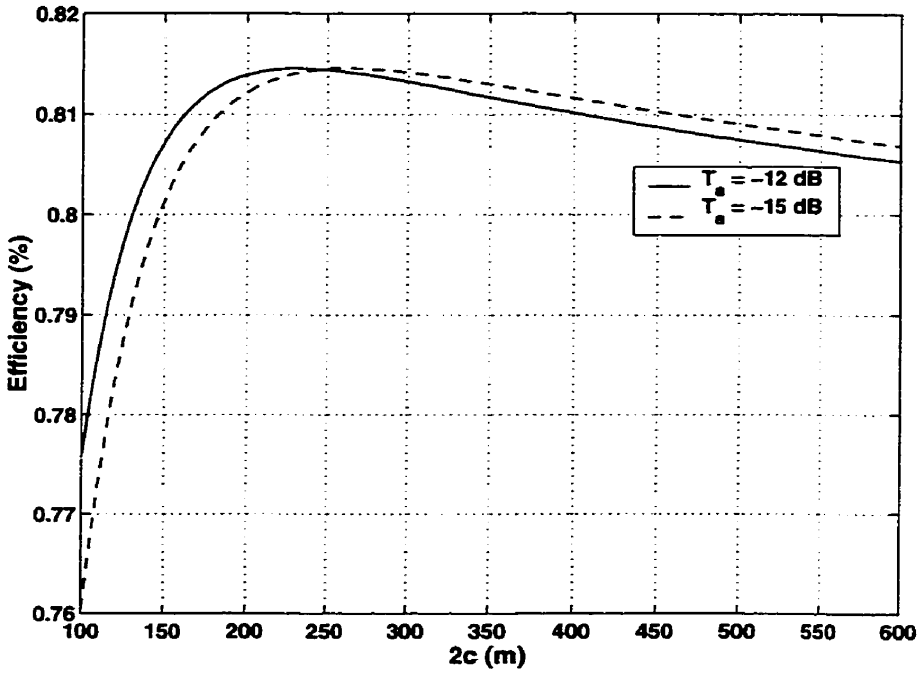

Figure 5.10: Ideal LAR efficiency vs sub-reflector foci distance for optimum eccentricity

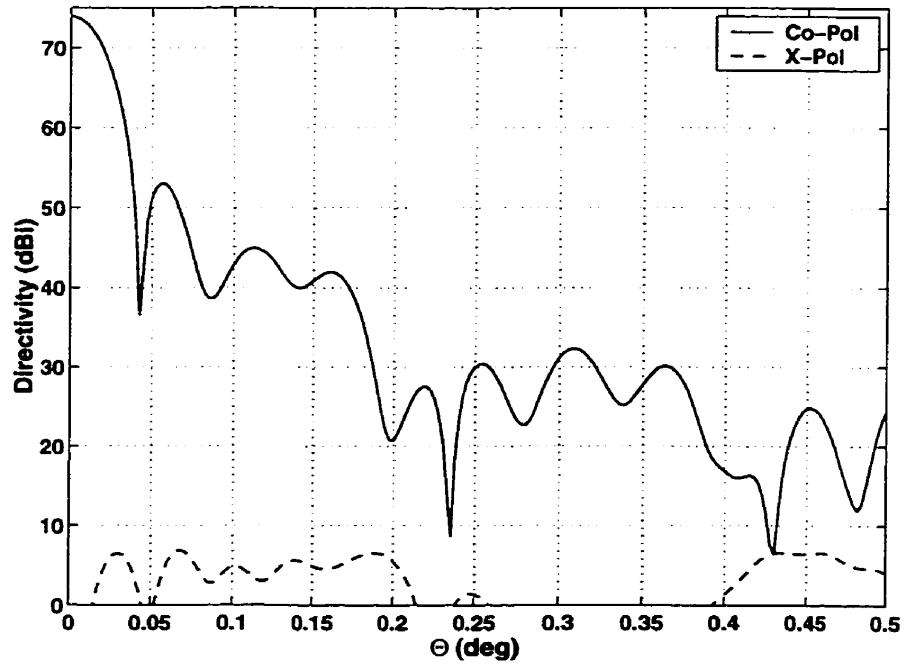

Figure 5.11: Radiation pattern of LAR calculated by PO, D_F=25 m d_f=0.23 m, T_a= -15 dB, 2c=500 m, f=3GHz, D_S=5 m, e=1.046

5.4. Conclusion

The performance of the Feed-Reflector, for a Large Adaptive Reflector Cassegrainian system was investigated by means of the Gaussian-Laguerre beam mode analysis. The electric field at the aperture of the Feed-Reflector was calculated by physical optics and expanded in terms of the Gaussian-Laguerre modes. The fractional power in the fundamental beam mode was about 99%, which indicated that it can be used as an efficient Gaussian beam launcher in quasi-optical systems. By utilizing the Gaussian beam analysis the hyperboloid sub-reflector parameters were found to maximize the LAR aperture efficiency. An overall efficiency of 71% was obtained for this system. A comparison between the physical optics and Gaussian beam approach revealed a reasonable agreement. The Gaussian beam optics provided a simple and elegant method of understanding the operation of the LAR with the Feed-Reflector system, and its optimization.

Chapter 6

CHARACTERISTICS AND DESIGN OF THE LAR OFFSET SYSTEM WITH FEED-REFLECTOR

6.1. Introduction

Offset reflector antennas are among the most common types of reflector antennas and regularly used at microwave frequencies. The offset paraboloidal reflector antennas have advantages in low side lobe levels and high efficiency, due to the lack of aperture blockage. Also the reaction of the reflector upon the primary-feed can be reduced significantly. Similar to its axisymmetric counterpart, the offset paraboloid reflector can be arranged in a dual reflector system where the main reflector is illuminated by the combination of a primary-feed and sub-reflector. The geometry of this configuration can be adjusted such that no blockage of the optical path occurs either by the primary feed or the sub-reflector.

In previous chapters the axisymmetric LAR using the Feed-Reflector was designed and investigated in detail. Several disadvantages were associated with this configuration. The major drawback was that, it could only scan over several tenths of a degree without leading to degradation of the system performance. However, the LAR beam is expected to scan to large angles up to 60°. The aperture blockage is another disadvantage of the symmetric LAR. Almost 15% of the LAR's surface had to be removed to install the Feed-Reflector which decreased the overall system efficiency. Finally, the parasitic fields from

the Feed-Reflector interfered with the main reflector radiation pattern.

In section 6.2., new equations are developed for the LAR surface, which is capable of handling large scan angles. In section 6.3., the LAR open Cassegrain system [74] is introduced and investigated. To overcome the blockage and reduce cross polarization, dual offset systems are utilized, which is the subject of investigation in section 6.4.

6.2. Geometry of Offset LAR

The geometry of an offset LAR is shown in Fig. 6.1a, where there is no direct mechanical coupling between the reflector surface and the focal point[1,104]. This allows the antenna to be steered by moving the focal point while adjusting the shape of the surface accordingly.

The system shown in Fig. 6.1a is designed to be very large, thus the airborne platform is required at or near the focus to support either a prime focus feed or sub-reflector. The LAR beam is steered by adjusting the Azimuth (Φ_{AZ}) and Zenith (Scan) Angle (θ_{ZA})of the vector, $\boldsymbol{R_o}$, of this figure. This can be done by simultaneously adjusting the shape of the surface. The main objective of the design is to allow the focal ratio, f_L / D_L, to be sufficiently large that the reflector is almost flat, which permits construction of the reflector parallel to the ground. In this design the LAR is considered as a small portion of a paraboloid who's axis is tilted to be in the scanning direction.

Because the LAR main reflector is a paraboloid, its scan capability is very limited. Thus, to accommodate large scans, the reflector surface itself must be rotated and trans-

lated with the scanning ray. But, the surface deformation of the LAR on the ground, with respect to its size, must be small due to practical actuator plays. An interesting question thus arises, "can the rotated-translated reflector surfaces of different beams, with scan angles from zero to 60 degree, share a nearly common surface?". This problem was investigated in [104] and corresponding reflector surfaces were shown to satisfy a generalized parabolic equation given by

$$\tan(\theta_{ZA})\sin(\theta_{ZA})z^2 - 4R_o\left(1+\frac{x}{2R}\sin(\theta_{ZA})\right)z + x^2\cos(\theta_{ZA}) + \frac{y^2}{\cos(\theta_{ZA})} = 0 \quad (6\text{-}1)$$

The detail of derivations of the rotated-translated paraboloids, and investigation of the resulting surface properties are provided in Appendix II. In particular, a plot of rotated-translated paraboloids are shown in Fig. II.1 and repeated in Fig. 6.1b, providing a nearly common surface on the ground for $-100 \le X \le 100$, the intended size of the LAR. The ray tracing plots of Fig. II.2 show that these paraboloid sections can be used as the LAR surface, provided the focal point is moved appropriately for each rotated angle θ_{ZA}. With this assumption, the resulting surfaces of Eq. (6-1) are used in this chapter to investigate the performance of the offset LAR. Three different configurations, which were defined in chapter 2, are designed and investigated:

- a) an open Cassegrainian LAR
- b) an optimised dual offset LAR
- c) a dual offset LAR

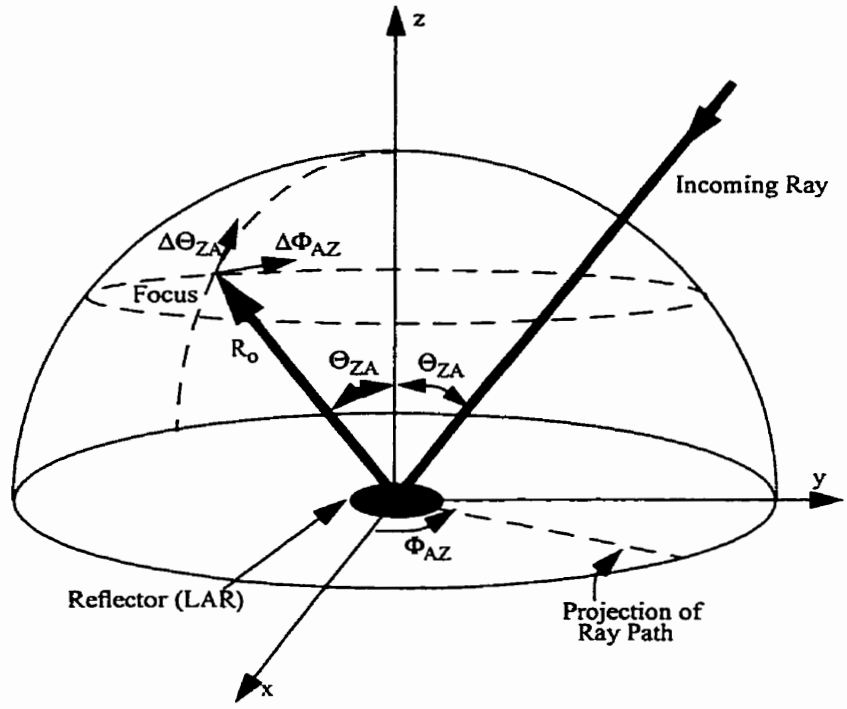

(a)

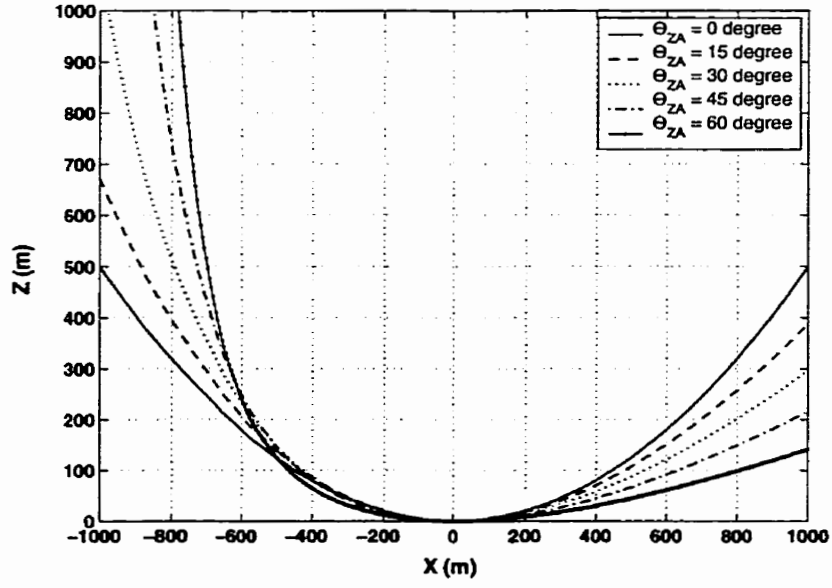

(b)

Figure 6.1: a) The Geometry of offset LAR for the scan angle θ_{ZA}. The reflector does not contain the paraboloid vertex, b) Different rotated-translated paraboloid surfaces for various rotation angles θ_{ZA} (the actual reflector is for X<\|100\|) [104]

6.3. LAR Open Cassegrainian System

Of the variety of offset Cassegrainian systems proposed in literature, perhaps the easiest for the LAR application is the open Cassegrainian antenna introduced in 1965 by Bell Telephone Laboratories [74]. The antenna, which is illustrated in Fig. 6.2 ,comprises an offset section of the LAR and symmetric section of hyperboloid sub-reflector fed by the Feed-Reflector which protrudes from an aperture in the LAR surface similar to the symmetric case. With this structure it is possible to design a system such that the sub-reflector moves in a sphere with a constant radius R_o, while its vertex faces the Feed-Reflector vertex in all scan angles. The Feed-Reflector is located in the middle of the LAR with its vertex located at (x_0, z_0) and can tilt up to 60°. Although for most scan angles the sub-reflector does not block the aperture of the main reflector (LAR), as a direct consequence of the position of the primary feed, considerable blockage due to the feed system, particularly for the large scan angles (θ_{ZA}>30°) is unavoidable.

Unlike other offset reflectors which have a circular aperture rim in the direction of maximum radiation, the LAR always has circular aperture rim at θ_{ZA} = 0°. To make the results comparable to other offset cases, in this section, in addition to a regular LAR with circular rim at θ_{ZA} = 0° for all scan angles, the LAR with circular rim in the direction of radiation (scan direction) is also considered. The latter case produces an elliptical rim at the scan angle of zero degree.

To investigate the properties of the open Cassegrainian LAR system with a hyperboloid sub-reflector, the radiation patterns of the system shown in Fig. 6.2 for D_F = 25 m,

$f_F = 9$ m, $d_f = 0.23$ m, $T_a = -15$ dB (Taper at the edge of Feed-Reflector) $D_S = 5$ m, $2c = 500$ (focii distances) and $e = 1.0424$ ($b = 489.824$, dash curve in Fig. 3.6), are calculated for scan angles of 15, 30, 45, 60 degrees at 3 GHz. Both elliptical and circular rims are considered for each angle. All radiation patterns are in the beam coordinate system as shown in Fig. 6.2. Two blockage sources occurred in this configuration, which are: i) the blockage due to the removal of the central portion of the LAR, similar to its symmetric counterpart, and ii) the shadowing blockage of the Feed-Reflector that hinders the incoming rays to reach the LAR surface. The radius of the blockage is 15 m for scan angles up to 30°, because for these scanning angles the shadowing blockage is less than the LAR removed portion. However, for larger angles, the shadowing blockage by the Feed-Reflector exceeds that from the removal of the central section and thus, further area of the LAR is blocked due to the Feed-Reflector projection effect. For example, for the scan angle of 60°, the blockage radius increases to 25 m.

Important features of this configuration are summarized in Tables 6.1 and 6.2. Also the radiation patterns for elliptical and circular rims at 30, and 60 degrees are depicted in Figs. 6.3 and 6.4 respectively. These tables and figures indicate that the side lobe level and cross-polarization increase by increasing scan angles and the efficiencies decrease. At large scan angles, the patterns in different planes do not have same beamwidth which is partly due to the blockage effect.

Table 6.1: Parameters for different Scan Angles of Open Cassegrainian LAR with elliptical aperture rim at $\theta_{ZA} = 0^o$, $D_L = 200\cos(\theta_{ZA})$ m, $D_F = 25$ m, $d_f = 0.23$ m, $D_S = 5$m

Scan Angles θ_{ZA} (deg)	45° X-Pol. (dB)	90° X-Pol. (dB)	SLL (dB)	Gain (dBi)	Efficiency (%)
15	-38.1	-35.1	-18.6	74.1	69.78
30	-32.4	-29.4	-17.9	72.9	65.91
45	-28.95	-25.95	-15.75	69.95	50.00
60	-26.22	-21.22	-11.25	64.22	27.00

Table 6.2: Parameters for different Scan Angles of Open Cassegrainian LAR with circular aperture rim at $\theta_{ZA} = 0^o$, $D_L = 200$m, $D_F = 25$ m, $d_f = 0.23$ m, $D_S = 5$m

Scan Angles θ_{ZA} (deg)	45° X-Pol. (dB)	90° X-Pol. (dB)	SLL (dB)	Gain (dBi)
15	-38.15	-35.15	-18.85	74.35
30	-30.97	-28.47	-17.72	73.72
45	-25.35	-23.65	-15.1	71.85
60	-19.5	-18.58	-13	69.38

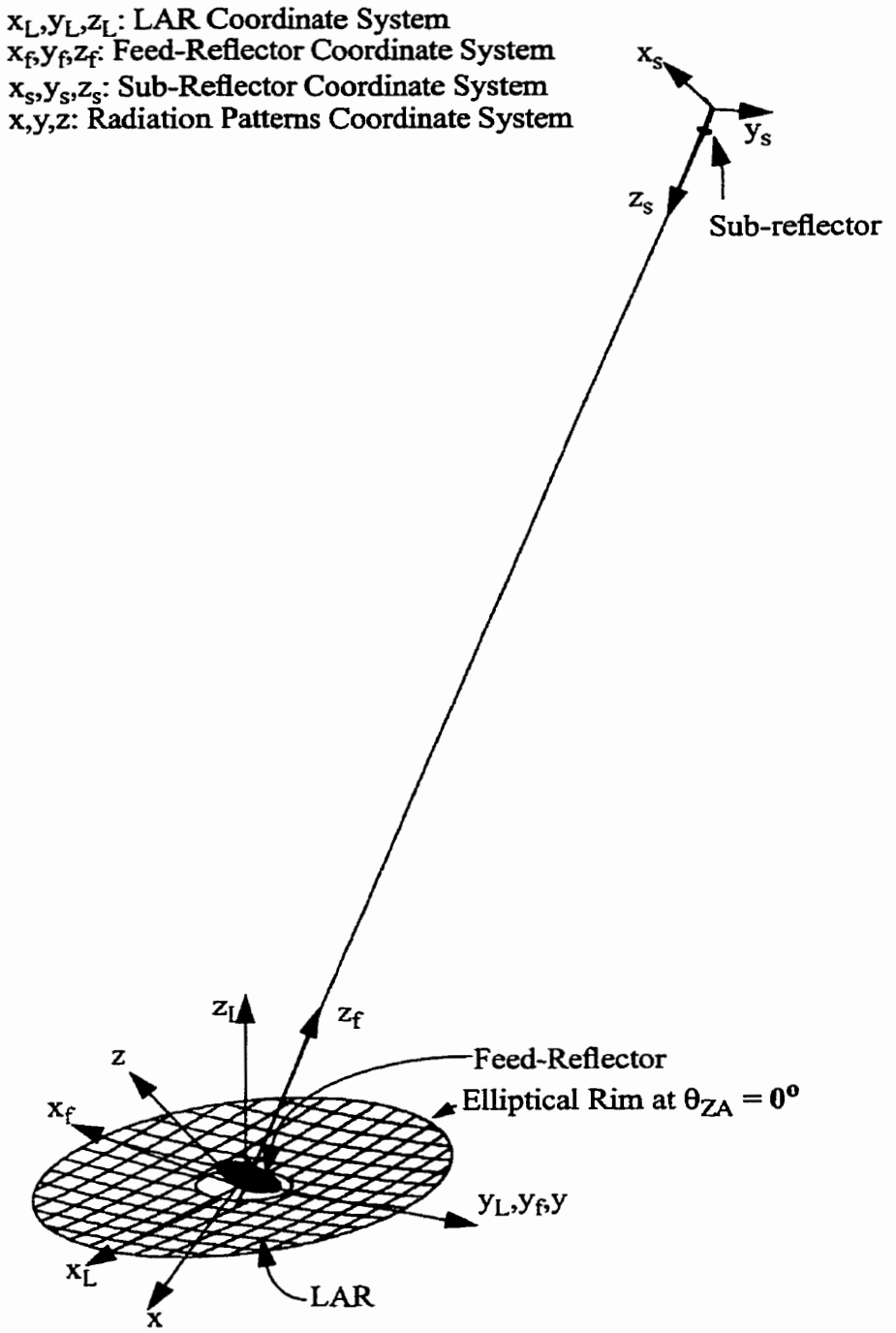

Figure 6.2: Configuration of Open Cassegrainian LAR system, with its related coordinate systems

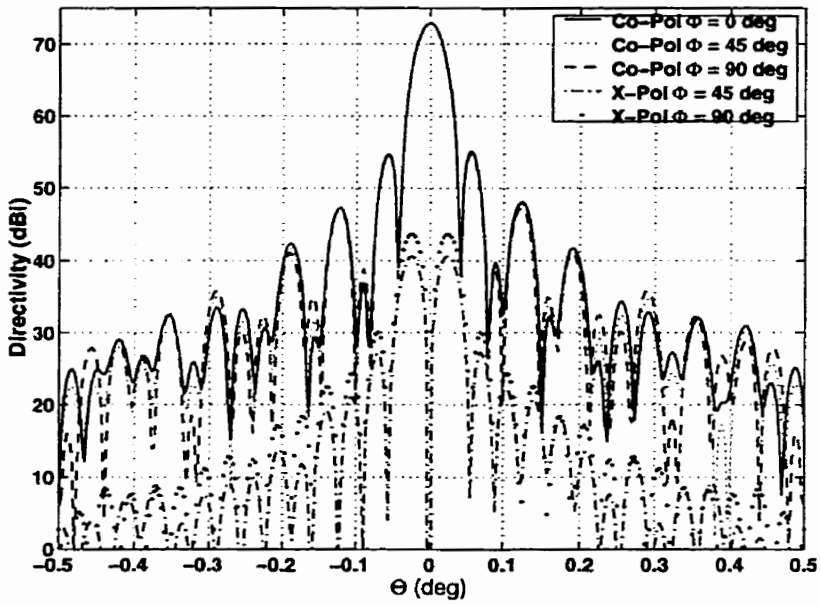

(a)

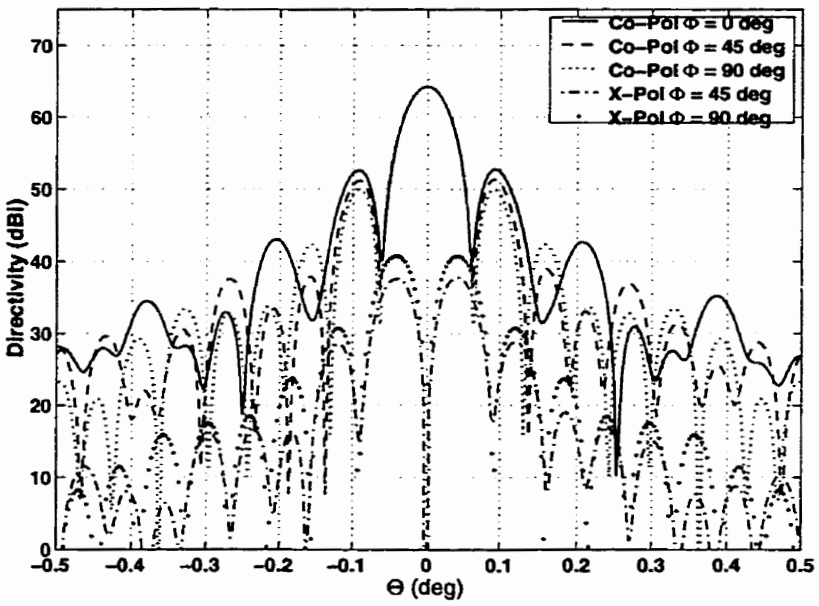

(b)

Figure 6.3: Radiation patterns of the open Cassegrainian LAR with elliptical rim at $\theta_{ZA} = 0^o$ *for a)* $\Theta_{ZA} = 30$ *deg. b)* $\Theta_{ZA} = 60$ *deg.,* $D_L = 200\cos(\Theta_{ZA})$ *m,* $D_F = 25$ *m,* $d_f = 0.23$ *m,* $D_S = 5m$

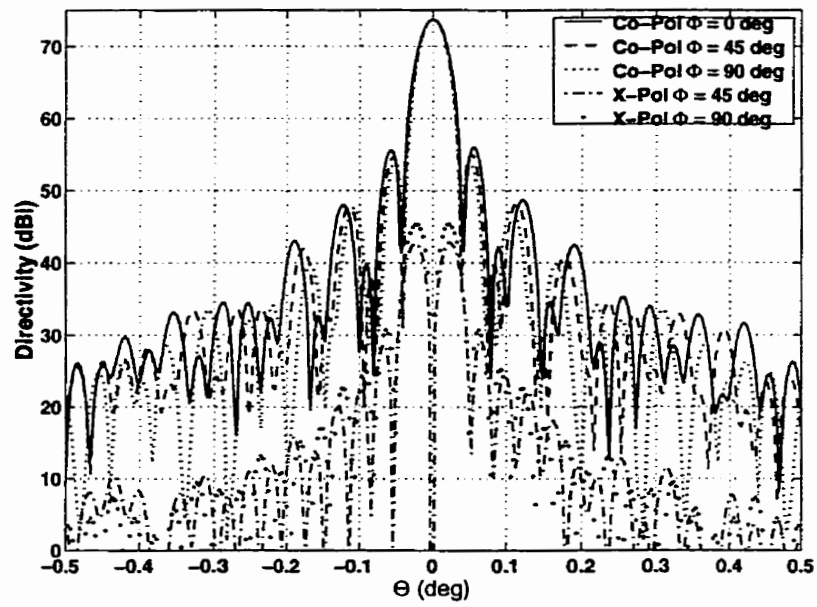

(a)

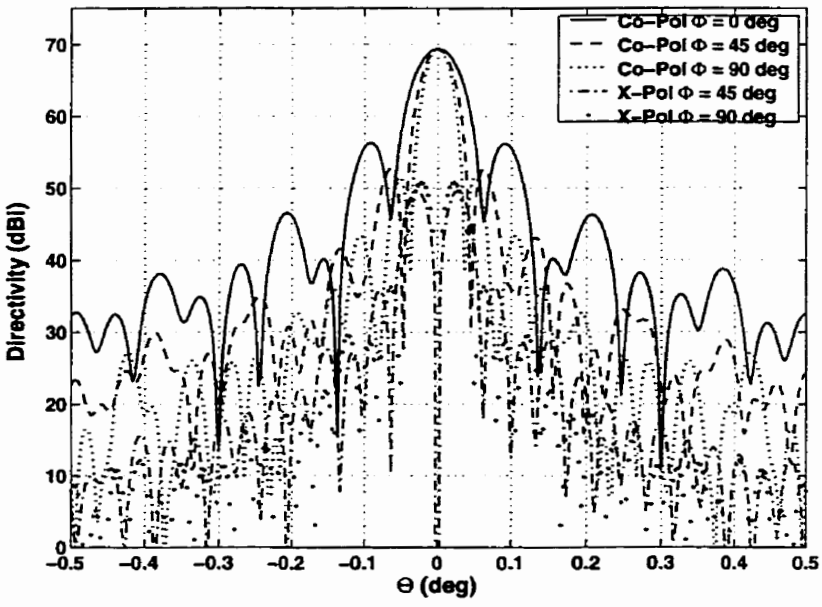

(b)

Figure 6.4: Radiation patterns of the open Cassegrainian LAR with circular rim at θ_{ZA} = 0^o *fora)* Θ_{ZA} = 30 deg. *b)* Θ_{ZA} = 60 deg.D_L = 200 m, D_F = 25 m, d_f= 0.23 m, D_S = 5m

6.4. Dual Offset Cassegrainian LAR

In the previous section, the open Cassegrainian LAR was investigated. In spite of its simple configuration, it suffers from high cross-polarization and a considerable amount of blockage, especially for large offset angles, which decreases the aperture efficiency. To overcome these difficulties an offset dual reflector configuration can be designed [78-83]. The geometry of an offset dual reflector for the LAR application is shown in Fig. 6.5. The paraboloid has a focal length f_L, and a distance R_o from its focal point to its centre equal to 500 m. The sub-reflector has an eccentricity e and interfocal distance $2c$. The axis of parent hyperboloid is tilted an angle β with respect to the axis of the parent paraboloid (LAR coordinate system). Four Cartesian coordinate systems shown in these figure are:

- x_L-y_L-z_L, the LAR coordinate system centred at paraboloid (LAR) focus.
- x_S-y_S-z_S, the sub-reflector coordinate system centred at paraboloid focus.
- x_F-y_F-z_F, the Feed-Reflector coordinate system centred at the second hyperboloid focal point which coincides the Feed-Reflector vertex.
- x-y-z, the beam coordinate system, where z-axis is located at the centre ray. x-axis is in the plane of incidence and y-axis is normal to the plane of incidence.

Each one of these Cartesian systems is assumed to have an associated spherical coordinate system, namely r_L-θ_L-Φ_L, r_S-θ_S-Φ_S, r_F-θ_F-Φ_F, and r-θ-Φ, respectively. The feed parameters are the sub-reflector edge angle θ_e, as observed from the Feed-Reflector vertex, and

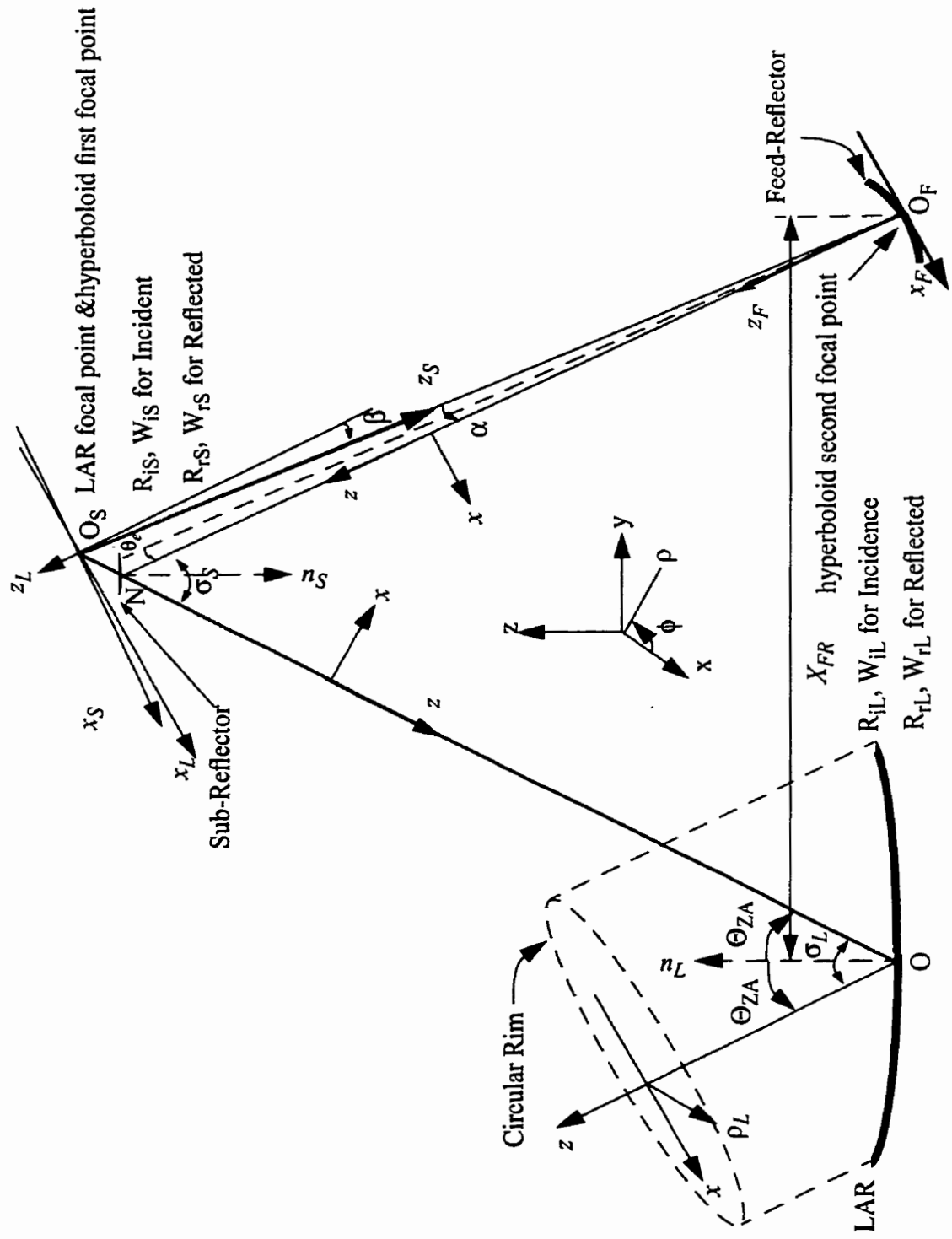

Figure 6.5: Dual offset reflector LAR configuration, R and W are the Gaussian beam parameters of each reflector

the feed pointing angle α.

The additional parameters which are of interest in this work are X_{FR} the distance between the LAR and the Feed-Reflector vertices; R_{1S} and R_{2S} which are equal to O_FN, and O_SN, respectively. To make this system comparable to classical dual offset reflectors, the LAR rim is considered to be circular in the x-y plane of the radiation pattern coordinate system (Fig. 6.5).

To design the above system, in addition to the LAR parameters which were defined in chapter 1, R_{1S}, R_{2S}, X_{FR}, α, β, e, $2c$, and θ_e (Feed-Reflector subtended angle) must be known. The sub-reflector is assumed to have a projection of 5 m diameter in x_F-y_F plane, thus, $\theta_e = 0.2905^\circ$. The other seven parameters can be determined to minimize the LAR cross-polarization and maximize its aperture efficiency. Of the above parameters, only four of them, i.e. α, β, e, and $2c$, can be independently specified.

It is well known that a dual offset reflector configuration can eliminate geometrical optics cross-polarization in the main reflector aperture through Mizugutchi's condition [79]. However, introducing the Feed-Reflector, instead of a feed horn antenna, imposes new situations which requires the Mizugutchi's condition to be verified for this new system. A powerful and convenient means to analyze the LAR system, as quoted in chapter 5, is the Gaussian-beam mode technique. In the next sub-section the generalized Gaussian modes representation of the cross-polarization fields will be introduced. These modes are launched at any offset section of a conical surface and by proper orientation of the LAR and the sub-reflector, the modes introduced at each section can cancel each other. Adding these modes help to understand the field propagation between the sub-reflector and the

LAR. The maximum efficiency from the LAR aperture can be obtained by a precise selection of the Gaussian-modes parameters at the LAR, i.e. W_{iL}, R_{iL} (beam radius and the radius of curvature of the incident wave).

6.4.1. Generalized Gauss-Laguerre Beam Modes

For a beam coordinate system with a cylindrical coordinates of (ρ, ϕ, z) (Fig. 6.5) the general form of Eq.(5-1) is [100]

$$E(\rho, \Phi, z) = \sum_{p=0}^{\infty}\sum_{l=0}^{\infty} A_p^l \frac{2}{W}\sqrt{\frac{p!}{(p+l)!}}\left(\sqrt{2}\frac{\rho}{W}\right)^l L_p^l\left[\frac{2\rho^2}{W^2}\right] \exp\left(\frac{-\rho^2}{W^2}\right)\exp\left(-jk_o z - j\frac{k_o\rho^2}{2R} + j\theta_p^l - jl\phi\right) \tag{6-2}$$

where $L_p^{\,l}$ is a generalized Laguerre polynomial, and p and l are the radial and angular mode numbers. $L_p^{\,l}(x)$ obeys the differential equation [67]

$$x\frac{d^2L_p^l}{dx^2} + (l+1-x)\frac{dL_p^l}{dx} + pL_p^l = 0 \tag{6-3}$$

W and R are beam radius and radius of curvature, respectively, which are described in Eq.(5-4). The phase slippage per beam mode $\theta_p^{\,l}$, varies with z according to [102, 103]

$$\theta_p^l = (2p+l+1)tan^{-1}\{2(z-z_o)/k_o W_o^2\} \tag{6-4}$$

where z_o is the beam waist position. Following the notation used in [67], p and l refer to the standard $\mathbf{TEM}_{pl}$ mode. It will be illustrated in the next section that only two modes are used in the dual offset LAR Gaussian-beam analysis, namely $\mathbf{TEM}_{00}$, and $\mathbf{TEM}_{01}$.

6.4.2. Cross-Polarization Induced by Offset Quadratic Surface

Using the paraxial ray approximation, simple formulas for the cross polarization introduced by a curved reflector was developed in [102] and [103]. Fig. 6.6 shows a cut in x-z plane ($\phi = 0^{\circ}$, plane of incidence) of a reflector with the quadratic surface of revolution with the centre ray of the beam passing through the foci. The expression for maximum cross-polarization is[103]

$$C_{max} = \frac{W_i \kappa_{\perp} \sin\left(\frac{\sigma}{2}\right)}{\sqrt{2e}} \tag{6-5}$$

where W_i is the beam radius of the wave front by the primary radiator at the reflector. σ is the angle between incidence and reflected rays. $\kappa_{\perp}$ is the curvature of the reflector in the direction normal to the plane of incidence. Thus, the maximum cross-polarized field is in

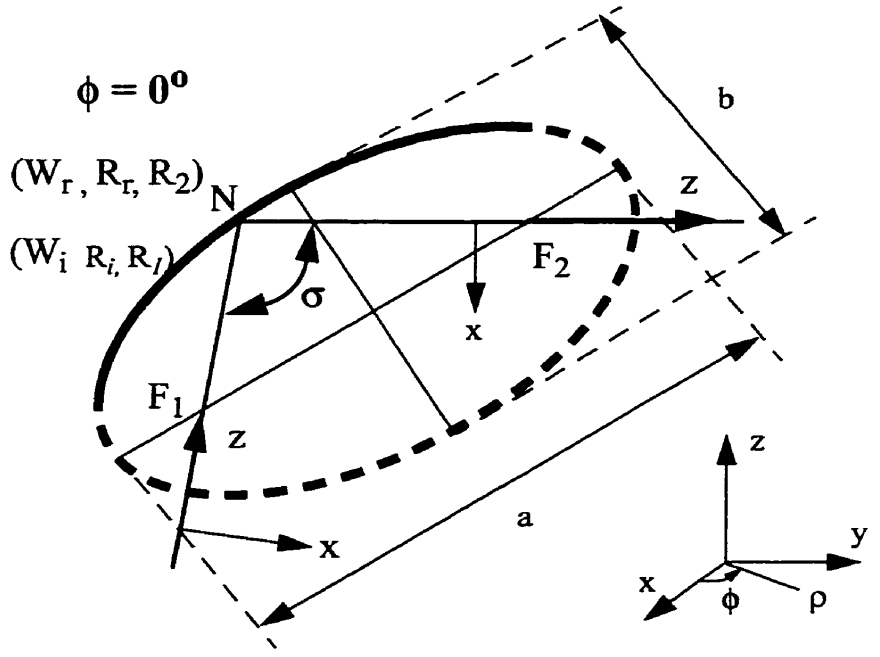

Figure 6.6: Cross-section of a conical reflector in the plane of incidence ($\phi = 0$). W_i and W_r are the beam radii of incidence and reflected wave respectively

the direction normal to the plane of incidence, which in this case is $\phi = 90^{o}$ or 270^{o} plane. The curvature in the plane perpendicular to the plane of incidence for the quadratic surface of revolution, with beam centre ray passing through the foci, is[103]

$$\kappa_{\perp} = \frac{a}{b^2} cos\left(\frac{\sigma}{2}\right) \tag{6-6}$$

where a is the major axis, and b is the minor axis of the quadratic surface. Using Eqs.(6-5) and (6-6), the maximum cross-polarization is

$$C_{max} = \frac{W_i \tan\left(\frac{\sigma}{2}\right)}{\sqrt{2}ef} \tag{6-7}$$

in this equation, f is the "focal length" of conical section and can be obtained from Eq. (5-7). The maximum cross-polarization occurs at $\rho = \frac{W_i}{\sqrt{2}}$ [100], where ρ is the distance from the centre ray (z-axis) as indicated in Fig. 6.6.

It is shown in [102] that the reflected field from an offset quadratic surface reflector can be approximately represented by a superposition of two Gaussian-beam modes. A fundamental mode with the in-line polarization is denoted by $\overline{E}_{00}$, and a higher-order Gaussian-beam mode which includes the cross-polarization is denoted by $\overline{E}_{01}$. The subscripts refer to the standard $\mathbf{TEM}_{00}$ and $\mathbf{TEM}_{01}$ modes respectively[102]. (See Appendix III for the typical aperture field decomposition into Gaussian-beam modes)

$$\overline{E}_{00} = (H_{00}\hat{x} + V_{00}\hat{y})\frac{W_0}{W}\exp\left(-jk_0 z - \frac{\rho^2}{W^2} - j\frac{k_o \rho^2}{2R} + jtan^{-1}\{2(z-z_o)/k_o W_o^2\}\right) \tag{6-8}$$

$$\bar{E}_{01} = [V_{01}(\hat{x}\cos\phi - \hat{y}\sin\phi) - H_{01}(\hat{x}\sin\phi + \hat{y}\cos\phi)]$$
$$\frac{\sqrt{2}\rho W_0}{W^2}\exp\left(-jk_0 z - \frac{\rho^2}{W^2} - j\frac{k_o\rho^2}{2R} + j2tan^{-1}\{2(z-z_o)/k_o W_o^2\}\right) \quad (6\text{-}9)$$

where H_{00}, H_{01} and V_{00}, V_{01} are the phasor coefficients for horizontally and vertically polarized fields; (ρ, ϕ, z) are the standard cylindrical coordinates[102]. W is the beam radius and can be found by Eqs.(5-4) and (5-5) from W_r.

For the $\mathbf{TEM}_{00}$ mode ($exp(-\rho^2/W^2)$), the field decreases to the e^{-1} value of its maximum on axis at $\rho = W$, whereas the $\mathbf{TEM}_{01}$ mode ($\rho\ exp(-\rho^2/W^2)$) at $\rho = W$ decreases to $\sqrt{2/e}$ of its maximum which occurs at $\rho = \frac{W}{\sqrt{2}}$.

From the above statements and by using Eqs.(6-8) and (6-9), it is found that if the higher order mode is generated by reflection from a quadratic surface with the angle between incidence and reflected rays, σ, and the curvature $\kappa_{\perp}$ in the direction perpendicular to the plane of incidence, then for convenience the parameter γ is defined as [103]

$$\gamma = \frac{V_{01}}{V_{00}} = \frac{H_{01}}{H_{00}} = \sqrt{e}C_{max} = \frac{W_i \tan\left(\frac{\sigma}{2}\right)}{\sqrt{2}f} \quad (6\text{-}10)$$

If the reflection point N is considered at $z = z_r$, there is a relative phase shift between the higher order mode and fundamental mode at an observation point $z = z_{ob}$. From Eqs. (6-8) and (6-9)[103]

$$\Delta\Phi = \Phi_{01}(z_{ob}) - \Phi_{00}(z_{ob})$$
$$= (tan^{-1}(2(z_{ob}-z_o)/k_o W_o^2) - tan^{-1}(2(z_r - z_o)/k_o W_o^2)) \quad (6\text{-}11)$$

where Φ_{00}, and Φ_{01} are phases of fundamental and higher order modes respectively. Note that, at the reflection point on the reflector, i.e. z_r, the two modes are in the phase. As the beam progresses along the z-axis, it undergoes a phase shift between the fundamental and the higher order modes.

6.4.3. Matrix Representation of Beam Mode Transformation Factors

To keep a track of the cross-polarization produced by a sequence of factors in the LAR system, it is useful to represent each factor in terms of its transmission matrix for the fundamental and higher order modes[103]. Three types of factors that affect cross-polarization in the reflection process can be categorized as follow:

- i) the reflection from a reflector
- ii) the logitudinal propagation length
- iii) the rotation of plane of incidence.

The effect of each factor is shown in Appendix IV, Fig. IV.1.

As a dual-mode beam progresses along, undergoing a number of reflections, each factor may be thought of as a reflectionless, passive, eight-port devices as shown in Appendix IV, Fig.IV2. The coupling between these two modes in the LAR system, can be stated by the matrix equation [103]

$$\bar{b} = T\bar{a} \tag{6-12}$$

where $\bar{a}$ is a vector with components being the phasors of the input modes,

$$\bar{a} = \begin{bmatrix} V_{00a} \\ H_{00a} \\ V_{01a} \\ H_{01a} \end{bmatrix} \tag{6-13}$$

and $\bar{b}$ is a vector with components being the phasors of the output modes

$$b = \begin{bmatrix} V_{00b} \\ H_{00b} \\ V_{01b} \\ H_{01b} \end{bmatrix} \tag{6-14}$$

T is a four by four matrix which explains the properties of the beam factors

$$T = \begin{bmatrix} T_{11} & T_{12} & T_{13} & T_{14} \\ T_{21} & T_{22} & T_{23} & T_{24} \\ T_{31} & T_{32} & T_{33} & T_{34} \\ T_{41} & T_{42} & T_{43} & T_{44} \end{bmatrix} \tag{6-15}$$

each of the aforementioned three factors has its own transformation matrix.

To express the beam modes in a form which allows the reflectors to be oriented arbitrary in space, the beam coordinate systems at the input and output of a reflector are defined with z-axis in the direction of propagation, x in the plane of incidence and perpendicular to z, and y normal to z and x (thus normal to the plane of incidence) so that (x, y, z) forms a right-handed cartesian system as shown in Figs. 6.5 and 6.6. Thus, the transformation matrix T_{ref} (transformation matrix for the first factor, i.e. the reflection from a reflector) for reflector is (See Appendix IV)

$$T_{ref} = \begin{bmatrix} \sqrt{1-\gamma^2} & 0 & -\gamma & 0 \\ 0 & -\sqrt{1-\gamma^2} & 0 & \gamma \\ -\gamma & 0 & -\sqrt{1-\gamma^2} & 0 \\ 0 & \gamma & 0 & \sqrt{1-\gamma^2} \end{bmatrix} \tag{6-16}$$

where γ is described in Eq.(6-10). Note that V modes (normal to plane of incidence modes) do not couple to H modes (plane of incidence modes) during reflection from a curved reflector.

As cited in the previous section, there is a relative phase shift between the higher order mode and its corresponding fundamental mode. Thus, the beam transformation matrix for a longitudinal-propagation length l is [103]

$$T_{lp} = \begin{bmatrix} 1 & 0 & 0 & 0 \\ 0 & 1 & 0 & 0 \\ 0 & 0 & e^{j\Delta\Phi} & 0 \\ 0 & 0 & 0 & e^{j\Delta\Phi} \end{bmatrix} \tag{6-17}$$

where

$$\Delta\Phi = tan^{-1}(2(z_b - z_o)/k_o W_o^2) - tan^{-1}(2(z_a - z_o)/k_o W_o^2) \tag{6-18}$$

and z_a and z_b are the position of the input and output respectively (z_b-z_a = l).

As explained before, the beam coordinate systems are attached to the plane of incidence of each reflector. Thus, as one passes from one reflector to another, the plane of incidence may rotate. From Fig. IV.1, if the plane of incidence is rotated clockwise by an angle ξ, the projection of the input modes onto the output modes produces the following

beam factor matrix for rotation of the plane of incidence [103]

$$T_{rot} = \begin{bmatrix} \cos\xi & -\sin\xi & 0 & 0 \\ \sin\xi & \cos\xi & 0 & 0 \\ 0 & 0 & \cos 2\xi & -\sin 2\xi \\ 0 & 0 & \sin 2\xi & \cos 2\xi \end{bmatrix} \tag{6-19}$$

The total transmission matrix for a beam is a multiplication of each factor matrix, that beam is undergone of its effect.

6.4.4. Application of The Gaussian-Beam Modes for Cross-Polarization Elimination

The LAR Cassegrainian system is an asymmetric configuration in the sense that the plane of incidence is rotated 180 degree, as shown in Fig.6.5 (plane of incidence rotates from the plane of $\bar{z}$ and $\bar{n}_S$ to plane of $\bar{z}$ and $\bar{n}_L$, where $\bar{n}_S$ and $\bar{n}_L$ are normal vectors to the sub-reflector and the LAR respectively). The overall matrix is the product of four beam factor matrices. A reflection from the sub-reflector ($\boldsymbol{T}_{refS}$), a 180 degree rotation of the plane of incidence ($\boldsymbol{T}_{rot\pi}$), a longitudinal propagation from the sub-reflector vertex to the LAR vertex ($\boldsymbol{T}_{lp}$), and a reflection from the LAR ($\boldsymbol{T}_{refL}$) [103].

$$T = T_{refL} T_{lp} T_{rot\pi} T_{refS} \tag{6-20}$$

Thus, using Eqs. (6-16) to (6-19) and neglecting terms of order γ^2, one finds

$$T = \begin{bmatrix} -1 & 0 & (\gamma_S + \gamma_L e^{j\Delta\Phi}) & 0 \\ 0 & -1 & 0 & (\gamma_S + \gamma_L e^{j\Delta\Phi}) \\ (\gamma_L + \gamma_S e^{j\Delta\Phi}) & 0 & e^{j\Delta\Phi} & 0 \\ 0 & (\gamma_L + \gamma_S e^{j\Delta\Phi}) & 0 & e^{j\Delta\Phi} \end{bmatrix} \tag{6-21}$$

where γ_S, and γ_L are related to the sub-reflector and the LAR and can be obtained by Eq. (6-10). Note that, γ_S is negative because f_S (the hyperboloid sub-reflector focal length) is also negative.

In Eq.(6-21),T_{13} and T_{24} show a conversion from a higher-order mode to a fundamental mode. T_{31} and T_{42} show the conversion from a fundamental mode at input to a higher-order mode at the output (cross-polarization). From Eqs.(6-10) and (6-21), the ratio C_{max} of the peak value of cross-polarization component to that of co-polarization component is [101]

$$C_{max} = \frac{1}{\sqrt{2e}}\left|\frac{W_{iS}}{f_S}\tan\left(\frac{\sigma_S}{2}\right)+\frac{W_{iL}}{f_L}\tan\left(\frac{\sigma_L}{2}\right)e^{-j\Delta\Phi}\right| \tag{6-22}$$

where the W_{iS}, and W_{iL} are the beam radii of waves incident on the sub-reflector and LAR, respectively, and σ_S and $\sigma_L = 2\theta_{ZA}$ are the angles as shown in Fig. 6.5. C_{max} can be written as an amplitude of a complex number with C_R and C_I being its real and imaginary parts respectively.

$$C = \sqrt{C_R^2 + C_I^2} \tag{6-23}$$

where from [100] and the assumption of $R_{2S} \approx R_{rS}$ and $R_{iL} \approx f_L$ for maximum LAR phase efficiency one finds

$$C_R = \frac{W_{iS}}{\sqrt{2e}}\left(\tan\left(\frac{\sigma_S}{2}\right)\cdot\frac{1}{f_S}+\tan\left(\frac{\sigma_L}{2}\right)\cdot\frac{1}{R_{2S}}\right) \tag{6-24}$$

$$C_I = \frac{1}{\sqrt{2e}}\tan\left(\frac{\sigma_L}{2}\right)\cdot\frac{1}{f_L}\cdot\frac{\lambda(f_L - R_{2S})}{\pi W_{iS}} \tag{6-25}$$

The above representation of C_R does not incorporate λ, and $C_I = 0$ when $\lambda = 0$. This means the condition $C_R = 0$ is a geometric optics condition to eliminate the cross-polarization component. Thus, to eliminate the cross-polarization component, the stipulation (6-25) can be rewritten as follows:

$$\tan\left(\frac{\sigma_S}{2}\right) \cdot \frac{1}{f_S} + \tan\left(\frac{\sigma_L}{2}\right) \cdot \frac{1}{R_{2S}} = 0 \qquad (6\text{-}26)$$

which is another form of Mizugutchi's condition[79].

6.4.5. Sub-Reflector Parameters Evaluation

The method adopted in the last chapter for designing the sub-reflector can also be applied in this section for evaluation of its parameters. However, the approach must be modified to include the effect of the asymmetric mode ($\mathbf{TEM}_{01}$). As indicated before, besides the sub-reflector eccentricity and the focii distance (i.e. e and $2c$) its orientation parameters (α, and β and also X_{FR}) the distance between the LAR and the Feed-Reflector vertices must be also calculated. Again for the purpose of initial design, one of the sub-reflector focii must be at the LAR focal point and the other one is considered to be at the Feed-Reflector vertex. However, this does not necessarily means that $2c = 500$ m. Similar to the symmetric case discussed in chapter 5, this is not a necessary requirement. The location of the sub-reflector second focal point is located on the line connecting the LAR focal point and the Feed-Reflector vertex. The separation of two focal point, $2c$, depends on the Feed-Reflector edge taper.

To achieve the maximum efficiency from the LAR, the following conditions must

be satisfied:

- Phase distribution must be uniform over the LAR aperture (η_p)
- A compromise between the high aperture-illumination efficiency, η_i, and low spillover efficiency, η_s must be sought such that the product $\eta_s \eta_i$ is maximized

The equations for phase, spillover and illumination efficiencies were shown in Eqs.(5-10), (5-11), and (5-12) respectively. In those equations, $\overline{E}_{Lap}(\rho, \phi, z_c)$ is the LAR aperture distribution at the distance z_c from its vertex, $|\overline{E}_S(\rho,\phi)|^2$ is the power-radiation pattern of the sub-reflector at the LAR location ($z = z_L$), and ρ_L =100cos(θ_{ZA}) m is the LAR aperture radius in the direction of propagation.

By carrying out Eq.(6-26) and neglecting C_I, it can be found that $\overline{E}_{Lap}(\rho, \phi, z_c)$ has only a component in co-polar direction, i.e. *y*. However, $\overline{E}_S(\rho,\phi)$ can be written as

$$\overline{E}_S = V_{00}\left[\hat{x}\left(\gamma\frac{\sqrt{2}\rho W_o}{W^2}e^{j\Delta\Phi}\cos(\phi)\right)+\hat{y}\left(\frac{W_0}{W}-\gamma\frac{\sqrt{2}\rho W_o}{W^2}e^{j\Delta\Phi}\sin(\phi)\right)\right] \exp\left(-\frac{\rho^2}{W^2}-j\frac{k_o\rho^2}{2R}\right) \tag{6-27}$$

thus

$$|\overline{E}_S|^2 = \overline{E}_S \bullet \overline{E}_S^* = \left(\frac{W_o}{W}\right)^2\left(2\gamma^2\frac{\rho^2}{W^2}+1-2\sqrt{2}\gamma\frac{\rho}{W}\cos(\Delta\Phi)\sin(\phi)\right)\exp\left(-2\frac{\rho^2}{W^2}\right) \tag{6-28}$$

By utilizing the above two equations in Eqs.(5-10)-(5-12), for the maximum LAR

aperture efficiency, σ_S, R_{2S}, $2c$ and e can be determined uniquely. From Fig. 6.5,α, β and X_{FR} are

$$\frac{\sin(\alpha)}{R_{2S}} = \frac{\sin(\pi - \sigma_S)}{2c} \tag{6-29}$$

$$\beta = \sigma_L + \alpha - \sigma_S \tag{6-30}$$

$$\frac{\sin(\sigma_S)}{X_{FR}} = \frac{\sin\left(\frac{\pi}{2} + \frac{\sigma_L}{2} - \sigma_S\right)}{R_o} \tag{6-31}$$

where R_o is distance between the LAR vertex and its focal point.

6.4.6. Results for Scan Angles Greater Than 7 Degree (Optimised Dual Offset LAR)

Utilizing the above theories pave the way to design and analyze the dual offset LAR. A system similar to the one shown in Fig. 6.5 is designed. The characteristics and the performances of the system are investigated for different zenith angles (or scan angle θ_{ZA}) on the LAR operating frequencies (1-22 GHz). A summary of parameters and results obtained are presented below.

For the first step, the operating frequency is considered to be 3 GHz and scan angles vary between 7- 60 degrees. Scan angles less than 7^o are examined later in the next sub-section. Parameters of the system are displayed in Figs. 6.7-6.9. All these parameters are evaluated to maximize the LAR aperture efficiency and minimizing its cross-polarization. The initial parameters to design the system are $D_L = 200\cos(\theta_{ZA})$ m, $R_o = 500$ m, $D_F = 25$ m, $f_F = 9$ m, $d_f = 0.23$ m, $D_S = 5/\cos(\theta_{ZA})$ m, $T_a = -15$ dB.

In Fig. 6.7 the eccentricity of the system defined in Eq. (4-4) is depicted for the various scan angles. Although the range of variation is small, it has a great impact on the system performance. The alternation of α and β versus scan angles are displayed in Fig. 6.8a which indicates the values for β are much less than those for α and are closed to zero. Unlike α which increases with the scan angle (θ_{ZA}), β has a peak value at 45 degree and then decreases.

The inter-focal distance of hyperboloid sub-reflector, $2c$, slightly changes over the LAR scan range as shown in Fig. 6.8b. This figure also shows the distance between the LAR and the Feed-Reflector vertices (X_{FR}) which varies from 124.65 m to 846.541m for scan angles between 7 to 60 degrees. This means that the Feed-Reflector must be able to

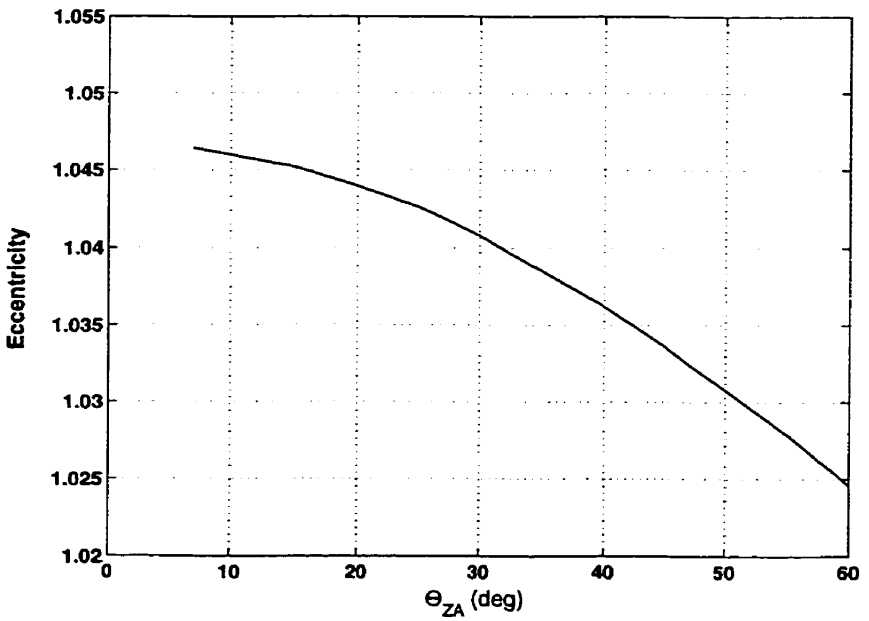

Figure 6.7: Eccentricity of dual offset LAR vs. scan angle, f =3 GHz, $D_L = 200\cos(\theta_{ZA})$ m, R_o = 500 m, D_F = 25 m, f_F = 9 m, d_f = 0.23 m, $D_S = 5/\cos(\theta_{ZA})$ m, T_a = -15 dB, for LAR Min. X-Pol. & Max. directivity

move on the area of a ring with a inner radius of 124.65 m and an outer one of 846.541. For $\theta_{ZA} < 7^{\circ}$, the inter-vertex distance of LAR and Feed-Reflector is less than 100 m, which makes the Feed-Reflector to merge with the LAR. To prevent this situation another method must be selected for these scan angles.

R_{1S} the distance between the sub-reflector second focal point and its vertex N (Fig. 6.5), and R_{iS}, the radius of curvature of the incidence beam, are shown in Fig. 6.9a. This graph indicates that in contrast to the conventional Cassegrainian configuration, considerable differences exist among the values of R_{1S} and R_{iS},and these discrepancies even increase by increasing the scan angle. However, R_{2S} and R_{rS}, the corresponding parameters of the sub-reflector, i.e. the distance between the sub-reflector first focal point and its vertex N, and the radius of curvature of the reflected beam, are almost equal.

W_{iL} and W_{iS} the beam radii of incidence waves to the LAR and the sub-reflector are shown in Fig. 6.9b. Due to the projection of the LAR surface into the direction of scan and to maintain the LAR maximum efficiency, W_{iL} decreases with an increase in the scan angle. However, W_{iS} values are nearly constant and are due to the constant Feed-Reflector subtended angle θ_e.

Efficiency and the directivity of the LAR in a dual offset configuration are shown in Figs. 6.10 and 6.11a. The efficiency of the system drops by increasing the scan angle. This is mostly because of the increase in the LAR offset angle. Maximum directivity for uniform aperture distribution of the LAR is also displayed in Fig. 6.11a. The maximum directivity also decreases because the projection of the LAR aperture in the direction of the scan angle is reduced (Fig. 6.5).

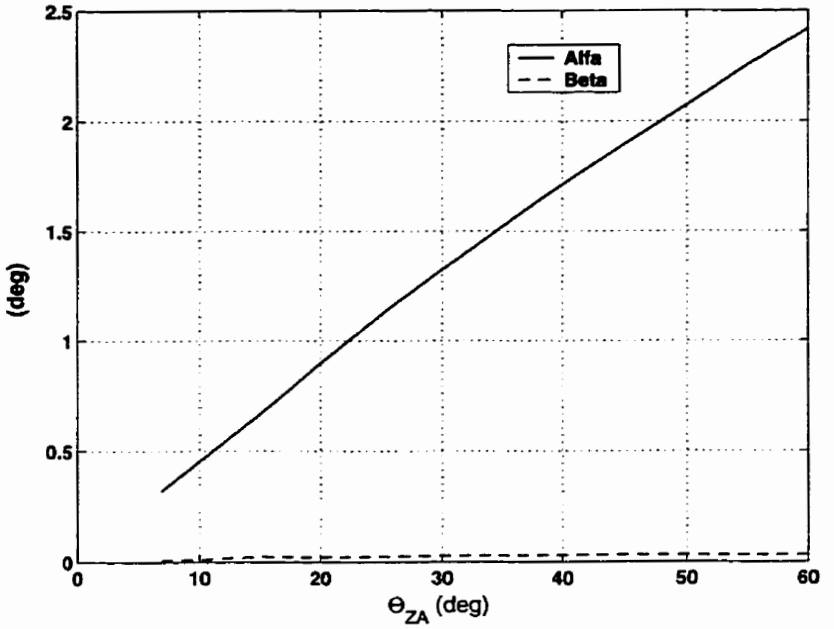

(a)

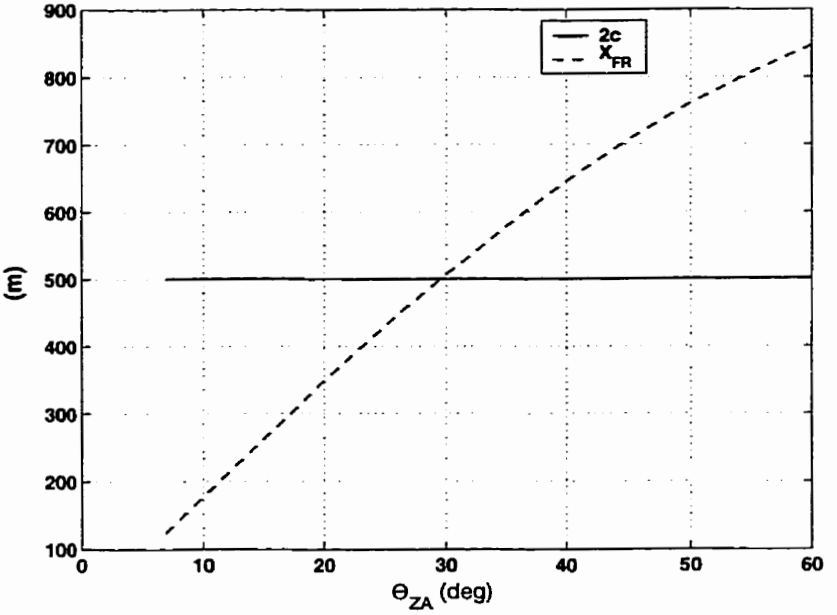

(b)

Figure 6.8: (a) α and β vs. scan angle (b) 2c and X_{FR} vs. scan angle, f =3 GHz, D_L = 200cos(θ_{ZA}) m, R_o = 500 m, D_F = 25 m, f_F = 9 m, d_f = 0.23 m, D_S = 5/cos(θ_{ZA}) m, T_a = -15 dB, for LAR Min. X-Pol. & Max. directivity

The first sidelobe level (FSLL) of the LAR for different scan angles is depicted in Fig. 6.11b, which shows its values are nearly constant and are about -24 dB. Cross-polarization of the LAR obtained by Physical Optics technique (PO+PTD) and Gaussian beam (GB) of Eq.(6-25) are also shown in this figure. As can be predicted, the cross-polarization increases with θ_{ZA}. The differences between values obtained by these two techniques is approximately 2 dB and can be elucidated as the Gaussian beam is an approximate solution.

The sub-reflector radiation patterns for the scan angles (θ_{ZA}) of 30 and 60 degrees and for different planes are shown in Figs. 6.12a and 6.12b respectively. The maximum cross-polarization occurrs at the 90° plane (orthogonal to the plane of incidence). The radiation patterns show a narrower beamwidth and higher directivity for θ_{ZA}=60° compare to θ_{ZA}=30° (The sub-reflector size for θ_{ZA}=60° is larger than for θ_{ZA}=30°).

The LAR aperture distributions for the scan angles (θ_{ZA}) of 30 and 60 degrees are illustrated in Figs. 6.13a and 6.13b respectively. The aperture field taper, on average, is 20 dB for each scan angle. The LAR radiation patterns for these scan angles are shown in Figs. 6.14a and 6.14b. These figures indicate the LAR radiation patterns are symmetric in the main beam. The maximum cross-polarization occurrs at the 90° plane which is well below the co-polarization.

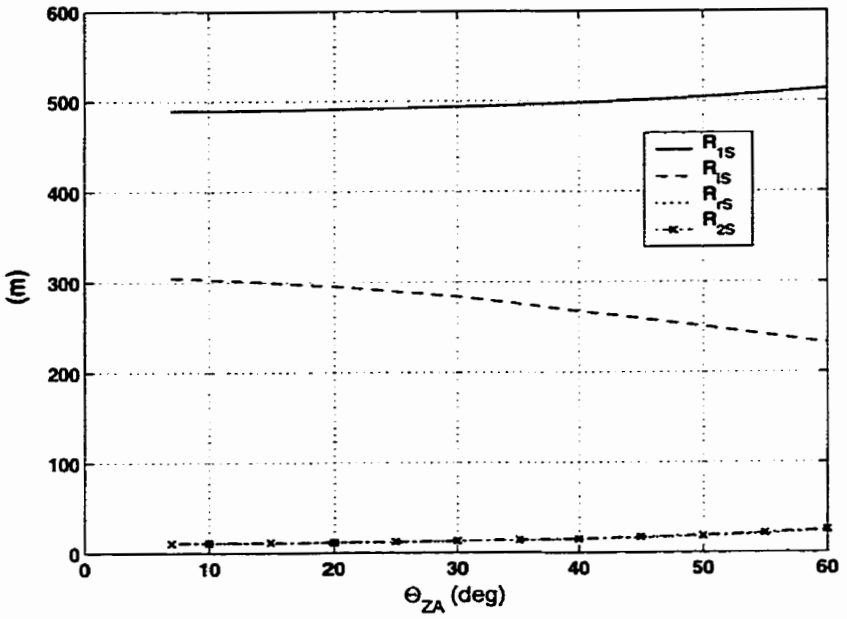

(a)

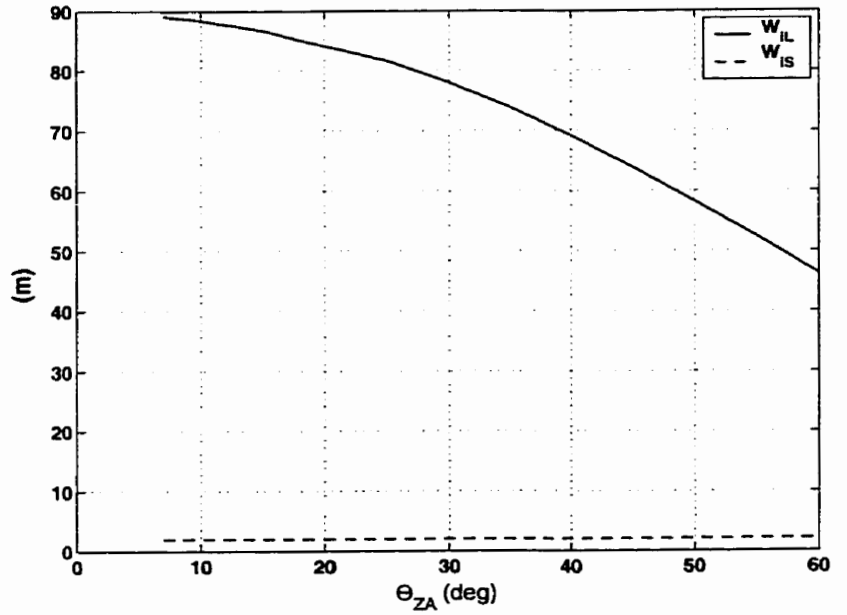

(b)

Figure 6.9: (a) R_{1S}, R_{2S}, R_{iS}, and R_{rS} vs. scan angle b) incidence beam radius on the LAR and the sub-reflector, f =3 GHz, $D_L = 200\ cos(\theta_{ZA})$ m, R_o = 500 m, D_F = 25 m, f_F = 9 m, d_f = 0.23 m, $D_S = 5/cos(\theta_{ZA})$ m, T_a = -15 dB, for LAR Min. X-Pol. & Max. directivity

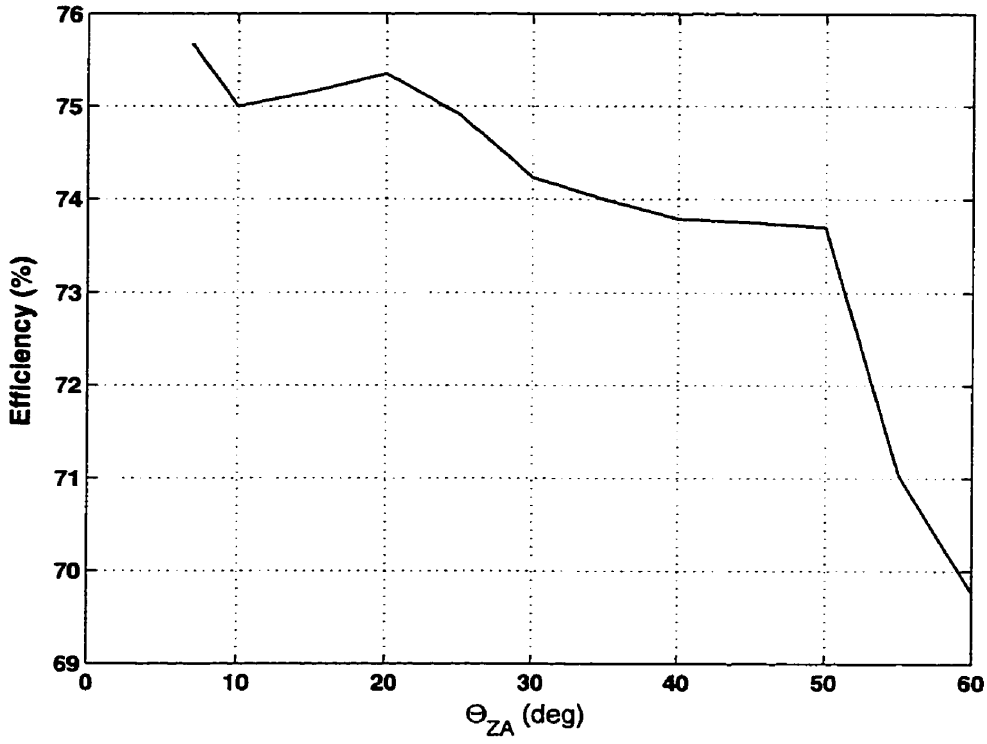

Figure 6.10: Efficiency of the dual offset LAR vs. scan angle, f =3 GHz, D_L = 200cos(θ_{ZA}) m, R_o = 500 m, D_F = 25 m, f_F = 9 m, d_f = 0.23 m, D_S = 5/cos(θ_{ZA}) m, T_a = -15 dB, for LAR Min. X-Pol. & Max. directivity

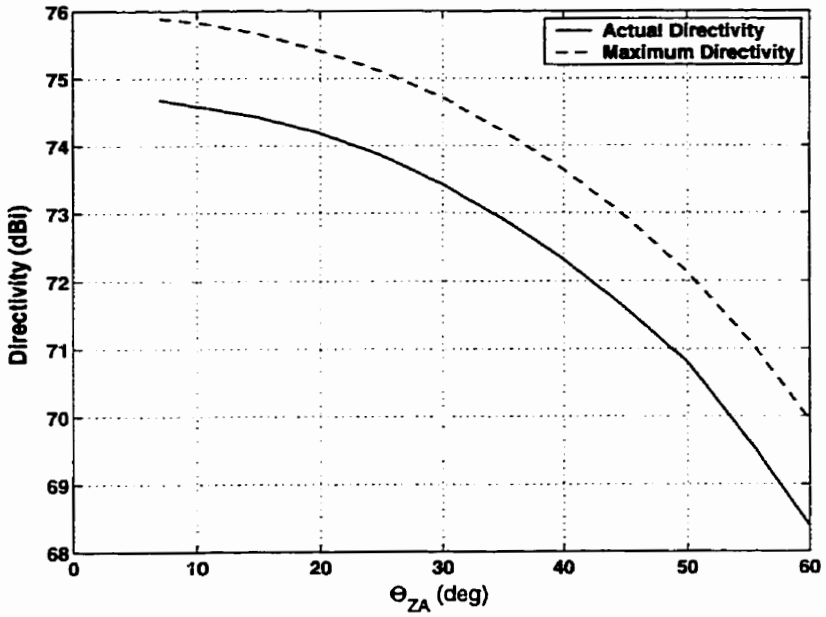

(a)

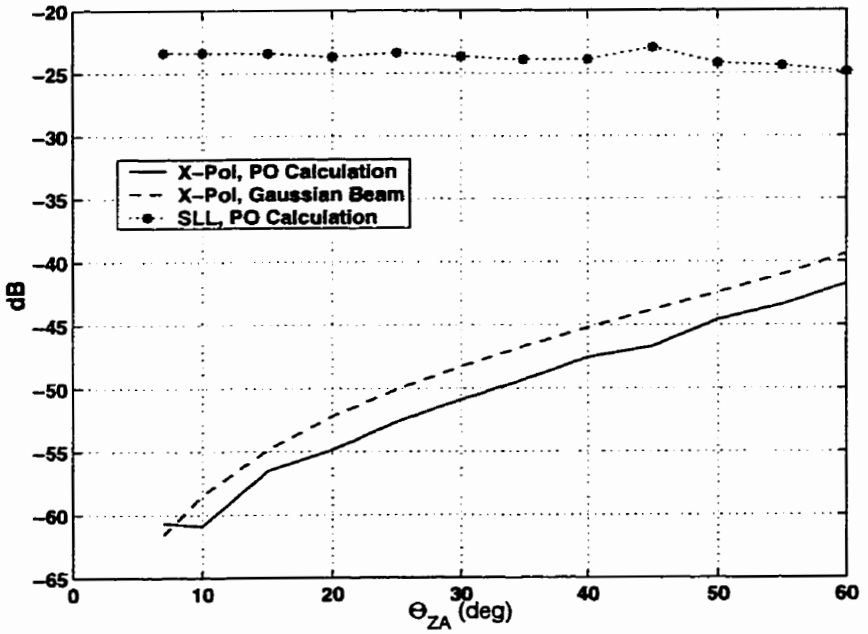

(b)

Figure 6.11: (a) Actual and maximum directivity (b) sidelobe level and cross-polarization of the dual offset LAR vs. scan angle, f =3 GHz, $D_L = 200\cos(\theta_{ZA})$ m, R_o = 500 m, D_F = 25 m, f_F = 9 m, d_f = 0.23 m, $D_S = 5/\cos(\theta_{ZA})$ m, T_a = -15 dB, for LAR Min. X-Pol. & Max. directivity

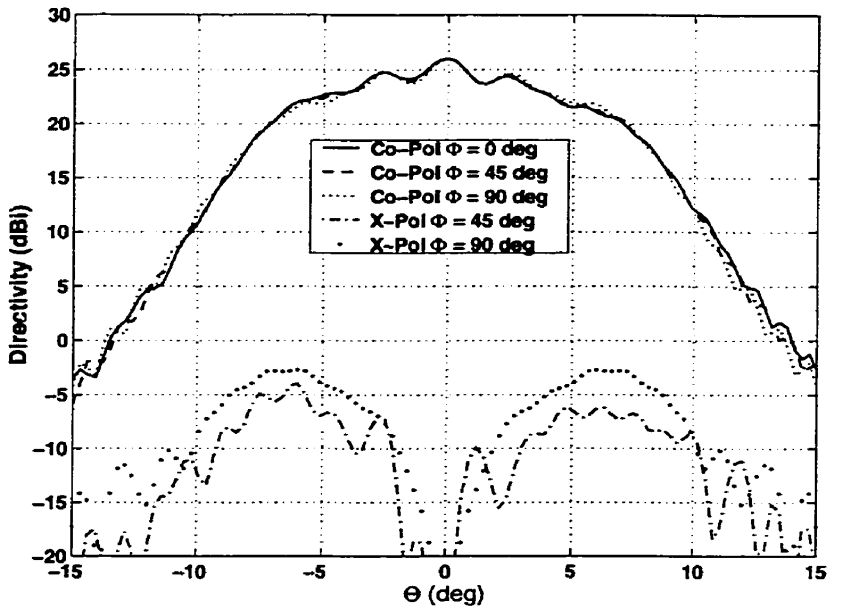

(a)

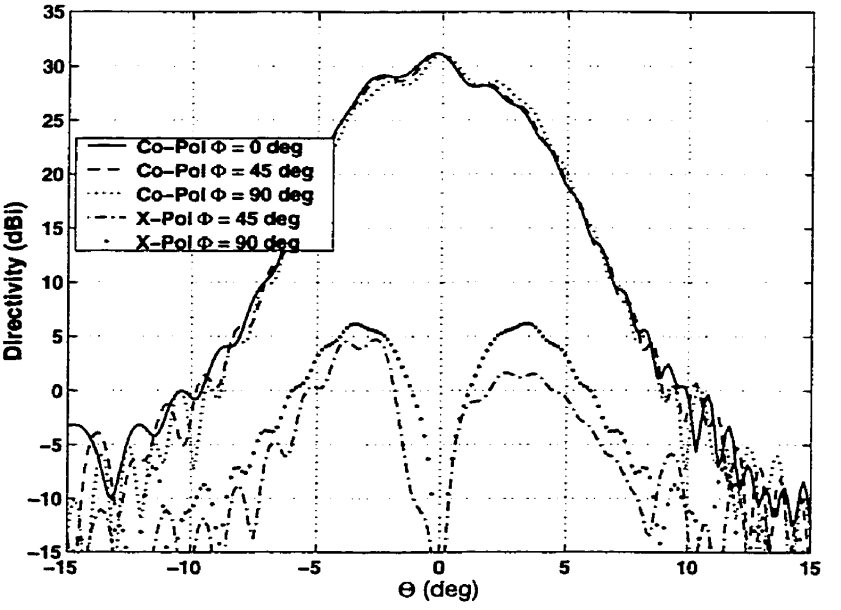

(b)

Figure 6.12: Sub-reflector radiation patterns for a) $\theta_{ZA} = 30^o$, b) $\theta_{ZA} = 60^o$, f =3 GHz, $D_L = 200\cos(\theta_{ZA})$ m, $R_o = 500$ m, $D_F = 25$ m, $f_F = 9$ m, $d_f = 0.23$ m, $D_S = 5/\cos(\theta_{ZA})$ m, $T_a = -15$ dB, for LAR Min. X-Pol. & Max. directivity

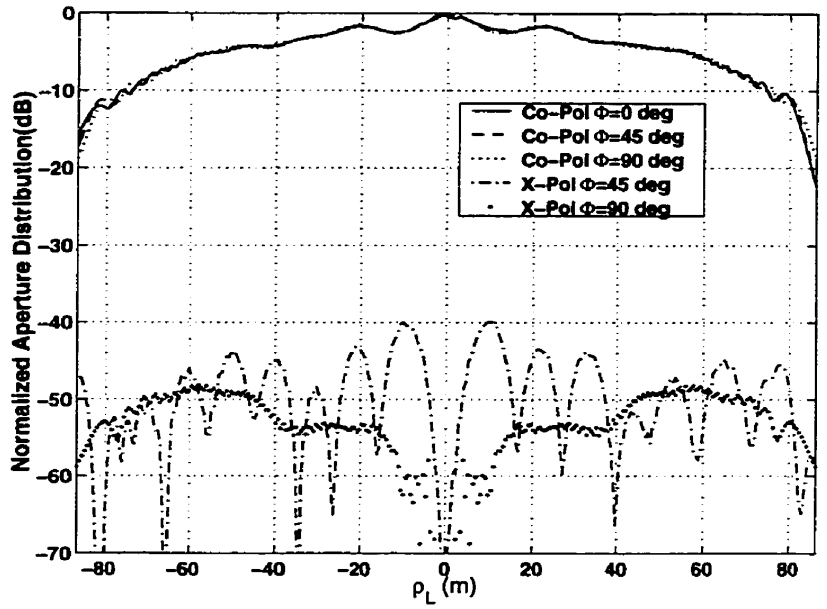

(a)

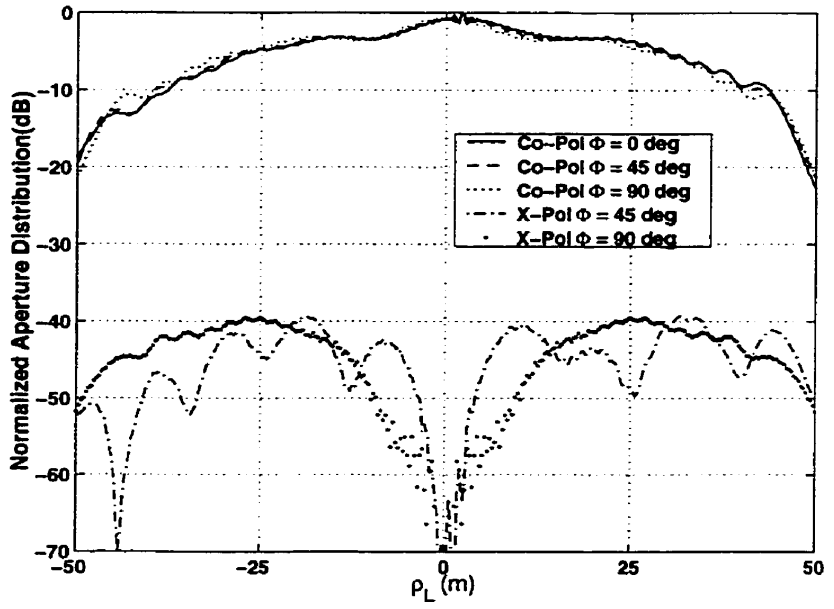

(b)

Figure 6.13: LAR aperture distributions for a) $\theta_{ZA} = 30^o$, b) $\theta_{ZA} = 60^o$, f =3 GHz, D_L = 200cos(θ_{ZA}) m, R_o = 500 m, D_F = 25 m, f_F = 9 m, d_f = 0.23 m, D_S = 5/cos(θ_{ZA}) m, T_a = -15 dB, for LAR Min. X-Pol. & Max. directivity

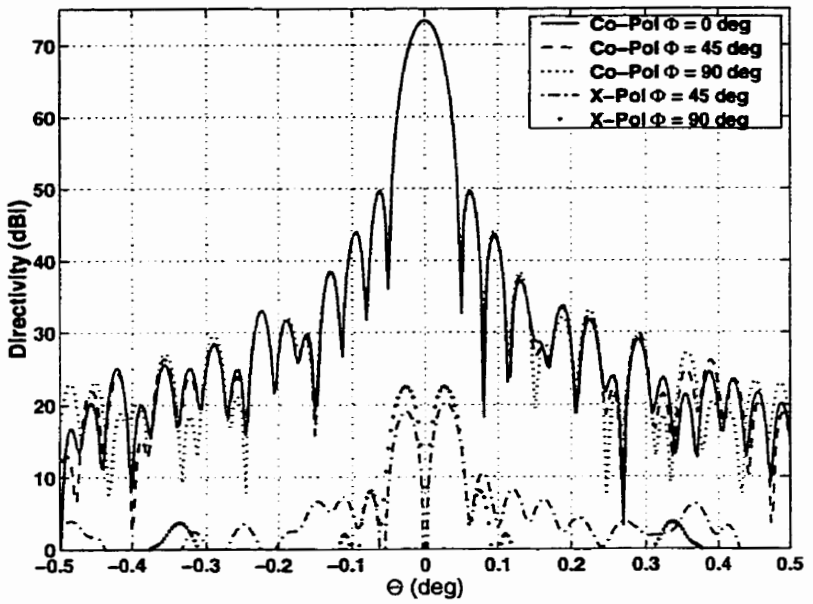

(a)

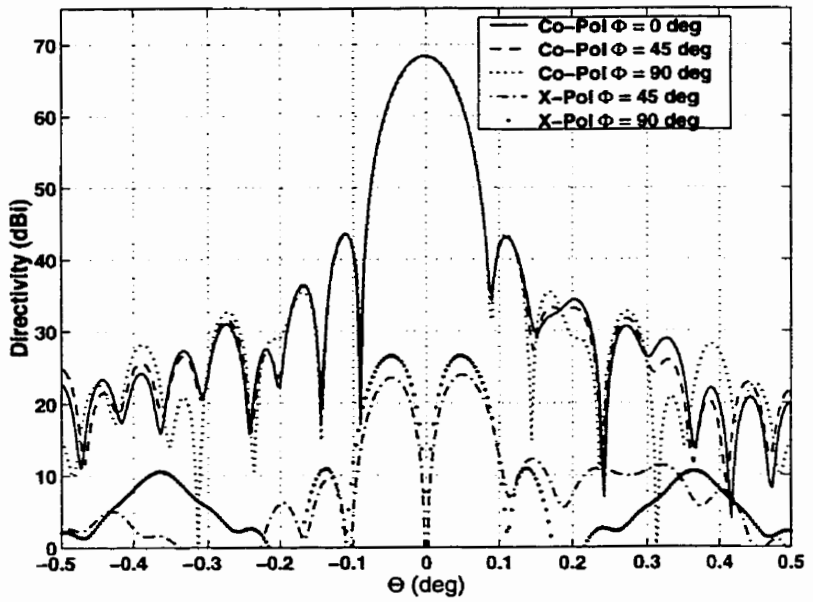

(b)

Figure 6.14: LAR radiation patterns a) $\theta_{ZA} = 30^o$, b) $\theta_{ZA} = 60^o$, f=3 GHz, D_L = 200cos(θ_{ZA}) m, R_o = 500 m, D_F = 25 m, f_F = 9 m, d_f = 0.23 m, D_S = 5/cos(θ_{ZA}) m, T_a = -15 dB, for LAR Min. X-Pol. & Max. directivity

6.4.7. Results for Scan Angles Less Than 7 Degree (Dual Offset LAR)

The parameters and results which have been shown up to now, are for scan angles between 7 to 60 degrees. For scan angles less than 7°, X_{FR} must be less than 100 m to satisfy the minimum cross-polarization condition of Eq.(6-26). However, it is observed from the previous results that the calculated cross-polarizations are far below -40 dB. This basically means for small scan angles, the maximum cross-polarization is in acceptable range even if Eq.(6-26) is not satisfied.

A new configuration is shown in Fig. 6.15 for θ_{ZA}= 0°(similar configuration can be designed for other scan angles less than 7°). In this figure all parameters are similar to Fig. 6.5 except for a new parameter θ_0 which is an offset angle. To design the system, X_{FR} is considered to be 130 m. The other parameters are as follow: $\beta = 10.0929°$, $\alpha = 0.3201°$, $e = 1.044$, $\theta_e = 0.2905°$, $\theta_0 = 4.6956°$, and $2c = 507.8592$ m. The LAR radiation patterns at 3 GHz are shown in Fig. 6.16. The maximum directivity is 74.75 dBi with the efficiency of 75.68%. The cross-polarization and the first sidelobe level are -45.25 and -22.25 dB respectively. A comparison between this result and those of the symmetric configuration reveals a considerable improvement in the LAR performance.

6.4.8. Dual Offset LAR Performance Over Its Operating Band

The performances of the system over the frequency band of 2 to 22 GHz, is also investigated. The idea of designing the Feed-Reflector to cover this frequency band was explained in chapter 4, which is to maintain the effective aperture area in wavelength constant which results in a fixed spot size. This can be done by utilization of different horns of different directivities. To investigate the performance of the LAR over its bandwidth, a

Feed-Reflector with a fixed diameter of 25 m, 9 m focal length and 0.23 m defocusing distance is assumed. The sub-reflector parameters and its orientation are similar to those for 3 GHz.

Directivities of the dual offset configuration for various scan angles over operating frequencies are plotted in Fig. 6.17a. Fig. 6.17b shows the efficiency of this system which indicates for almost all frequencies over 3 GHz they are more than 70%. Cross-polarization for the entire frequency band and for all scan angles (shown in Fig. 6.18a) are below -40 dB which is acceptable for most applications. The first sidelobe level (FSLL) of this configuration is depicted in Fig. 6.18b.

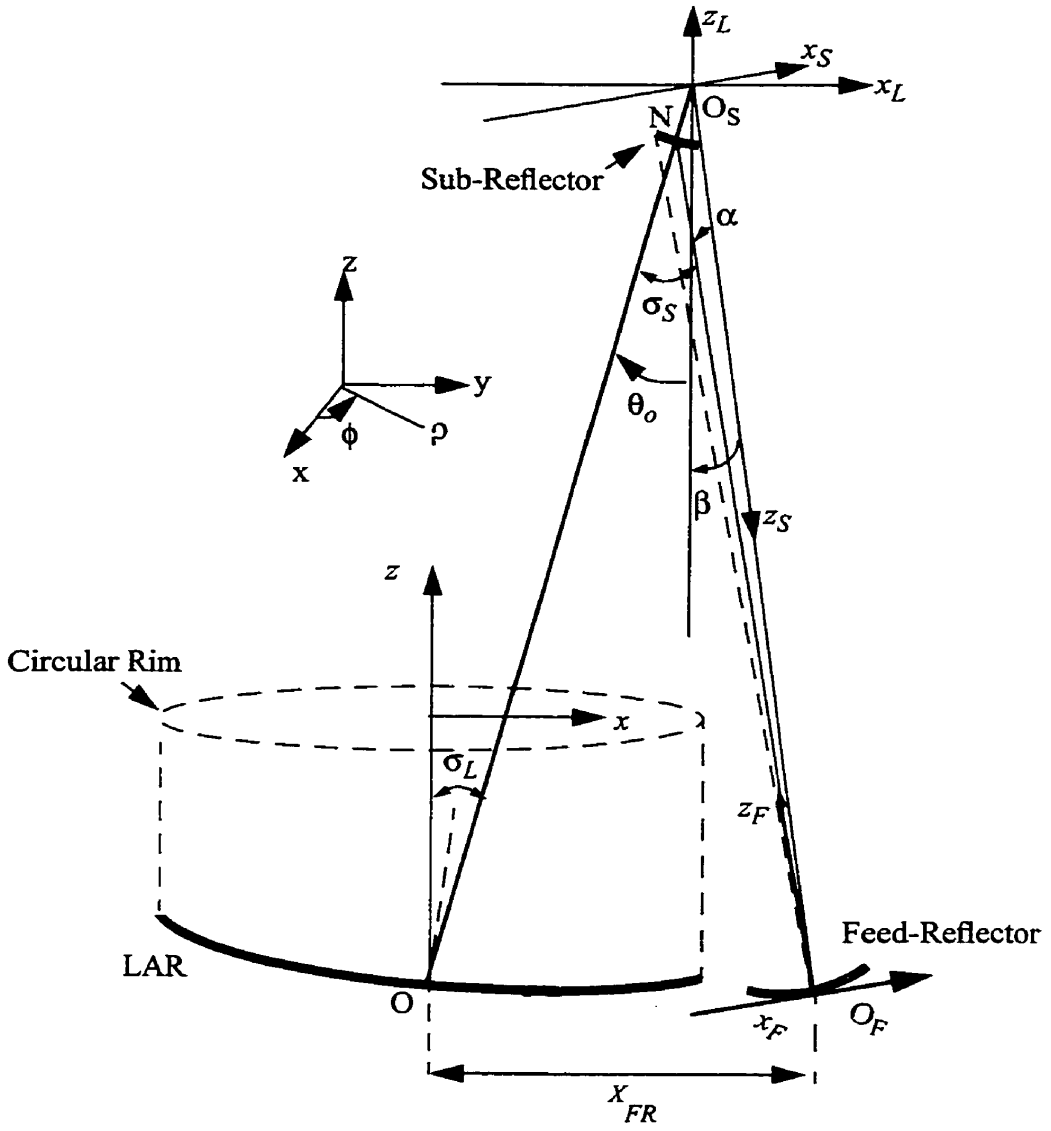

Figure 6.15: Dual offset reflector LAR configuration with $\theta_{ZA} = 0^o$

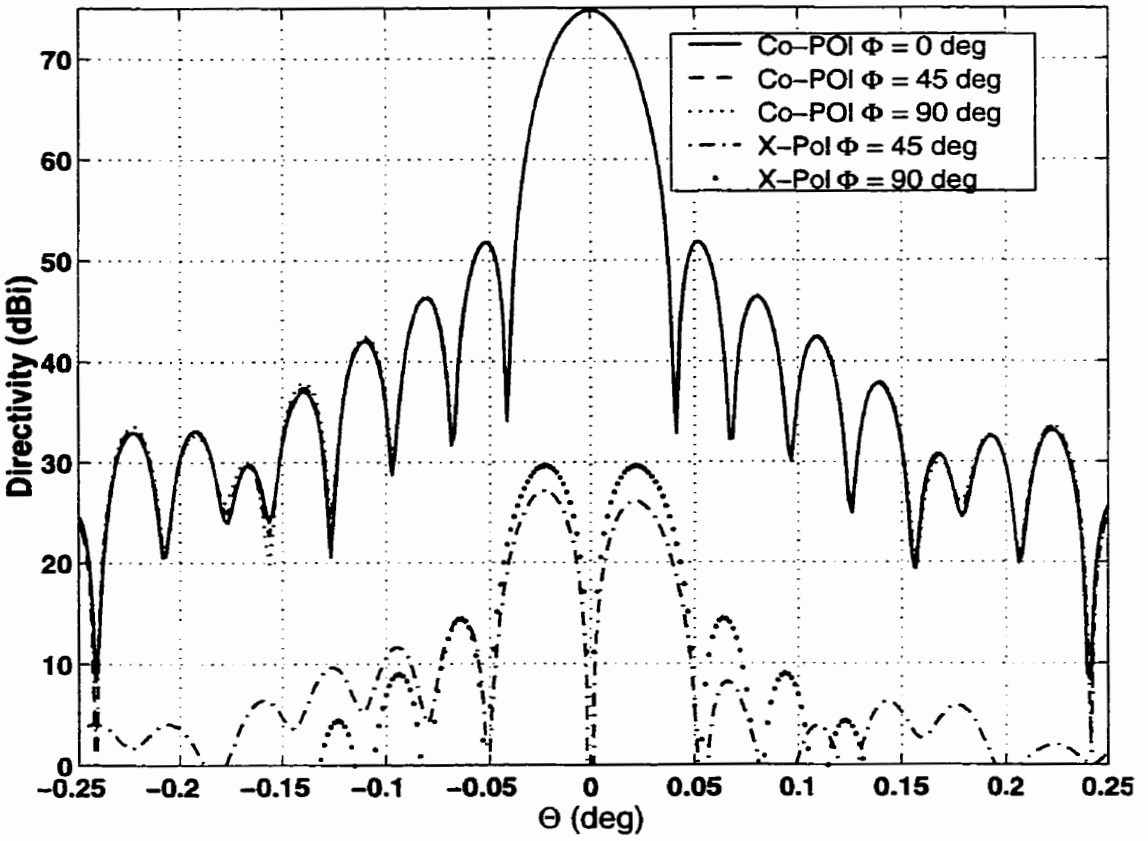

Figure 6.16: LAR radiation patterns for Dual offset reflector LAR configuration with $\theta_{ZA} = 0^{o}$*,(Fig. 6.15)* $f = 3$ *GHz,* $D_L = 200$ *m,* $R_o = 500$ *m,* $D_F = 25$ *m,* $f_F = 9$ *m,* $d_f = 0.23$ *m,* $D_S = 5$ *m,* $T_a = -15$ *dB*

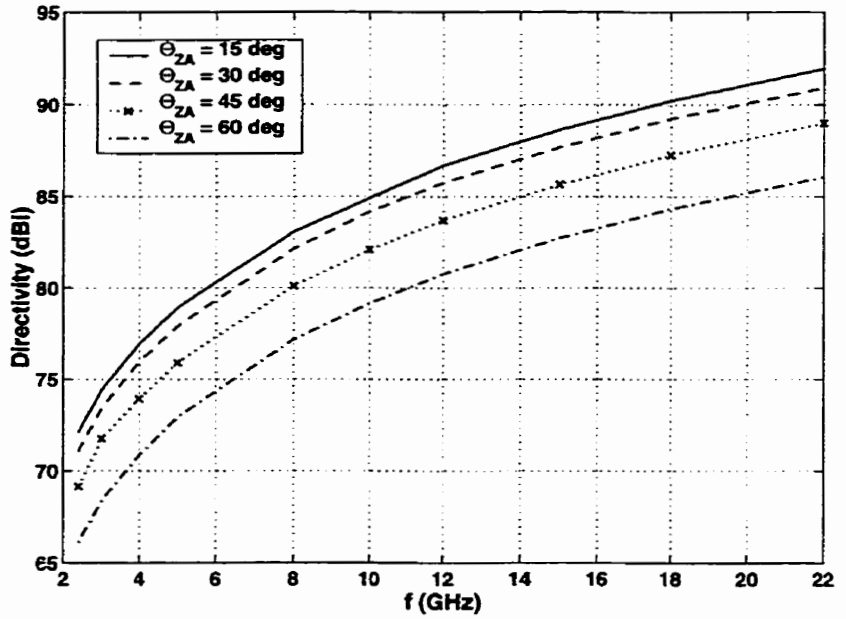

(a)

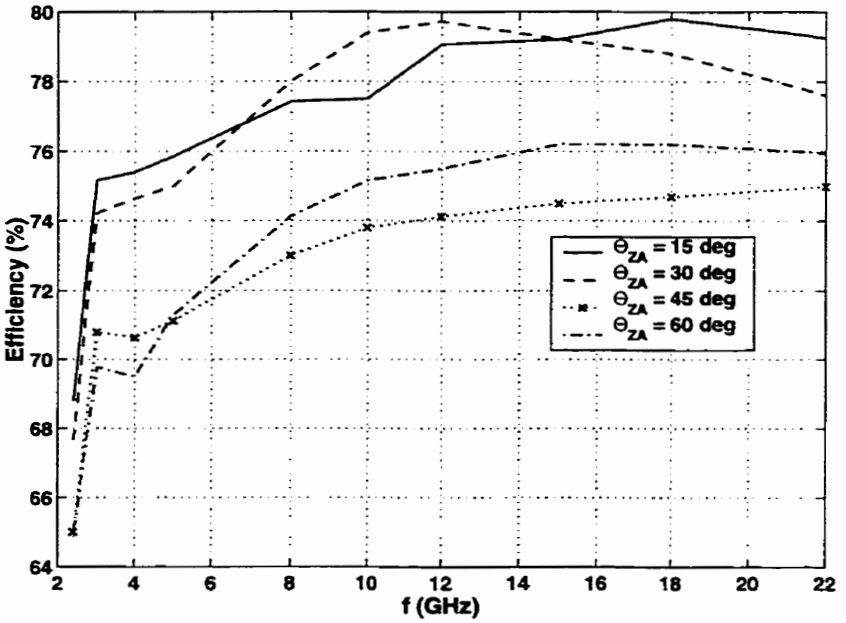

(b)

Figure 6.17: (a) directivity b) efficiency of the LAR vs. frequency for various scan angle for the configuration of Fig. 6.5, $D_L = 200\cos(\theta_{ZA})$ m, $R_o = 500$ m, $D_F = 25$ m, $f_F = 9$ m, $d_f = 0.23$ m, $D_S = 5/\cos(\theta_{ZA})$ m, $T_a = -15$ dB

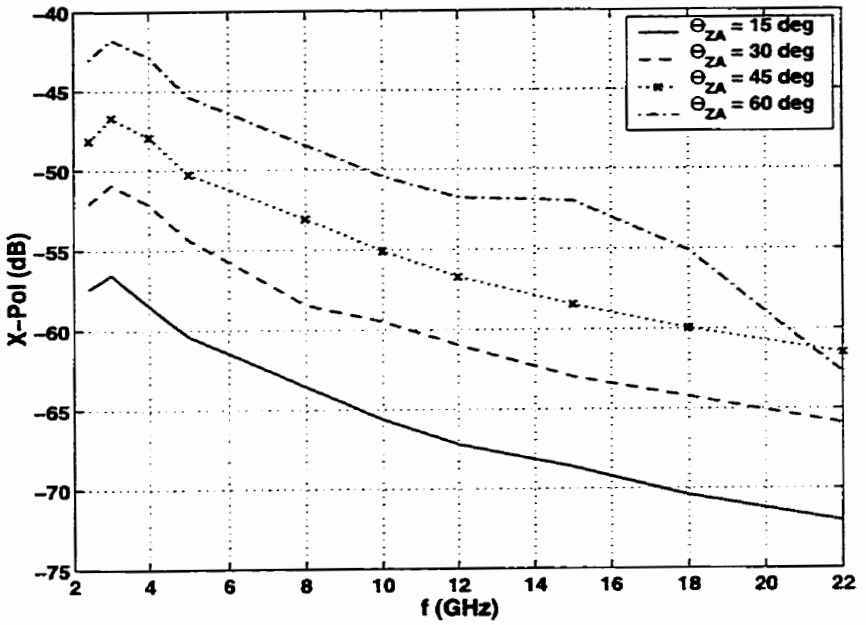

(a)

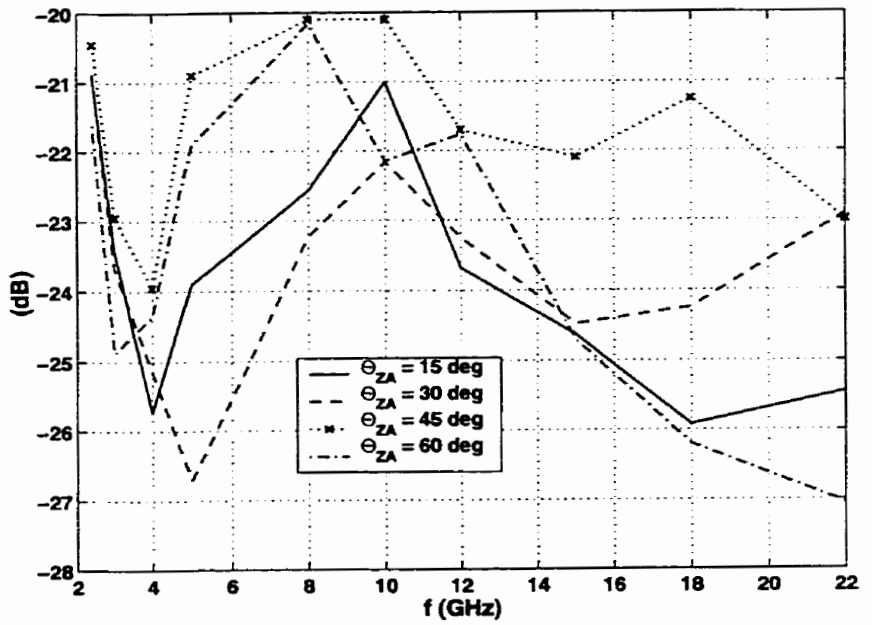

(b)

Figure 6.18: (a) cross-polarization (b) first sidelobe level of the LAR, for the configuration of Fig. 6.5, f =3 GHz, $D_L = 200\cos(\theta_{ZA})$ m, R_o = 500 m, D_F = 25 m, f_F = 9 m, d_f = 0.23 m, $D_S = 5/\cos(\theta_{ZA})$ m, T_a = -15 dB

6.5. Conclusion

An exact equation for the offset LAR surface was obtained in this chapter. Open Cassegrainian LAR was introduced and analysed. Although the structure was simple, the cross-polarization and blockage due to the Feed-Reflector were high, specially for large scan angles.

To overcome these difficulties, the concept of dual offset LAR with the Feed-Reflector was introduced. In that design the cross-polarization was eliminated by proper orientation of the sub-reflector. The parameters of the configuration were obtained by using generalized Gauss-Laguerre beam modes and a matrix representation of beam mode transformation factor. The efficiency of the system was maximized by the method introduced in chapter 5. The results obtained for this design indicated a considerable improvements in cross-polarization and gain. Also in that design the blockage effect was totally removed. Performances of the system over the LAR operating band were investigated which indicated satisfactory results.

Chapter 7

CONCLUSIONS

7.1. Summary

The concept of a Large Adaptive Reflector was described briefly in this thesis, and a novel feed system was designed. Various aspects of the LAR Cassegrainian system using the Feed-Reflector were investigated. The feed was based on the near field focusing properties of reflector antennas. The theory of this feed system was established by using the defocused paraboloid reflector characteristics and the aperture theory. By employing the concept of equal ray path theory, the sub-reflector profile was obtained. The effect of the feed horn defocusing distance and taper at the Feed-Reflector edge were studied. The field taper at the Feed-Reflector edge was found to be dependent on the wavelength and sub-reflector size. An approximated formula was developed to estimate the illuminated portion of the Feed-Reflector antenna (-15 dB taper at the edge).

To make it feasible for fabrication, a conventional hyperboloid sub-reflector was considered for the LAR symmetric configuration, which approximated the surface obtained by the equal path law. The effect of sub-reflector second focal point position, eccentricity, and size were investigated. A ray tracing was used for better understanding of the system performance. For the unshaped surfaces, a maximum efficiency of 75% was obtained with less than -65 dB cross polarization. The SLL is in the acceptable range.

The performance of the LAR was investigated over its operating band. It was

found that for a 5 meter sub-reflector and a 25 m Feed-Reflector, the LAR efficiency is more than 72% for the frequencies above 3.0 GHz. However, if the sub-reflector diameter is increased to 10 m this frequency reduces to 1 GHz.

Three shaping processes were conducted on the LAR Cassegrainian system for its symmetric configuration based on a diffraction synthesis technique, using Jacobi-Fourier series to represent the reflector surface. An efficiency of 78.5% was obtained by shaping all three reflectors.

The performance of the Feed-Reflector, for the LAR Cassegrainian system was investigated by means of the Gaussian-Laguerre beam mode analysis. The electric field at the aperture of the Feed-Reflector was calculated by physical optics and expanded in term of the Gaussian-Laguerre modes. The fractional power in the fundamental beam mode was about 99%, which indicated that it can be used as an efficient Gaussian beam launcher in quasi-optical systems. By utilizing the Gaussian beam analysis the hyperboloid sub-reflector parameters which maximize the LAR aperture efficiency were found. It was found that Gaussian beam optics provided a simple and elegant method of understanding the operation of the LAR with the Feed-Reflector system, and its optimization.

An exact equation for the offset LAR surface was obtained in this thesis. Open Cassegrainian LAR was introduced and analysed. Although the structure was simple, the cross-polarization and blockage due to the Feed-Reflector were high specially for large scan angles.

To overcome these difficulties associated with the symmetric configuration and

also open Cassegrainian system such as blockage and cross-polarization, the concept of a dual offset LAR with the Feed-Reflector was introduced. In that design the cross-polarization was eliminated by proper orientation of the sub-reflector. The parameters of the configuration were obtained by utilizing generalized Gauss-Laguerre beam modes and matrix representation of beam mode transformation factor. The efficiency of the system was maximized. The results obtained for the design indicated considerable improvements in cross-polarization and gain. Also in that design, the blockage effect due to the Feed-Reflector was totally removed. Performance of the offset system over the LAR operating band was investigated which indicated satisfactory results.

7.2. Future Work

Large Adaptive Reflector antenna using a Feed-Reflector is a new configuration. Further research can be pursued on experimental and theoretical aspects of such structures to develop novel designs capable of coping with future technological requirements for high gain applications.

The Feed-Reflector can be considered as a member of the feed family. Virtually, all the research that has been done in the areas of the feeds can be repeated for the Feed-Reflector. New research can be done on the performance and design of an offset Feed-Reflector. This research might help to reduce the movements of the Feed-Reflector in a dual offset configuration.

In this research it was assumed that the LAR surface is continuous. However, fur-

ther research can be done to investigate for the effect of the gaps between the panels. Also the following topics for investigation can be suggested:

a) Investigating the scanning performance of the LAR symmetric and offset configurations.

b) Deriving an equation for the equivalent parabola in the LAR Cassegrainian structure.

REFERENCES

[1] T. H. Legg, "A proposed large radio telescope of new design," *Astronomy & Astrophysics Suppl.*, vol. 130, pp. 369-379, 1998

[2] P. Mousavi, L. Shafai, and B. Veidt, "Primary study of feed option for Large Adaptive Reflector," Final report, Department of Electrical & Computer Engineering, University of Manitoba, Canada, Mar. 1999.

[3]A.F. Kay, "Near-field gain of aperture antennas," *IRE Trans. Antennas Propagat.*, vol. AP-8, pp. 586-593, Nov. 1960.

[4]J. W. Sherman, III, "Properties of focused apertures in the Fresnel region," *IRE Trans. Antennas Propagat.*, vol. AP-10, pp. 399-408, July. 1962.

[5]William J. Graham, "Analysis and synthesis of axial field patterns of focused apertures," *IEEE Trans. Antennas Propagat.*, vol. AP-31, No. 4, pp. 665-668, July 1983.

[6]A. Badawi, A. Sebak, and L. Shafai, "Array near field focusing," *1997 Conference on Communications, Power and Computing, Wescanex 97,* pp. 242-245, Winnipeg, May 22, 1997.

[7]D. K. Cheng, and S. T. Moseley, "On-axis defocus characteristics of the paraboloidal reflector," *IRE Trans. Antennas Propagat.*, vol. AP-3, pp. 214-216, Oct. 1955.

[8] D. K. Cheng, "On the simulation of Fraunhofer radiation patterns in the Fresnel region," *IRE Trans. Antennas Propagat.*, vol. AP-5, pp. 399-402, Oct. 1957.

[9] T. S. Chu, "A note on simulating Fraunhofer radiation patterns in the Fresnel region," *IEEE Trans. Antennas Propagat.*, vol. AP-19, pp. 691-692, Sept. 1971.

[10] L. Shafai, A. Kishk, and A. Sebak, "Near field focusing of aperture and reflector antennas," *1997 Conference on Communications, Power and Computing, Wescanex 97,* pp. 246-251, Winnipeg, May 22, 1997.

[11] P. Mousavi, L. Shafai, P. Dewdney, B. Veidt, "Application of the Large Adaptive Reflector (LAR) for deep space communication," *USNC/URSI Radio Science Meeting* Digest, pp. 180, Orlando, July, 1999.

[12] P. G. Ingerson, and W.V.T. Rusch, "Radiation from a paraboloid with an axially defocused feed," *IEEE Trans. Antennas Propagat.*, vol. AP-21, pp. 104-106, Jan. 1973.

[13]V. Galindo-Israel, and R. Mittra, "A new series representation for the radiation integral with application to reflector antennas," *IEEE Trans. Antennas Propagat.*, vol. AP-25, pp. 631-641, Sept. 1977.

[14] R. Mittra, Y. Rahmat-Samii, V. Galindo-Israel, and R. Norman, "An efficient technique for the computation of vector secondary patterns of the offset paraboloid reflector, "*IEEE Trans. Antennas Propagat.*, vol. AP-27, pp. 294-304, May 1979.

[15] Y. Rahmat-Samii, V. Galindo-Israel, "Shaped reflector antenna analysis using the Jacobi-Bessel series," *IEEE Trans. Antennas Propagat.*, vol. AP-28, No. 4, pp. 425-435, July 1980.

[16] A.A. Kishk, L. Shafai, "Different formulations for numerical solution of single and

multi-bodies of revolution with mixed boundary conditions, "*IEEE Trans. Antennas Propagat.* vol. AP-34, pp. 666-673, 1986.

[17] A.D. Olver, P. Clarricoats, A. Kishk, and L. Shafai, "Microwave horns and feeds," *IEE Proc.*, Peter Peregrinus, London, 1994.

[18] N.C. Albertsen, K. Pontoppidan, "Analysis of subreflector for dual reflector antennas," *IEE Proc,* 131H, pp. 205-213, June 1984.

[19] K. Pontoppidan, "Technical description of Grasp8", TICRA engineering consultants communication systems and antennas, July, 1999.

[20] A.W. Love, "Scale model development of a high efficiency dual polarized line feed for the Arecibo spherical reflector," *IEEE Trans. Antennas Propagat.* vol. AP-21, pp. 628-639, 1973.

[21] P-S. Kildal, "Study of element patterns and excitations of line feeds of the spherical reflector at Arecibo," *IEEE Trans. Antennas Propagat.* vol. AP-34, pp. 197-207, Sept. 1986.

[22] P-S. Kildal, L.A. Baker, and T. Hagfors, "The Arecibo upgrading: Electrical design and expected performance of the dual-reflector feed system," *IEEE Proc.* vol. 82, No. 5, pp. 714-724, May 1994.

[23] J.D. Kraus, "*Antennas*," McGraw-Hill International Edition, pp. 610-613, 1988

[24] C. Granet, G.L. James, and J. Pezzani, "A new dual-reflector feed system for the

Nancy radio telescope," *IEEE Trans. Antennas Propagat.* vol. AP-45, pp. 1366-1373, Sept. 1997.

[25] C. Scott, "Modern method of reflector antenna analysis and design," Nortwood, MA: Artech House, 1990.

[26].J.B. Keller, "Geometrical theory of diffraction," *J. Opt. Soc. Amer.*, vol. 52, no. 2, pp. 116-130, Feb. 1962.

[27] J.B. Keller, "Diffraction by an aperture," *J. Appl. Phys.*, vol. 28, pp. 426-444, Apr. 1957.

[28] D.S. Ahluwalia, R.M. Lewis, and J. Boersma, "Uniform asymptotic theory of diffraction by a plane screen," *SIAM J. Appl. Math.* vol. 16, pp. 783-807, 1968.

[29] S. W. Lee and G.A. Deschamps, "A uniform asymptotic theory of electromagnetics diffraction by a curved wedge," *IEEE Trans. Antennas Propagat.* vol. AP-24, pp. 25-34, Jan. 1976.

[30] R.G. Kouyoumjian and P. H. Pathak, "A uniform geometrical theory of diffraction of an edge in perfectly conducting surface," *Proc. IEEE*, vol. 62, pp. 1448-1461, Nov. 1974.

[31] P. Y. Ufimtsev, "Method of edge waves in the physical theory of diffraction," *Izd-Vo Sovyetskoye Radio*, pp. 1-243, 1962.

[32] M. Ando, "Radiation pattern analysis of reflector antennas," *Electron. Commun. in*

Japan, Part 1, vol. 68, no. 4, pp. 93-102, 1985.

[33] K. M. Mitzner, "Incremental length diffraction coefficient," Aircraft Division Northrop Corp., Tech. Rep. AFAl-TR-73-296, Apr. 1974.

[34] A. Michaeli, "Equivalent edge current for arbitrary aspects of observation," *IEEE Trans. Antennas Propagat.* vol. AP-32, pp. 252-258, Mar. 1984.

[35] E. F. Knott, "The relationship between Mitzner's ILDC, and Michaeli's equivalent current," *IEEE Trans. Antennas Propagat.* vol. AP-33, pp. 112-114, Jan. 1985.

[36] A. Michaeli, "Elimination of infinities in equivalent edge currents Part I: Fringe current components," *IEEE Trans. Antennas Propagat.* vol. AP-34, pp. 912-918, July. 1986.

[37] B.Y. Kinber, "On two-reflector antennas," *Radio Eng. Elec. Phys.*, pp. 914-921, June 1962.

[38] V. Galindo-Israel, "Design of dual-reflector antennas with arbitrary phase and amplitude distribution," *IEEE Trans. Antennas Propagat.* vol. AP-12, pp. 403-408, July. 1964.

[39] W. F. Williams, "High efficiency antenna reflector," *Microwave J.*, vol. 8, no. 7, pp. 79-82, July 1965.

[40] V. Galindo-Israel, R. Mittra, and A.G. Cha, "Aperture amplitude and phase control of offset dual reflectors," *IEEE Trans. Antennas Propagat.* vol. AP-27, pp. 154-164, Mar.

1979.

[41] V. Galindo-Israel, W. Imbriale, and R. Mittra, "On the theory of the synthesis of single and dual offset shaped reflector antennas," *IEEE Trans. Antennas Propagat.* vol. AP-35, pp. 887-896, Aug. 1987.

[42] V. Galindo-Israel, W. Imbriale, R. Mittra, and K. Shogen, "On the theory of the synthesis of offset dual-shaped reflectors - Case examples," *IEEE Trans. Antennas Propagt.* vol. AP-39, pp. 620-626, May 1991.

[43] J. O. Rubinos-Lopez, and A. Garcia-Pino, "A ray by ray algorithm for shaping dual-offset reflector antennas," *Microwave and Optical Technology Letters*, vol. 15, no. 1, pp. 20-26, May 1997.

[44] B. S. Westcott, F. A. Stevens, and F. Brickell, "GO synthesis of offset dual reflectors," *IEE Proc,* vol. 128H, pp. 11-18, Feb. 1981.

[45] B.S. Westcott, "Shaped reflector antenna design." London: Research Studies Press Ltd. 1983.

[46] S. Von Hoerner, "Minimum-noise maximum gain telescope and relaxation method for shaped asymetric surfaces," *IEEE Trans. Antennas Propagat.* vol. AP-26, pp. 464-471, May. 1978.

[47] J. J. Lee, L. I. Parad, and R. S. Chu, "A shaped offset-fed dual reflector antenna," *IEEE Trans. Antennas Propagat.* vol. AP-27, pp. 165-171, Mar. 1979.

[48] B. S. Westcott, F. Brickell, and I.C. Wolton, "Cross-polar control in far field synthesis of dual offset reflectors," *IEE Proc,* vol. 137 H, no.1, pp. 31-38, Feb. 1990.

[49] P-S. Kildal, "Synthesis of multi-reflector antennas by kinematic and dynamic ray tracing," *IEEE Trans. Antennas Propagat.* vol. AP-38, no. 10, pp. 1587-1599, Oct. 1990.

[50] K. Aoki, N. Miyahara, S. Makino, S. Urasaki, and T. Katagi, "Design method for offset shaped antenna with an elliptical aperture of low cross-polarization characteristics," *IEE Proc,* vol. 146H, pp. 60-64, Feb. 1999.

[51] G. Bjontegaard, and T. Pettersen, "An offset dual-reflector antenna shaped from near-field measurements of the feed horn: Theoretical calculations and measurements," *IEEE Trans. Antennas Propagat.* vol. AP-31, no. 6, pp. 973-977, Nov. 1983.

[52] B. S. Westcott, and F. Brickell, "Geometric-optics synthesis of dual-reflector antennas with distributed sources," *IEE Proc,* vol. 136 H, no.5, pp. 361-366, Oct. 1989.

[53] A. Ludwig, "Low sidelobe aperture distributions for blocked and unblocked circular apertures," *IEEE Trans. Antennas Propagat.* vol. AP-30, no. 5, pp. 973-977, Sept. 1982.

[54] D. W. Duan, Y. Rahmat-Samii, "A generalized three-parameter (3-P) aperture distribution for antenna applications," *IEEE Trans. Antennas Propagat.* vol. AP-40, no. 6, pp. 697-713, June. 1992.

[55] A. R. Cherrette, S. W. Lee, and R. J. Acosta, "A method for producing a shaped con-

tour radiation pattern using a single shaped reflector and a single feed," *IEEE Trans. Antennas Propagat.* vol. AP-37, no. 6, pp. 698-706, Nov. 1989.

[56] P. J. Wood, "Reflector antenna analysis and design," *IEE Electromagnetic Waves* Series 7, London: Peter Peregrinus Ltd. 1986.

[57] J. Bergmann, R. C. Brown, P. J. B. Clarricoats, and H. Zhou, "Synthesis of shaped-beam reflector antennas patterns," *IEE Proc,* vol. 135H, no. 1,pp. 48-53, Feb. 1988.

[58] Y. Rahmat-Samii, J. Mumford, "Reflector diffraction synthesis using global coefficient optimization techniques," *IEEE AP-S Intl. Symp.* pp. 1166-1169, 1989.

[59] D. W. Duan, and Y. Rahmat-Samii, "A generalized diffraction Synthesis technique for high performance reflector antennas," *IEEE Trans. Antennas Propagat.* vol. AP-43, no. 1, pp. 27-40, Jan. 1995.

[60] D. W. Duan, and Y. Rahmat-Samii, "Reflector antennas with superquadric aperture boundaries," *IEEE Trans. Antennas Propagat.* vol. AP-41, no. 8, pp. 1164-1167, Aug. 1993.

[61] R. A. Hoferer, and Y. Rahmat-Samii, "A GO-sub-reflector implementation methodology using Fourier-Jacobi surface expansion," *IEEE AP-S Intl. Symp.* 1999, pp. 2328-2331.

[62] R. C. Hansen, Ed. "Microwave scanning antennas," vol. I. NewYork, Academic, 1964.

[63] H. Bryant, "*Heinrich Hertz*," pp. 40-43, NewYork: IEEE 1988.

[64] J. C. Bose, "Collected Physical Papers," London: Longmans, Green, 1927.

[65] A. G. Fox, and T. Li, "Resonator modes in a maser interferometer," *Bell Syst. Tech. J.*, vol. 40, pp. 453-488, Mar. 1961.

[66] H. Kogelnik, "Equivalence relations among spherical mirror optical resonators," *Bell Syst. Tech. J.*, vol. 43, pp. 2873-2886, Nov. 1964.

[67] H. Kogelnik, and T. Li, "Laser beams and resonators," *Proc. IEEE*, vol. 54, pp. 1312-1329, Oct. 1966.

[68] G. Goubau, and F. Schwering, "On the Guided propagation of electromagnetic wave beams," *IRE Trans. Antennas Propagat.*, vol. 9, pp.248-261, May 1961.

[69] B. Mac A. Thomas, "Design of corrugated conical horns," *IEEE Trans. Antennas Propagat.* vol. AP-26, pp. 367-372, Mar. 1978.

[70] C. Aubry, and D. Bitter, "Radiation pattern of a corrugated conical horn in terms of Laguerre Gaussian functions," *Electron. Lett.*, vol. 11, pp. 154-156, 1975.

[71] R. J. Wylde, "Millimetre-wave Gaussian beam-mode optics and corrugated feed horns," *IEE Proc.* vol. 131H, no. 1,pp. 258-262, Aug. 1984.

[72] T. Shen, Z. Sun, and W. Dou, "The hexagonal horn as an efficient Gaussian beam launcher," *IEEE Trans. Antennas Propagat.* vol. AP-45, pp. 1173-1178, Jul. 1997.

[73] A.W. Rudge, K. Milne, A.D. Olver, and P. Knight, "The handbook of antenna design Vol. 1," *IEE Electromagnetic Waves series*, Peter Peregrinus, 1982.

[74] J. S. Cook, E.M. Elam, "The open Cassegrain antenna," *Bell Telephone Syst. Tech. Publ.*, Monograph 5051, 1961.

[75] T. S. Chu, and R. H. Turrin, "Depolarization properties of offset reflector antennas," *IEEE Trans. Antennas Propagat.* vol. AP-21, pp. 339-345, May. 1964.

[76] V. Jamnejad-Dailamani, and Y. Rahmat-Samii, "Some important geometrical features of conical-section-generated offset reflector antennas," *IEEE Trans. Antennas Propagat.* vol. AP-28, pp. 952-957, Nov. 1980.

[77] R. Graham, "The polarization characteristics of offset Cassegrainian aerials," *Proc. IEE Conf. on Radar Present and Future*, pp. 23-25, 1973.

[78] H. Tanaka, M. Mizusawa, "Elimination of cross-polarization in offset dual-reflector antennas," *Trans. Inst. Electron. Commun. Eng. Japan*, vol. 58-B, no. 12, pp. 643-650, Dec. 1975.

[79] Y. Mizugutch, M. Akagawa, and H. Yokoi, "Offset dual reflector antennas," *IEEE AP-S Intl. Symp. Dig.* pp. 2-5, Amherst, MA, Oct. 1976.

[80] C. Dragone, "Offset multi reflector antennas with perfect pattern symmetry and polarization discrimination," *Bell Syst. Tech. J.*, vol. 57, no. 7, pp. 2663-2684, Sept. 1978.

[81] R. A. Shore, "A simple derivation of the basic design equation for offset dual reflector

antennas with rotational symmetry and zero cross-polarization," *IEEE Trans. Antennas Propagat.* vol. AP-33, pp. 114-116, Jan. 1985.

[82] K. W. Brown, and A. Prata, Jr., "A design procedure for classical offset dual reflector antennas with circular apertures," *IEEE Trans. Antennas Propagat.* vol. AP-42, pp. 1145-1152, Aug. 1994.

[83] W. V. T. Rusch, A. Prata, Jr. Y. Rahmat-Samii, and R. Shore, "Derivation and application of equivalent paraboloid for classical offset Cassegrain and Gregorian Antennas," *IEEE Trans. Antennas Propagat.* vol. AP-38, pp. 1141-1149, Aug. 1990.

[84] S. Sliver, "Microwave antennas theory and design," M.I.T. Rad. Lab. Ser. vol. 12, McGraw-Hill Book Co., Inc., New York, N.Y. ch. 6; 1949.

[85] H.C. Minnett, and B. MacA, "Field in image space of symmetrical focusing reflectors,"*Proc. Inst. Elec. Eng.*, vol. 115, pp. 1419-1430, 1968.

[86] F. S. Holt, and E. L. Bouche, "A Gregorian corrector for spherical reflectors," *IEEE Trans. Antennas Propagat.* vol. AP-12, pp. 44-47, Jan. 1964.

[87] B. M. Thomas, "Cross polarization characteristics of axially symmetric reflectors," *Electron. Lett.* vol. 12, pp. 218-219, Apr. 1976.

[88] P. Mousavi, L. Shafai, P. Dewdney, and B. Veidt, "Feed-Reflector design for large adaptive reflector antenna," *IEEE Trans. Antennas Propagat.* Submitted.

[89] P. Mousavi, L. Shafai, P. Dewdney, and B. Veidt, "Large adaptive reflector (LAR) fed

by a paraboloid Feed-Reflector," *Millennium Conference on Antenna & Propagation*, pp. 547, Davos, April 2000.

[90] P. Mousavi, L. Shafai, P. Dewdney, and B. Veidt, "Feed-Reflector system for large adaptive reflector Cassegrain configuration," *IEEE AP-S. Int. Symp. Digest.*, pp. 1910-1913, Salt Lake City, Jul. 2000.

[91] D.W. Duan, and Y. Rahmat-Samii, "Reflector / Feed (s) synthesis challenges for satellite contour beam applications," *IEEE AP-S Intl. Symp.* 1992, pp. 297-300.

[92] Y. Rahmat-Samii et al., 'Computation of Fresnel and Fraunhofer fields of planar aperture and reflector antenna by Jacobi-Bessel series-A review," *Electromagnetics*, vol. 1, no. 2, pp. 155-185, Apr. June, 1981.

[93] G. Szego, "Orthogonal polynomials," American Mathematical Society, 1959.

[94] R. L. Haupt, "An introduction to genetic algorithms for electromagnetics," *IEEE Trans. Antennas Propagation Magazine,* 37, 2, pp. 7-15, Apr. 1995.

[95] P. Mousavi, L. Shafai, P. Dewdney, and B. Veidt, "Characteristics of the large adaptive reflector antenna fed by a paraboloid reflector," *Int. Symp. on Antennas & Propagation, ISAP*, Accepted, Fukuoka, Japan Aug. 2000.

[96] P. Mousavi, L. Shafai, P. Dewdney, and B. Veidt, "Shaping large adaptive reflector Cassegrain configuration using Feed-Reflector," *Symp. on Antenna Tech. & Appl. Electromagnetics, ANTEM*, pp. 291-294, Winnipeg, Canada Jul. 2000.

[97] M. Abramowitz, and I.E. Stegun, "Handbook of mathematical function with formulas, graphs, and mathematical tables", *U.S. Department of Commerce,* June 1964.

[98] T. S. Chu, "An imaging beam waveguide feed," *IEEE Trans. Antennas Propagat.*, vol. Ap-31, pp. 614-619, 1983.

[99] R. E. Collin, "Antennas and Radio wave Propagation", McGraw-Hill, New York 1985, Chapter 4.

[100] Takashi, Kitsuregawa, "Advance technology in satellite communication antennas: electrical and mechanical design," Artech House, Norwood, MA, 1990.

[101] S. Betsudan, T. Katagi, "Design method of four-reflector type beam waveguide feeds," *Electronics and Communications in Japan*, Part 1, vol. 68, No. 1, pp. 109-107, 1985.

[102] M. J. Gans, R. A. Semplak, "Some far-field studies of an offset launcher," *Bell Syst. Tech. J.*, vol. 54, pp. 1319-1340, Sept., 1975.

[103] M. J. Gans, "Cross Polarization in reflector-type beam waveguide and antennas," *Bell Syst. Tech. J.*, vol. 55, pp. 289-316, Mar., 1976.

[104] P. Dewdney, "The large adaptive reflector (LAR), Geometry of the reflector," NRC, DRAO, report, June, 1998

APPENDIX I

Modified Jacobi Polynomials

This material is from reference [59] and included as an aid for understanding the relationship (4-5)

Definition of the modified Jacobi polynomials, and formulas that are convenient for numerical evaluation of the derivatives $dF_m^n(t)/dt$ are present in this appendix.

The modified Jacobi polynomials, $F_m^n(t)$, are defined as [92]

$$F_m^n(t) = \sqrt{2(n+2m+1)} \bullet P_m^{(n,0)}(1-2t^2) \bullet t^n \qquad 0 \le t \le 1 \tag{I-1}$$

where $P_m^{(n,0)}$ is a Jacobi polynomial. The Jacobi polynomials, are generally denoted by $P_m^{(\alpha,\beta)}(x)$, are defined as [93]

$$(1-x)^{\alpha}(1+x)^{\beta}P_n^{(\alpha,\beta)}(x) = \frac{(-1)^n}{2^n \cdot n!}\left(\frac{d}{dx}\right)^n[(1-x)^{n+\alpha}(1+x)^{n+\beta}] \tag{I-2}$$

They can be calculated most efficiently using the recurrence relations

$$P_0^{(\alpha,\beta)}(x) = 1 \tag{I-3}$$

$$P_1^{(\alpha,\beta)}(x) = \frac{1}{2}(\alpha+\beta+2)x + \frac{1}{2}(\alpha-\beta) \tag{I-4}$$

$$\begin{aligned} &2n(n+\alpha+\beta)(2n+\alpha+\beta-2)P_n^{(\alpha,\beta)}(x) \\ &= (2n+\alpha+\beta-1)[(2n+\alpha+\beta)(2n+\alpha+\beta-2)x + (\alpha^2-\beta^2)] \\ &\quad P_{n-1}^{(\alpha,\beta)}(x) - 2(n+\alpha-1)(n+\beta-1)\times(2n+\alpha+\beta)P_{n-2}^{(\alpha,\beta)}(x) \end{aligned} \tag{I-5}$$

$n = 2, 3, 4, \ldots$

In the diffraction analysis of reflector antennas, one typically has to find the derivatives such as

$$r'_t = \left(\frac{\partial}{\partial t}x', \frac{\partial}{\partial t}y', \frac{\partial}{\partial t}z'\right) \tag{I-6}$$

For reflector that is represented by the modified Jacobi polynomials $F_m^n(t)$ as shown in Eq.(4-5), the derivative $dF_m^n(t)/dt$ must be calculated. For this purpose, we use the recurrence relation for the derivatives of the Jacobi polynomials [93]to obtain that of the modified Jacobi polynomials

$$\frac{dF_m^n(t)}{dt} = \frac{n}{t}F_m^n(t) - \frac{m}{n+2m}\cdot\frac{1}{t(1-t^2)}$$
$$\left\{[n-(n+2m)(1-2t^2)]\cdot F_m^n(t) + 2(n+m)\sqrt{\frac{n+2m+1}{n+2m-1}}F_{m-1}^n(t)\right\} \tag{I-7}$$

Equation (I-7) is not convenient for the computer program implementation because of the apparent singularities at $t = 0$, $t = \pm 1$, $n=m=0$, and $n+2m-1=0$. To overcome this difficulty, a study on Eq.(I-7) for various combinations of the indices m and n is conducted. As a result, it is found that the apparent singularities in Eq.(I-7) can be avoided using the formulas (I-8)-(I-11). These formulas consist of an algorithm which can be directly transferred into the computer code.

- When $n=0$ and $m=0$,

$$\frac{dF_m^n(t)}{dt} = 0 \tag{I-8}$$

- When $n = 0$ and $m = 1,2,3,\ldots$,

$$\frac{dF_m^n(t)}{dt} = -\sqrt{8(2m+1)} \cdot (m+1) \cdot t \cdot P_{m-1}^{(n+1,1)}(1-2t^2) \tag{I-9}$$

- When $n = 1,2,3,\ldots$ and $m = 0$,

$$\frac{dF_m^n(t)}{dt} = \sqrt{2(2n+1)} \cdot n \cdot t^{n-1} \tag{I-10}$$

- When $n = 1,2,3,\ldots$ and $m = 1,2,3,\ldots$,

$$\frac{dF_m^n(t)}{dt} = \sqrt{2(n+2m+1)} \cdot t^{n-1} \cdot (-2t^2 \cdot (n+m+1)P_{m-1}^{(n+1,1)}(1-2t^2) - (-n)P_m^{(n,0)}(1-2t^2)] \tag{I-11}$$

APPENDIX II

Offset LAR Surface Equation

This appendix provides a detailed investigation of paraboloid surface families that arise by rotating and translating the paraboloid and keeping a single point on the ground fixed, i.e. common to all paraboloids. They were investigated in [104] and shown to satisfy Eq. (6-1), shown later in Eq. (II-11)

Fig. II.1 shows a cut through the x-z plane of Fig. 6.1, containing the focus and the centre of the LAR, shown in configuration where R_o is held constant during the scan. Only, a small part of the paraboloid near the origin in Fig. II.1 is actually constructed as a physical reflector. The focal length and the degree of offset from the vertex of the paraboloid vary with scan angle. Unlike other radio telescopes where the geometry either is fixed or may be adjusted slightly, the fundamental parameters of the paraboloid change continuously as telescope scans.

The reasons for the use of parabolic surface are:

- rays parallel to the axis of the paraboloid are reflected to the focus
- the ray path distances from any wavefront plane to the focus are equal

Fig. II.2 shows example of rays for several scan angles, i.e. scanned beams.

The equation for the LAR paraboloid surface, in a coordinate system with its vertex at the origin and its focus on the z_r-axis along the incoming ray, i.e. the reflector beam, is simply

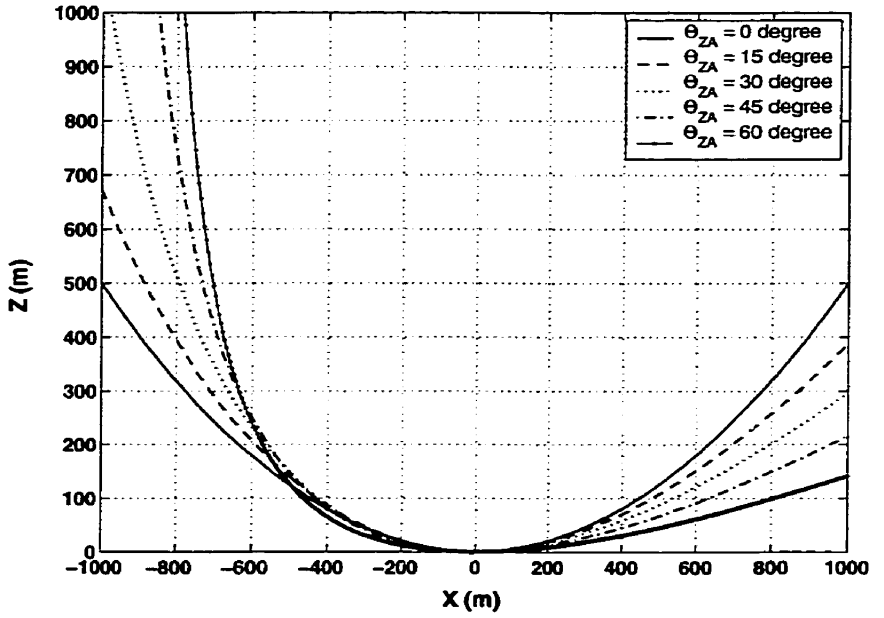

Figure II.1: Different rotated-translated paraboloid surfaces for various rotation angles θ_{ZA}*.[104]*

$$z_r = \frac{x_r^2 + y_r^2}{4f_L} \tag{II-1}$$

where f_L is the LAR focal length.

However, this equation is not appropriate for describing the LAR. A more useful equation, based in the coordinate system of Fig. 6.1, can be derived from Eq.(II-1) by the transformation of coordinate systems displayed in Fig. II.3.

Fig. II.3 shows a cut in x_r-z_r plane of Eq.(II-1), which has been constructed to contain the focus, the centre of the LAR reflector (x_0, z_0), and the paraboloid vertex at x_r-z_r origin O_r. In this plane, equation of the parabola is

$$z_r = \frac{x_r^2}{4f_L} \tag{II-2}$$

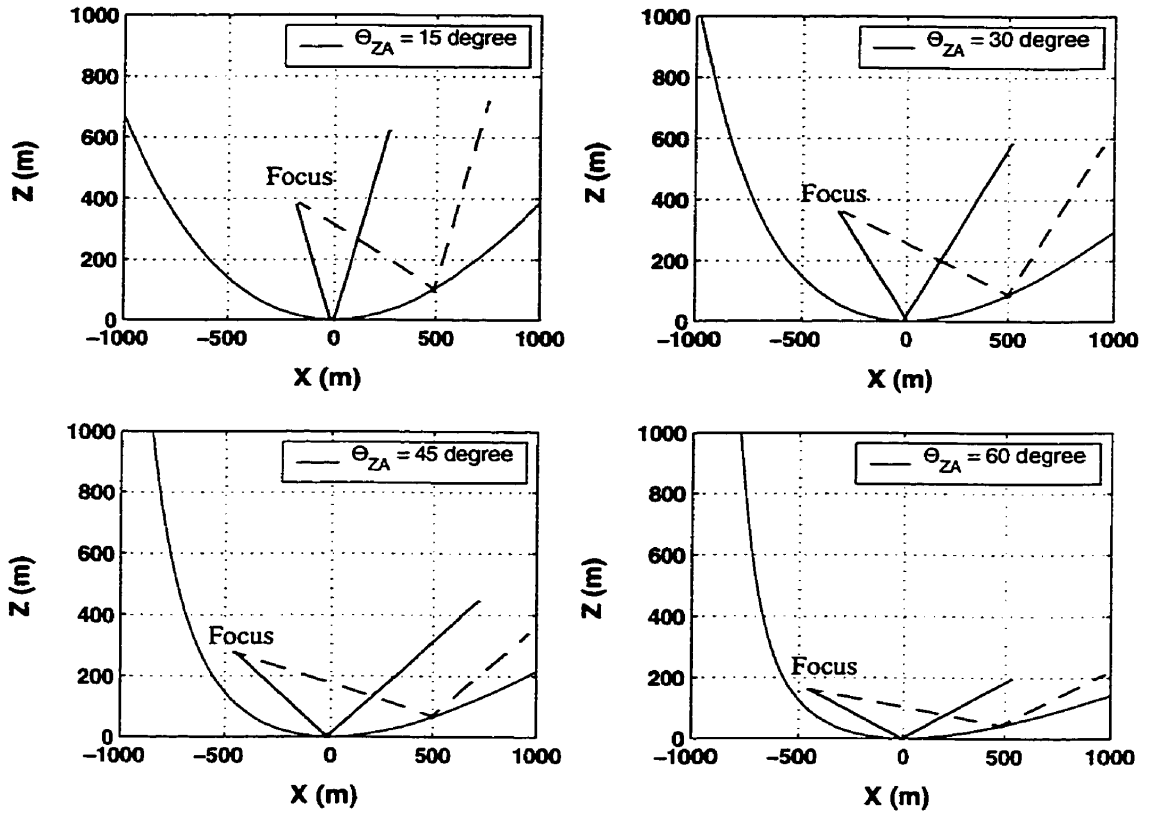

Figure II.2: Another view of the reflector geometry showing off-centre rays paths 500 m apart to show the whole profile of the rotated-translated reflector, converging at the focus.

Referring to Fig. II.3, the local vertical, represented as the z-axis, is normal to the reflector, and the tangent line at (x_0, z_0) is at the angle of θ_{ZA} to the x_r-axis, which is also the angle of the focus, as viewed from the reflector centred (x_0, z_0). The slope of parabolic surface, tangent at (x_0, z_0) is

$$\frac{dz_r}{dx_r} = \frac{x_o}{2f_L} = \tan\theta_{ZA} \tag{II-3}$$

Substituting Eq.(II-3) into Eq.(II-2), evaluated at (x_0, z_0), produces

$$z_0 = f_L tan^2\theta_{ZA} \tag{II-4}$$

Another relation can be derived from Fig. II.3. The sum of the distances from the

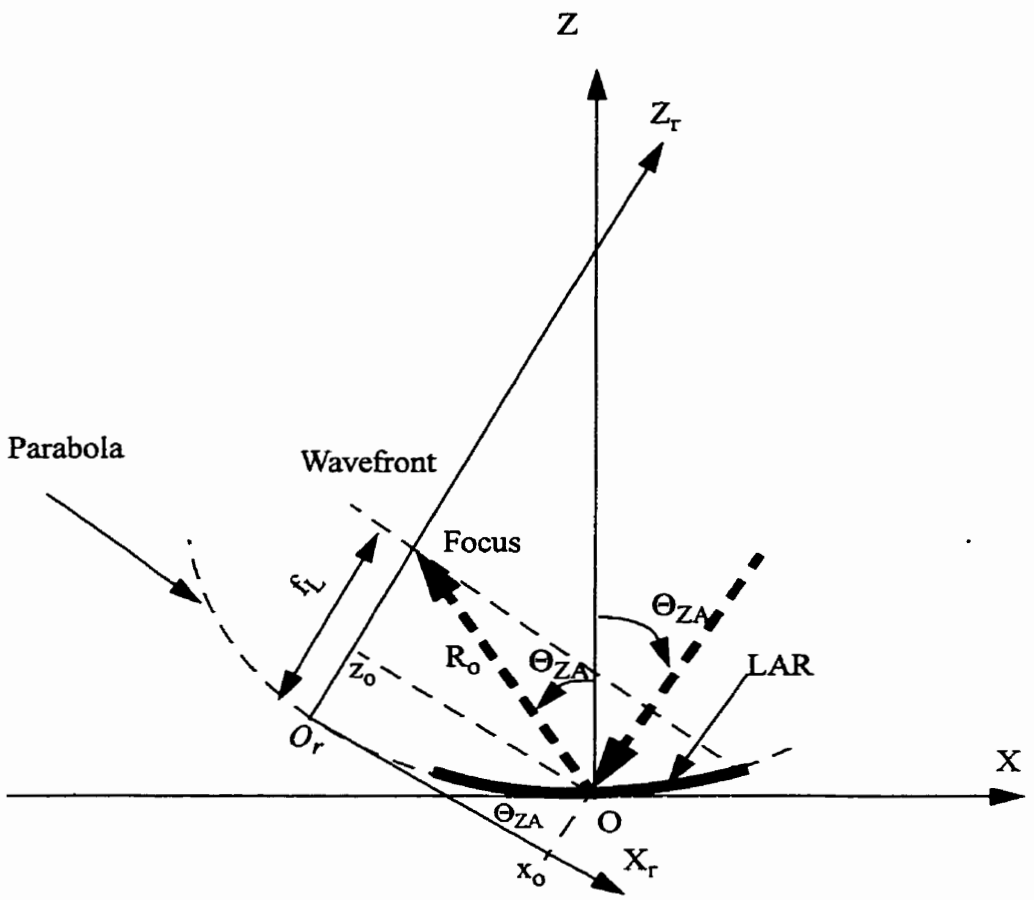

Figure II.3: A geometry to illustrate the transformation of the coordinates for the offset LAR surface

wavefront line shown in this figure to the focus must be constant for all rays parallel to the z_r-axis, including the one reflected at (x_0, z_0). Thus

$$R_o + (f_L - z_0) = 2f_L \tag{II-5}$$

Combining Eqs.(II-4) and (II-5) yields

$$R_o = f_L(1 + tan^2\theta_{ZA}) \tag{II-6}$$

Eq.(II-6) relates R_o to the focal length of the paraboloid.

The required coordinate transformation steps are

- translate the coordinates to (x_0, z_0)
- rotate them by θ_{ZA} in the x_r-z_r plane

The intermediate coordinates are (x_t, z_t), and the final coordinates are (x, z). For the translation step the transformation equations are

$$\begin{aligned} x_t &= x_r - x_0 \\ z_t &= z_r - z_0 \end{aligned} \tag{II-7}$$

Substituting these into Eq.(II-2) yields the equation for the parabola in (x_t, z_t) system[104]:

$$z_t = \frac{1}{4f_L}(x_t^2 + 4x_t f_L tan^2\theta_{ZA}) \tag{II-8}$$

For the rotation step, the transformation matrix is:

$$\begin{bmatrix} x_t \\ z_t \end{bmatrix} = \begin{bmatrix} \cos\theta_{ZA} & -\sin\theta_{ZA} \\ \sin\theta_{ZA} & \cos\theta_{ZA} \end{bmatrix} \begin{bmatrix} x \\ z \end{bmatrix} \tag{II-9}$$

Substituting Eq.(II-9) into Eq.(II-8), and using Eq.(II-6) for f_L, after some simplification gives

$$\tan(\theta_{ZA})\sin(\theta_{ZA})z^2 - 4R_o\left(1 + \frac{x}{2R_o}\sin(\theta_{ZA})\right)z + x^2\cos(\theta_{ZA}) = 0 \tag{II-10}$$

which does not contain f_L. If the same analysis is used for the three dimensional case, an analogous 3-D equation can be derived, with a y- term[104]

$$\tan(\theta_{ZA})\sin(\theta_{ZA})z^2 - 4R_o\left(1 + \frac{x}{2R}\sin(\theta_{ZA})\right)z + x^2\cos(\theta_{ZA}) + \frac{y^2}{\cos(\theta_{ZA})} = 0 \tag{II-11}$$

Fig. II.4 shows 3- dimensional views of the reflector surface for various scan (zenith) angles.

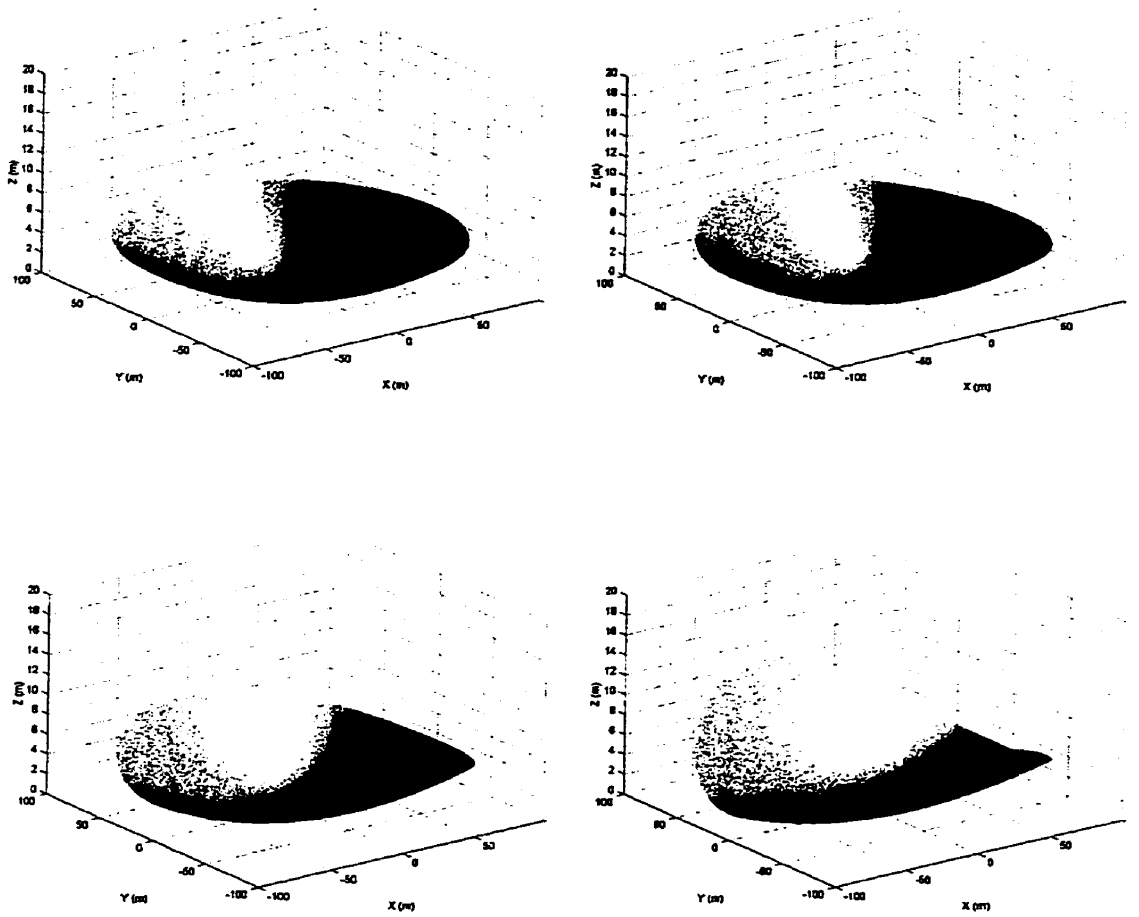

Figure II.4: Three dimensional views of the LAR surface. They are all calculated for R_o = 500 m and D = 200 m a) Top left: Θ_{ZA} = 15 deg. b) Top right: Θ_{ZA} = 30 deg. c) Bottom left: Θ_{ZA} = 45 deg. d) Bottom right: Θ_{ZA} = 60 deg.

APPENDIX III

Aperture Field Decomposition

This material is from reference [102] and included as an aid for understanding the relationships (6-8) and (6-9).

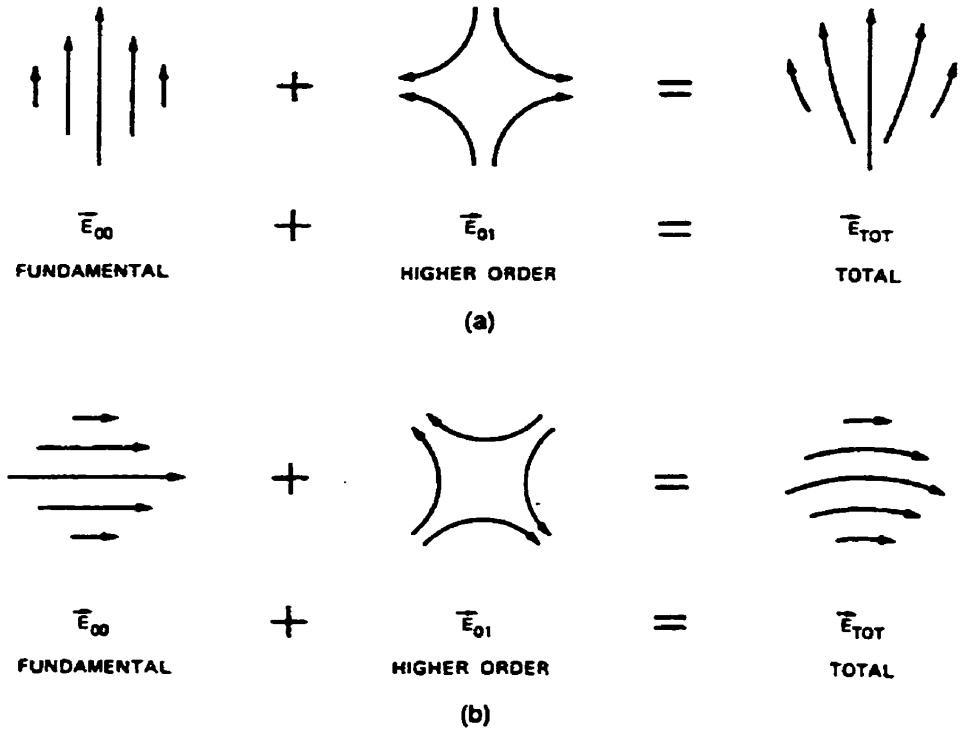

Figure III.1: Two mode decomposition of aperture field (looking opposite to direction of propagation) a) Feed horn vertically polarized b) Feed horn horizontally polarized

APPENDIX IV

Beam Mode Transformation Factors

This material is from reference [103] and included as an aid for understanding the relationships of section 6.4.3.

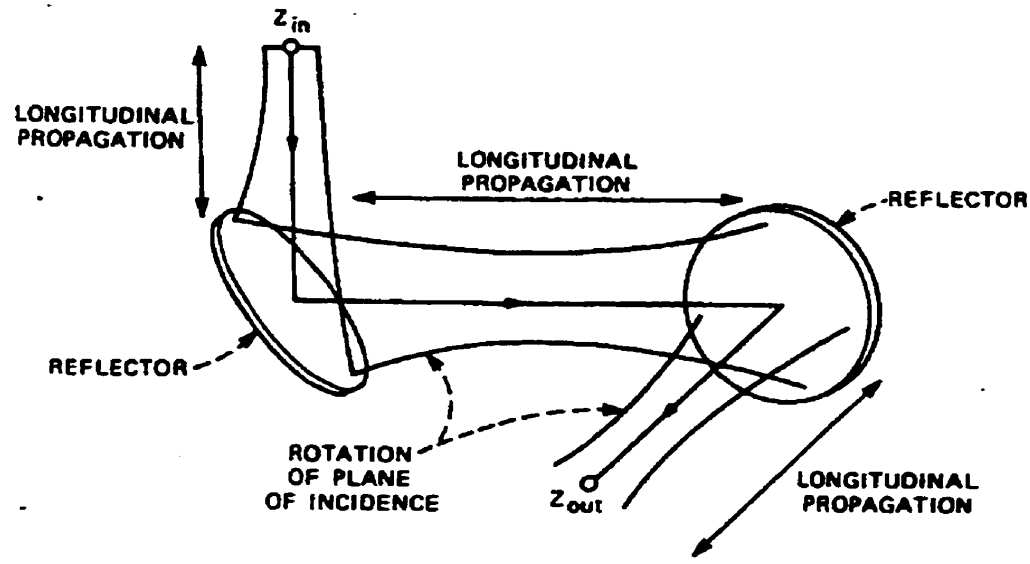

Figure IV.1: Factors influencing cross polarization in a reflector-type beam system.

By using the cross-polarization formulas and the mode definitions of section 6.4.2., and the conservation of power, the matrix elements applying when a fundamental mode is incident are easily determined:

$$T_{11} = \sqrt{1-\gamma^2} \qquad T_{13} = -\gamma \qquad T_{22} = -\sqrt{1-\gamma^2} \qquad T_{24} = \gamma$$
$$T_{12} = T_{21} = T_{14} = T_{23} = 0 \qquad \text{(IV-1)}$$

where γ is given in Eq. (6-10). Note that, for reflectors concave or convex in direction perpendicular to the plane of incidence, γ is positive or negative, respectively.

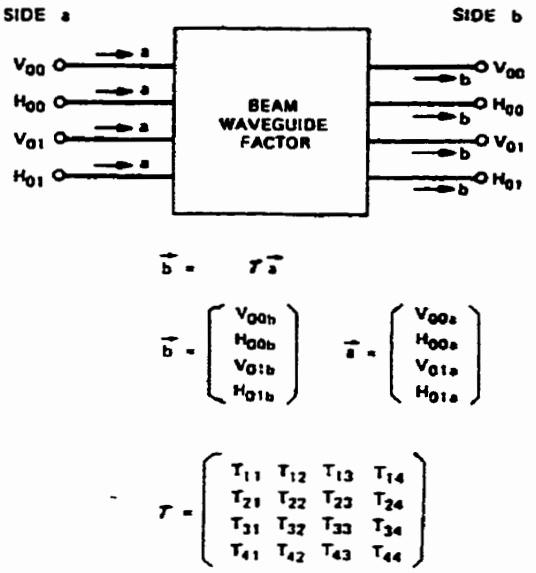

Figure IV.2: The beam waveguide factor as a reflectionless eight port.

Since the complex conjugate electric field satisfies Maxwell's equations and the boundary conditions on a perfect conductor (time reversal symmetry), the remaining matrix elements follow readily from the above real matrix elements of Eq. (IV-1):

$$T_{33} = -\sqrt{1-\gamma^2} \qquad T_{31} = -\gamma \qquad T_{44} = \sqrt{1-\gamma^2} \qquad T_{42} = \gamma$$
$$T_{41} = T_{32} = T_{43} = T_{34} = 0 \tag{IV-2}$$

Note that V modes do not couple to H mode during the reflection from a curved reflector.

$$T_{ref} = \begin{bmatrix} \sqrt{1-\gamma^2} & 0 & -\gamma & 0 \\ 0 & -\sqrt{1-\gamma^2} & 0 & \gamma \\ -\gamma & 0 & -\sqrt{1-\gamma^2} & 0 \\ 0 & \gamma & 0 & \sqrt{1-\gamma^2} \end{bmatrix} \tag{IV-3}$$

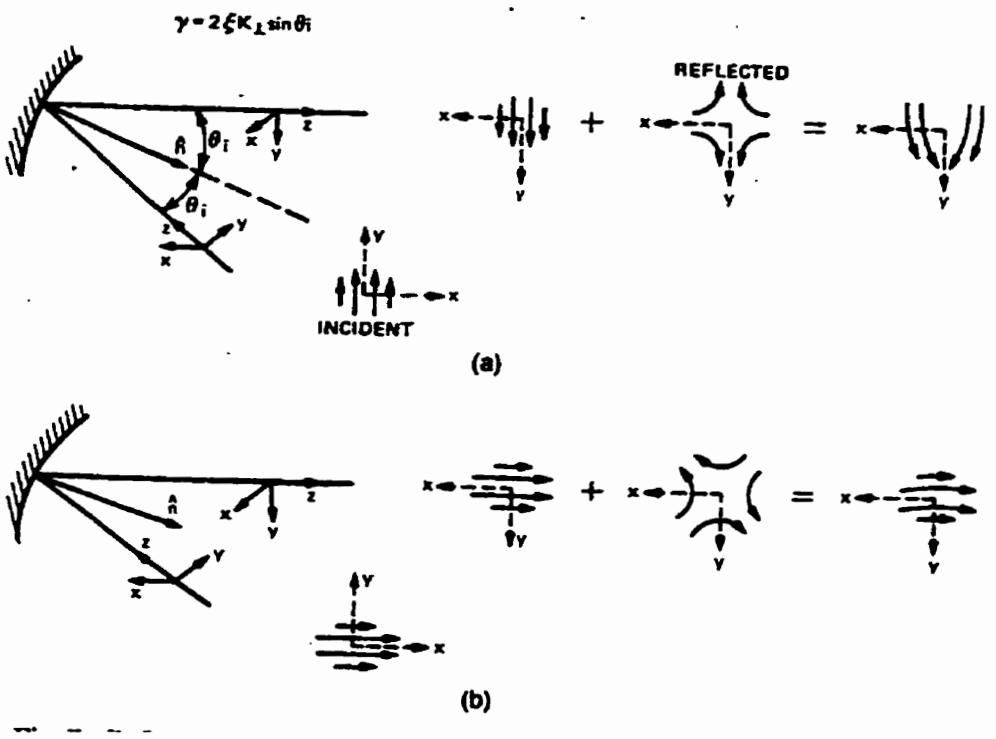

Figure IV.3: Reflector matrix components (fields viewed in direction opposite to propagation direction). a) V_{00} incident. b) H_{00} incident.